This is to certify that the
dissertation entitled

THE DEVELOPMENT OF MnO_2 COATED CERAMIC MEMBRANES FOR COMBINED CATALYTIC OZONATION AND ULTRAFILTRATION OF DRINKING WATER

presented by

Lindsay Marie Corneal

has been accepted towards fulfillment
of the requirements for the

Ph.D. degree in Materials Science and Engineering

Major Professor's Signature

March 9, 2010

Date

MSU is an Affirmative Action/Equal Opportunity Employer

DATE DUE	DATE DUE	DATE DUE

THE DEVELOPMENT OF MnO_2 COATED CERAMIC MEMBRANES FOR COMBINED CATALYTIC OZONATION AND ULTRAFILTRATION OF DRINKING WATER

By

Lindsay Marie Corneal

A DISSERTATION

Submitted to
Michigan State University
in partial fulfillment of the requirements
for the degree of

DOCTOR OF PHILOSOPHY

Materials Science and Engineering

2010

ABSTRACT

THE DEVELOPMENT OF MnO_2 COATED CERAMIC MEMBRANES FOR COMBINED CATALYTIC OZONATION AND ULTRAFILTRATION OF DRINKING WATER

By

Lindsay Marie Corneal

A novel method for the preparation of hydrated MnO_2 by the ozonation of $MnCl_2$ in water is described. The hydrated MnO_2 was used to coat titania water filtration membranes using a layer-by-layer technique. The coated membranes were then sintered in air at 500°C for 45 minutes. Upon sintering, the MnO_2 is converted to α-Mn_2O_3 (as characterized by x-ray and electron diffraction).

Atomic force microscopy (AFM) imaging showed no significant change in the roughness or height of the surface features of coated membranes, while scanning electron microscopy (SEM) imaging showed an increase in grain size with increasing number of coating layers. Energy dispersive x-ray spectroscopy (EDS) mapping and line scans revealed manganese present throughout the membrane, indicating that manganese dispersed into the porous membrane during the coating process and diffused into the titania grains during sintering. Selected area diffraction (SAD) of the coated and sintered membrane was used to index the surface layer as α-Mn_2O_3. The surface layer was uneven, although there was a trend of increasing thickness with increasing coating layers.

The coating acts as a catalyst for the oxidation of organic matter when coated membranes are used in a hybrid ozonation-membrane filtration system. A trend of decreasing total organic carbon (TOC) in the permeate water was observed with increasing number of coating layers. The catalytic activity also manifests itself as improved recovery of the water flux due to oxidation of foulants on the membrane surface.

Ceramic nanoparticle coatings on ceramic water filtration membranes must undergo high temperature sintering. However, this means that the underlying membrane, which has been engineered for a given molecular weight cut-off (MWCO), also undergoes a high temperature heat treatment that serves to increase pore size that have resulted in increases in permeability of titania membranes. Coating the titania membrane with manganese oxide followed by sintering in air at 500°C maintains the MWCO of the membranes, with high DI water permeability, which may be favorable in terms of membrane use.

SEM micrographs of titania membrane samples sintered between 500°C to 900°C were analyzed to identify a statistically significant increase in grain size with increasing sintering temperature. The grains however, generally retain a uniform shape until the 900°C sintering temperature, where large, irregularly shaped grains were observed. AFM analysis showed a corresponding increase in the surface roughness of the membrane for the sample sintered at 900°C.

To Chris and Jacquie, for all of your love and support.

ACKNOWLEDGMENTS

I have many people that I would like to thank for their help and support during my doctoral studies. First, I would like to thank my advisor, Dr. Melissa Baumann and the members of my guidance committee, Dr. Eldon Case, Dr. Susan Masten and Dr. Volodymyr Tarabara, for their help, advice, time and support.

I could not have completed my research without the financial support of the US National Science Foundation (Grant No. 0506828) Nanoscale Interdisciplinary Research Team (NIRT) program. The other members of this NIRT group have been a great assistance to me. I would like to thank Dr. Simon Davies for his help and guidance, along with Dr. Jeonghwan Kim, Dr. Seokjong Byun and Ms. Alla Alpatova for all of their help. I would also like to thank Mr. Minyoung Jeong for his assistance in preparing manganese oxide and coating of membranes during the early part of my research study.

There have been many other individuals that have helped me along the way. From the Center for Advanced Microscopy, I would like to thank Dr. Alicia Pastor, Dr. Ewa Danielewicz, Dr. Xudong Fan, Dr. Stanley Flegler and Dr. Carol Flegler. From the Department of Chemistry, I would like to thank Mr. Rui Huang. From the Composite Materials and Structures Center, I would like to thank Dr. Mike Rich, Dr. Per Askeland and Dr. Hazel-Ann Hosein.

Finally, I would like to thank my family for all of their support. Chris, Jacquie, Dan, Kelly, mom and dad, your love and encouragement has helped me more than I could ever put into words. Audra, your smiles brighten even the most stressful days.

There have been many others that have helped me along the way. I would like to thank everyone that I may have inadvertently omitted.

TABLE OF CONTENTS

LIST OF TABLES

LIST OF FIGURES

CHAPTER 1

INTRODUCTION

1.1 INTRODUCTION

While ozone reacts with humic substances to produce oxygenated by-products, it does not remove organic matter from water to any significant extent, therefore, the use of a catalyst is required [1]. Karnik et al. [2-4] have shown that nanolayers of Fe_2O_3 act as a catalyst in the oxidation of organic matter. Here, ceramic water filtration membranes coated with iron oxide nanoparticles were shown to improve water quality by reducing the dissolved organic carbon (DOC) and disinfection by-products (DBPs) in permeate samples when used in a hybrid ozonation-membrane filtration system. While the nanostructured iron oxide coating (the colloids had an initial particle size of 4 to 6 nm) dramatically improved water quality as well as prevented membrane fouling, other coated

membrane filtration surfaces, in combination with ozonation, have not been evaluated.

A possible coating alternative to iron oxide is manganese dioxide. Manganese-containing catalysts have been shown by Spasova et al. to be quite effective for the decomposition of ozone [5]. Also, manganese-containing catalysts have been found to catalyze the degradation of organic matter by ozone [6-44]. Studies have shown that manganese-containing catalysts are effective for the oxidation of pyruvic acid [9, 11], oxalic acid [8], metol [10], humic acids [12] and atrazine [13, 14] by ozone in aqueous systems as well as for the oxidation of volatile organic compounds (VOCs) in gas phase reactions [25, 30-32, 34-40, 43, 44].

Using MnO_2 nanoparticles to coat ceramic water filtration membranes should produce a catalytic surface to aid in the oxidation of natural organic matter (NOM), however the optimal number of coating layers, the sintering conditions and the surface reactions that act to reduce the concentration of contaminants in water must be determined. Layering of fine nanoparticles will help ensure an even coating on the membrane surface. By varying the number of coating layers and the sintering temperature and time, the optimum coating conditions can be determined based on improved water quality. The MnO_2 coated membranes must also be characterized to determine the final structure of the membrane and coating layer. Finally, the thermal stability of the membranes during the heat treatment required for the coating and sintering process must be determined.

1.2 OBJECTIVES

The objectives of this dissertation research were: 1) to produce and characterize MnO_2 nanoparticles, 2) to use these nanoparticles to coat ceramic water filtration membranes, 3) to evaluate the water quality using the coated membranes in combination with ozonation 4) to characterize the coated membranes and 5) to study the thermal stability of the ceramic membranes.

To coat ceramic water filtration membranes with MnO_2 nanoparticles, the particles had to first be synthesized. Many methods have been used to produce MnO_2 nanoparticle colloids [45-49]. One of the objectives of this research was to use ozone to oxidize Mn based on a modification of the method used by Kijima et al. [50].

Once the MnO_2 nanoparticles were synthesized, they were characterized to determine their composition and particle size. The nanoparticles were characterized using x-ray diffraction (XRD), x-ray photoelectron spectroscopy (XPS), energy dispersion spectroscopy (EDS), wet chemical analysis, transmission electron microscopy (TEM) and selected area diffraction (SAD).

When suitable MnO_2 nanoparticles had been prepared, they were then used to coat titania water filtration membranes (INSIDE CéRAM, TAMI North America, St. Laurent, Québec, Canada) using a layer-by-layer technique. The deposition

of thin nanoparticle layers helps ensure even coating of the membranes. The coated membrane was then sintered to fuse the coating to the membrane to obtain a durable coating. The optimum sintering conditions of time and temperature were determined by comparing water quality results using the sintered coated membranes in an ozone-filtration system. Additionally, the number of coating layers yielding the optimum water quality was also assessed in a similar manner.

Transmission electron microscopy (TEM), scanning electron microscopy (SEM) and atomic force microscopy (AFM) were used to characterize the morphology and microstructure of the coating layer, the surface and the pore structure of the sintered MnO_2 coated membranes.

Finally, the thermal stability of the titania membrane was studied. In this way, the link between the membrane performance and the coating and sintering of the membrane was determined.

1.3 STRUCTURE OF DISSERTATION

This dissertation has been organized in chapters. A detailed literature review of relevant background information for this dissertation is presented in Chapter 2. Also included in Chapter 2 is a review of catalytic membrane filtration, the

catalytic properties of manganese oxides, manganese oxide nanoparticle preparation methods, layer-by-layer coating and finally, sintering of porous ceramics.

The experimental work in this dissertation is covered in Chapters 3, 4, 5 and 6. Chapter 3 presents the preparation and characterization of the manganese oxide coating material. The characterization of the coating material was performed using wet chemistry, x-ray photoelectron spectroscopy (XPS), x-ray diffraction (XRD), thermogravimetric analysis (TGA), UV-visible absorbance spectroscopy and transmission electron microscopy (TEM) analysis.

Chapter 4 presents the catalytic membrane preparation, using a layer-by-layer coating method, and coated membrane characterization. The characterization of the coated membranes was performed using atomic force microscopy (AFM), scanning electron microscopy (SEM), energy dispersive x-ray spectroscopy (EDS) and transmission electron microscopy (TEM) analysis.

Chapter 5 presents the use of the catalytic coated membranes in a hybrid ozonation-membrane filtration system. The effect of the manganese oxide and the number of coating layers on the total organic carbon (TOC) removal and the flux recovery are discussed.

Chapter 6 presents the thermal stability of the ceramic membranes. Characterization of uncoated membranes, under various sintering conditions, was performed using x-ray diffraction (XRD), scanning electron microscopy (SEM) and atomic force microscopy (AFM) analysis. Characterization of manganese oxide coated membranes, under various sintering conditions, was performed using scanning electron microscopy (SEM) analysis and by performing molecular weight cut-off (MWCO) measurements.

Chapter 7 presents a summary and conclusions, with recommendations for future work being presented in Chapter 8.

CHAPTER 2

BACKGROUND

2.1 CATALYTIC MEMBRANE FILTRATION

Researchers have studied the use of ozonation with polymeric membrane filtration [51-54]. However, polymeric membranes are susceptible to degradation by ozone [52, 55] due to oxidative attack. Hence, ozone must be allowed to decompose before the ozonated water contacts the polymeric membrane.

Polytetrafluoroethylene (PTFE) [56], polyvinylidene fluoride (PVDF) [57-59] and polysulfone (PS) [60] membranes have been shown to be sufficiently ozone resistant to be used in a hybrid ozone-membrane process. More recently, however, because of their resistance to ozone and their longevity in water filtration systems, ceramic membranes have been used in combination with ozonation [2-4, 57, 61-74]. Despite the benefits of ceramic membranes,

polymeric membranes are still widely used for water filtration since ceramic membranes have not been studied as extensively for water treatment [70, 75, 76] and ceramic membranes are more expensive than polymeric membranes [57, 77-80].

Karnik et al. have reported their extensive work with catalytic membranes for drinking water treatment using ozonation and ultrafiltration [2-4, 65-68]. Their work used an alumina, zirconia and titania (AZT) ceramic membrane which was then coated with a Fe_2O_3 nanoparticle coating. They demonstrated that the Fe_2O_3 coated membrane improved the performance of a combined ozonation-filtration system. The enhanced performance was linked to the catalytic decomposition of ozone by the iron oxide to produce hydroxyl and other radicals [66]. The radicals produced at the Fe_2O_3 surface degrade organic foulants, resulting in a decrease in membrane fouling and a concomitant decrease in the dissolved organic carbon in the permeate [66]. The grain size of the Fe_2O_3 coating layer (as measured by SEM) increased with increasing number of coating layers (from 21 ± 0.24 nm for the uncoated membrane to a maximum of 66 ± 23 nm for the membrane coated with 40 layers). The membrane coated with 40 layers of the Fe_2O_3 coating showed the largest improvement in water quality, in terms of the removal of total trihalomethanes, halo acetic acids, aldehydes, ketones and ketoacids [4].

2.2 CATALYTIC PROPERTIES OF MANGANESE OXIDES

Catalysis of organic matter by manganese oxide with ozone has been studied by others [6-44], indicating that manganese oxide would be quite promising as a coating for ceramic membranes. Naydenov and Mehandjiev used manganese dioxide to catalytically oxidize benzene by ozone [6]. They achieved complete catalytic oxidation of benzene by ozone on MnO_2 in a temperature range of 10-80°C (283-353 K). Einaga et al. [18-24] also studied the effects of catalyst support, reaction conditions and manganese loading on the ability of manganese oxide catalysts to catalyze the oxidation of benzene. Andreozzi et al. demonstrated the catalytic ability of MnO_2 for the ozonation of pyruvic acid [9, 11], oxalic acid [8] and metol [10]. They found that pyruvic acid did not react with either MnO_2 or O_3, however, significant oxidation was observed when ozone was used in combination with MnO_2 [9, 11]. Andreozzi et al. found that oxalic acid reacted only slightly with MnO_2 in the absence of ozone, however, the reactivity was greatly increased with the addition of ozone [8]. Although these experiments were done in a semibatch process with suspended MnO_2 particles, rather than on a coated membrane, the catalytic properties of the MnO_2 in the presence of ozone seem quite promising.

Lee et al. examined the catalytic ozonation of humic acids [12]. Humic acid was used as a model organic compound because it is a major constituent of natural

organic matter. The authors observed a significant decrease in UV absorption with MnO_2 combined with ozone, indicating the oxidation of the humic acids [12].

Ma and Graham [13, 14] showed that manganese oxide catalysts enhanced the oxidation of atrazine by promoting ozone decomposition and hydroxyl radical formation. Ma and Graham's work also demonstrated that humic substances have a positive effect on the oxidation of atrazine as compared to that observed with the manganese catalyst and ozone alone [13, 14].

MnO_2 can therefore be an effective catalyst for the ozonation of organic matter in water. The favorable catalytic properties of manganese dioxide suggest that experimentation with a MnO_2 coating on the ceramic filtration membranes for the use in combined ozonation-filtration is logical. In order to coat the ceramic filtration membranes it is necessary to produce MnO_2 nanoparticles.

Additionally, Mn_2O_3 has been used as an effective catalyst in gas phase reactions [81-83] and may be effective for the decomposition of ozone in an aqueous system. The effectiveness of a Mn_2O_3 coating would need to be evaluated using water quality measurements when the coated membrane is used in the hybrid ozonation-membrane filtration system since previous work has only shown Mn_2O_3 to be effective in gas phase reactions.

2.3 PREPARATION OF MANGANESE OXIDE NANOPARTICLES

The oxides of manganese have been studied quite extensively for use in solid-state batteries and fuel cells [84-86] and various methods have been used to produce MnO_2 nanoparticle colloids.

Fujimoto et al. sonified manganese dioxide nanoparticles with a diameter of approximately 2 nm [45]. An argon-purged aqueous solution containing 0.1 mM of $KMnO_4$ was sonicated in the presence of 8 mM sodium dodecylsulfate (SDS) at 200 kHz, with an input power of 200 W. The UV-VIS spectra showed that the absorbance peaks from the MnO_4^- ions, which were originally at 525 nm and 545 nm, disappeared after 10 minutes of sonication and were replaced by a peak around 360 nm, indicating the presence of MnO_2.

Lume-Pereira et al. used γ-irradiation [46] to produce manganese oxide nanoparticles. Potassium permanganate (4×10^{-4} M) was irradiated at pH 10 and a temperature of 20°C. Using a dose rate of 7×10^4 rad/h, the absorption of the MnO_4^- ion at ~530 nm disappeared and was replaced by a broad band at ~336 nm, after a dose of 4.0×10^5 rad. Electron microscopic studies of an evaporated drop on a thin carbon carrier showed particles of 3-5 nm in diameter.

Lume-Pereira et al. described a "conventional" manganese oxide colloid preparation method [46] in which 75 mL of an aqueous solution of 4×10^{-4} M $Mn(ClO_4)_2$ was added to 50 mL of an aqueous solution of 4×10^{-4} M $KMnO_4$ with strong stirring. The colloid formed instantly. The exact size of the manganese dioxide particles is not known, however, the solution could not be filtered through a 10 nm nucleopore filter. This indicates that the particles were significantly larger than the particles that were produced using the γ-irradiation method [46].

Stadniychuk et al. [47] prepared a MnO_2 colloid using a modification of the Clorox method described by Ulrich and Stone [48]. In this modified method, Stadniychuk et al. mixed 15 mL of 1.0 M NaOH and 100 mL of 0.705 M NaOCl with 1620 mL of deionized water and stirred for 5 min to obtain a pH of 12.5. Then 13 mL of 1.009 M $MnCl_2 \cdot 4H_2O$ were added and rapidly stirred for 90 min. The mixture had a pH of 7-8. The solution was left to settle for approximately 24 hours. Excess liquid was removed and deionized water was added to make 500 mL of suspension. The suspension was then ultrasonicated for 3 hours and dialyzed against deionized water for 5 days. The water was changed at 1, 4, 16, 48, 72 and 96 hours to remove electrolyte ions. The sol was then removed from the dialysis bag and ultrasonicated for 5 hours. The sol was next filtered to remove large particles to prevent Ostwald ripening. This method produced MnO_2 particles with a mean diameter of 30 nm [47].

Stadniychuk et al. [47] also described a MnO_2 preparation developed by Bach et al. [87] which used a fumaric acid reduction method [87], in which 400 mL of 0.250 M $NaMnO_4 \cdot H_2O$ were mixed with 100 mL of 0.333 M $C_2H_2O_4Na_2$ (fumaric acid disodium salt) and stirred vigorously for 1 hour, then ultrasonicated for 3 hours. Then 10 mL of 2.5 M H_2SO_4 were added and the solution was stirred for 3-5 hours. The solution was then put in dialysis bags having a molecular weight cut-off of 3500 Da and dialyzed for 3 days against deionized water, with the water being changed at 1, 4, 12, 24 and 48 hours. This method produced MnO_2 particles with a mean diameter of 180 nm.

Kijima et al. [50] used ozonation to produce α–MnO_2. Fourteen (14) g of $MnSO_4 \cdot 5H_2O$ were dissolved in 600 mL of 3 M H_2SO_4. The solution was then heated to 80°C (353 K) while stirring at 200 rpm. When the solution reached 80°C, ozone was bubbled into the reactor for 3 hours at a rate of 40 cm^3/min. The O_3 concentration was 135 mg/L.

Luo prepared MnO_2 nanoparticles by directly mixing potassium permanganate and a polyelectrolyte aqueous solution [49]. At room temperature, 100 mL of a 20 mM potassium permanganate aqueous solution was mixed with equal amounts of poly(allylamine hydrochloride) (PAH) aqueous solution at a molar ratio of 4:1 of PAH (repeating unit) to Mn. This method resulted in spherical MnO_2 nanoparticles with diameters of 6 – 12 nm.

Many of these methods (i) involve using equipment that is not readily available [45, 46] or (ii) produce MnO_2 nanoparticles that are too large [47, 48]. To evenly coat the membranes, particle sizes of less than 20 nm are required. The direct mixing method by Luo [49], described above, appeared to be the best option for preparing MnO_2 nanoparticles of a fine, uniform particle size.

Ozone is a strong oxidizing agent that reacts with Mn(II) ions to form manganese oxide according to equation (1) [88]:

$$Mn^{2+} + O_3\,(aq) + H_2O \rightarrow MnO_2\,(s) + O_2\,(aq) + 2H^+ \qquad (1)$$

To produce nanoparticles of the desired size, however, particle growth and agglomeration must be controlled. The particle growth and agglomeration can be controlled for this ozonation method by adjusting the duration of ozonation as well as the pH of the resulting colloid.

Because of the lack of mechanical stability, the use of manganese oxide nanoparticles as a coating layer for ceramic water filtration membranes required that the deposition layer on the membrane be sintered [3, 4, 66-68]. MnO_2, however, decomposes to Mn_2O_3 at approximately 550°C (823 K) [89, 90], making it necessary to characterize the nanoparticles before and after sintering.

2.4 LAYER-BY-LAYER COATING

Based on the work of Karnik et al [3, 4, 66-68] with iron oxide nanoparticles, a layer-by-layer technique can be used to create a thin coating of the MnO_2 particles on the ceramic filtration membranes. This technique is used so that reproducible layer thicknesses can be achieved [91]. The adsorption of the charged molecules on the surface reverses the charge on the surface and restricts the adsorption to a single layer [91-94]. Introducing molecules of opposite charge then allows the adsorption of a second layer. Alternating between the oppositely charged molecules results in a multilayer structure [3, 4, 68, 91-94].

Previous work has been done with layer-by-layer assembly of ultrathin films of MnO_2 on electrodes [91, 94]. To create the layers, the electrodes were first submerged in a colloidal solution of manganese dioxide for 15 minutes and then rinsed with a pH 12 solution to remove any weakly adsorbed molecules. The electrodes were then submerged in poly(dimethyldiallylammonium chloride) (PDDA) (2 mg/mL, pH 12) for 15 minutes, then rinsed again with a pH 12 solution. This procedure was repeated for the desired number of layers.

2.5 SINTERING OF POROUS CERAMICS

As ceramic membranes become more widely used, there is a growing concern about the effect of sintering temperature on the underlying membrane structure [95, 96]. Although ceramic membranes have higher thermal stability than polymeric membranes [96], there can still be structural changes that occur in ceramic membranes at elevated temperatures [95, 96]. Lin et al. [95] found that lanthanan-doped alumina and titania membranes and yttria-doped zirconia membranes significantly improved the thermal stability of the memberanes. The doping raises the phase transformation temperatures in the materials and decreases the reduction in surface area and pore growth below the phase transformation temperatures [95]. However, doping of the ceramic membranes does not completely retard the structure changes that occur at elevated temperatures [95]. When ceramic membranes are coated with materials that necessitate high temperature treatment, the morphology and microstructure of the underlying membrane may be altered during the sintering of the coating. This may in turn result in changes to the underlying membrane properties such as the pore size and structure.

During sintering, the grains can either grow with very little densification or there can be an increase in the density, to approximately 95% of theoretical density, followed by grain growth [97]. Alternatively, grain growth and densification can occur simultaneously [97]. During densification, mass is transferred from the

grain boundary or region between the particles to the pores or the necks between the particles (Figure 1) [97]. The driving force for the increase in grain size and pore size is the reduction in the surface energy. By increasing the average grain size, there is a reduction in the total surface area, resulting in an overall reduction in the surface energy [97].

During the grain growth process, pores located at the grain boundaries can move with the grain boundaries and coalesce into larger pores at the intersections of the grains (Figure 2) [97, 98]. In fine grained oxides, an increase in pore size is observed in the initial stages of sintering. As sintering time continues, however, there is a marked increase in grain size [97, 98].

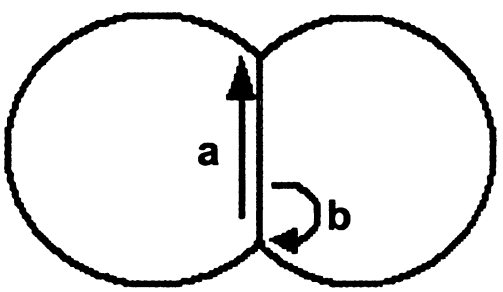

Figure 1. Schematic representation of densification by a) grain boundary diffusion and b) volume diffusion from the grain boundary area to the neck area (Adapted from Figure 10.9b in [97]).

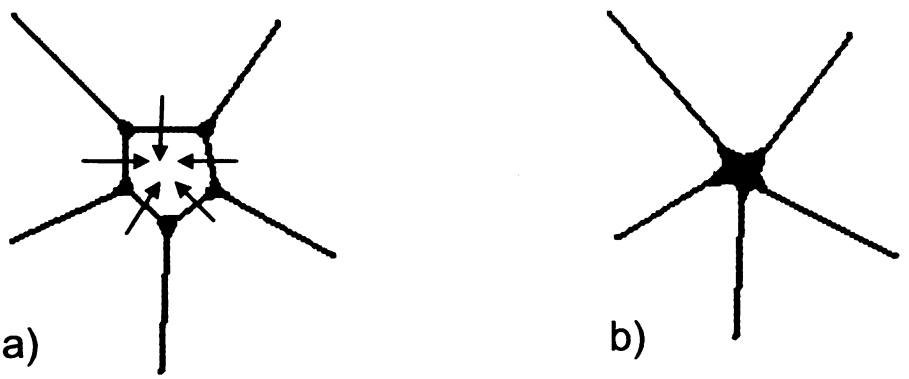

Figure 2. Schematic representation of a) pores at grain boundaries that b) coalesce at the intersections of grains during grain growth.

Since the nanoparticle coated membranes examined in this study are sintered for relatively short periods of time, the underlying membrane support only experiences the early stages of sintering and is not able to completely eliminate the agglomerated pores or further densify. An increase in the pore diameter of porous ceramic membranes with increasing sintering temperature (when sintered for short periods of time) has previously been observed by Baticle et al. [99].

Although purchased membranes were used in the work described in this dissertation, it is possible to synthesize ceramic membranes [72-74, 100-103], which could then be tailored for subsequent application of a catalytic coating and sintering. Some possible membrane preparation methods include the sol-gel process [73, 74, 100, 101] and slip casting [73, 102, 103].

In the sol-gel process, a colloid is prepared by dispersing the ceramic particles in an electrolyte. Modifying the charge on the particles, by adjusting the pH of the electrolyte, the colloidal suspension transforms to a gel structure [73]. The gel consists of agglomerates or interlinked chains of particles [73]. Adjusting the agglomerate size at the time of gelation, the density of the film can be adjusted [73]. This method can be used to produce membranes with narrow pore size distributions [73].

In the slip casting method, a porous support is dipped into a colloidal ceramic suspension of ceramic particles called a slip. The dispersion medium flows into the pores of the support and the solid particles remain at the entrance of the pores. This forms a gel layer on the surface of the membrane. The viscosity of the slip can be adjusted so as to ensure that the slip does not penetrate into the porous support [73].

To achieve good reproducibility in the membranes as well as a narrow pore size distribution, the optimum method for membrane fabrication would be the sol-gel process [73, 74, 102]. Manufacturing the membranes so that the resulting membranes are very reproducible would allow for comparisons to be made between membranes and the effects of any coatings and heat treatments could also be compared.

CHAPTER 3

PREPARATION AND CHARACTERIZATION OF MANGANESE OXIDE COATING MATERIAL

3.1 INTRODUCTION

The oxides of manganese have been studied quite extensively for use as catalysts for the oxidation of organic matter by ozone [6-44]. Preparing a manganese oxide nanoparticle colloid and applying it to a ceramic water filtration membrane, should therefore, produce a catalytic coating to degrade organic matter in water when used in a hybrid ozonation-membrane filtration system [2-4, 65-68].

Various methods have been used to prepare manganese oxide nanoparticle colloids [45-50]. Kijima et al. [50] oxidized Mn^{2+} to Mn^{4+} in H_2SO_4 (>2 M). However, since ozone is a strong oxidizing agent, it should react with Mn^{2+} at

circumneutral pH to produce MnO_2 [88]. The MnO_2 prepared using this modified ozonation method was characterized to confirm that MnO_2 was in fact present and to determine the size of the colloidal particles.

3.2 MATERIALS AND METHODS

Manganese oxide nanoparticles were prepared using ozonation. This method is significantly different than that developed by Kijima et al. [50], where the oxidation was performed in strong H_2SO_4 (> 2 M) solution and at elevated temperatures (> 70°C). For the nanostructured manganese oxide used in our study, the ozonation was performed in deionized (DI) water at room temperature. The system used to fabricate the nanoparticles (Figure 3) included a 2 L covered glass reactor, with inlet and outlet ports for the ozone gas and an injection port. A fritted glass aerator was used to bubble ozone into the reactor. Pure oxygen, from a compressed gas cylinder was used to generate ozone. The oxygen was first passed through a moisture trap containing anhydrous calcium sulfate (Drierite, Xenia, OH), then through an ozone generator (Ozotech Inc. Model OZ2PCS-V, Yreka, CA) at a flow rate of 50 mL/min. Ozone was bubbled into 1000 ml of deionized water (DI water) for 20 minutes. Following this, 100 mL of a 2 mM manganese (II) chloride (99+%, Sigma-Aldrich Co., St. Louis, MO) aqueous solution was injected. The ozonation was stopped immediately after the addition of $MnCl_2$. Continuing to bubble the ozone into the sample after the

addition of $MnCl_2$ resulted in particles that were visible to the naked eye. Ceasing ozonation once the $MnCl_2$ was added, resulted in a transparent, golden brown colored colloidal suspension having a pH of 3.7. The vented gas was passed through a 2% solution of potassium iodide (KI) in order to destroy residual ozone.

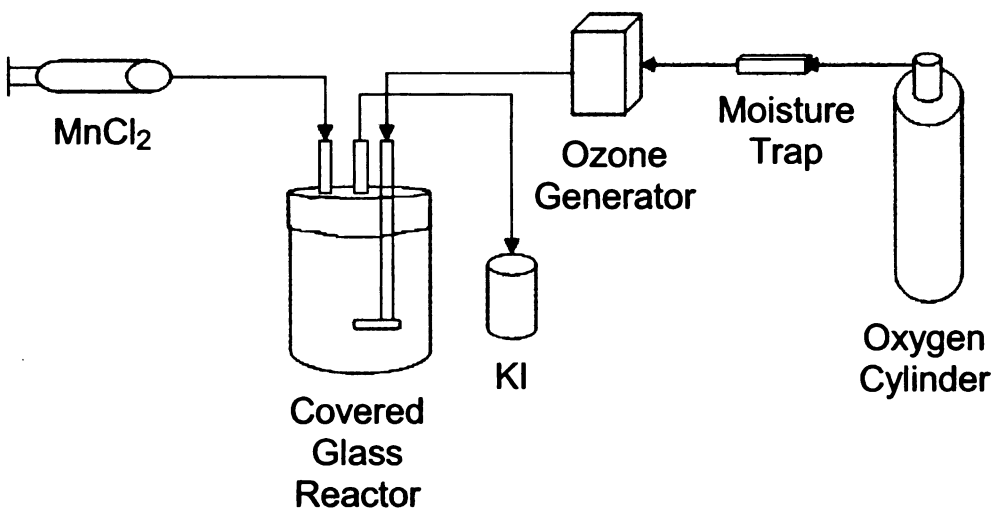

Figure 3. Schematic representation of apparatus used for preparation of MnO_2 colloid using ozonation.

At pH 3.7, the manganese oxide particles rapidly agglomerated. The particles were centrifuged (at 2500 rpm) for 30 min to settle the particles. The supernatant was then decanted and discarded. The resulting particles were dispersed into 500 mL of a 10^{-4} N KNO_3 (≥ 99.0%, J.T. Baker, Phillipsburg, NJ) solution and sonicated in an ice bath (Branson Ultrasonics Corporation Model 250 Sonifier, Danbury, CT) for 30 minutes, at an output of 58 watts, to break up any

agglomerated particles. The final pH of the resulting suspension was 6.3. At the pH of zero point of charge (pH_{zpc}) the net surface charge on a particle is zero, and particles in a suspension will rapidly agglomerate [104, 105]. For $pH>pH_{zpc}$ the net surface charge is negative and for $pH<pH_{zpc}$ the net surface charge is positive. Therefore, as the pH is adjusted away from pH_{zpc} the particles in a suspension repel each other, resulting in a stable suspension [104, 105]. Since the pH_{zpc} for MnO_2 is 1.48 - 2.40 [106, 107], by raising the pH further from the pH_{zpc} (from 3.7 to 6.3), a stable colloidal suspension was able to be achieved.

The second approach to preparing manganese oxide nanoparticles was based on the method described by Luo [49]. For this method, 100 mL of a 20 mM $KMnO_4$ (>99.0%, Sigma-Aldrich) aqueous solution was mixed with an equal amount of an aqueous solution of 80 mM poly(allylamine hydrochloride) (PAH, average molecular weight: 15,000, ≥95.0%, Aldrich) at a high speed for 5 min at room temperature. No further treatment was necessary before the colloid could be used.

Samples of the manganese oxide particles were prepared for TEM by dipping a holey carbon coated TEM grid into both colloidal manganese oxide suspensions prepared using both methods.

The manganese oxide colloid was used to coat ceramic water filtration membranes and then the coated membranes were sintered to adhere the coating to the membranes [3, 4, 66-68]. Since MnO_2 reduces to Mn_2O_3 at approximately 550°C [89, 90], a sintering temperature of 500°C was chosen to avoid this reduction. Since nanoparticles have a greater reactivity than micron-sized particles [108, 109], the MnO_2 nanoparticles that are prepared, may still be reduced to Mn_2O_3 at a sintering temperature of 500°C. Therefore, it was necessary to characterize the phase of the nanoparticles before and after sintering.

To examine the effect of sintering on the manganese oxide, the centrifuged particles from the sample prepared using ozonation were dried in air and the dried particles were pressed into a 12 mm disk of approximately 1 mm thickness using a uniaxial press at 31 kN. The disk was sintered (in an alumina dish) in air at 500°C for 45 minutes. Using the same process, a second disk was prepared and sintered at 550°C for 30 minutes to compare the oxidation state of the sintered manganese oxide. Half of each sintered disk was used for XRD analysis. The other half of each disk was ground with a mortar and pestle and approximately 10 mg of the ground powder was added to 100 mL of 10^{-4} N KNO_3 (≥99.0%, J.T. Baker, Phillipsburg, NJ) and sonicated for 30 minutes (at an output of 58 watts) in an ice bath in preparation for the TEM analysis. Samples of the suspension of sintered manganese oxide powders were prepared for TEM

analysis by dipping a holey carbon-coated TEM grid into the sonicated suspensions followed by air drying.

Characterization of the oxidation state of manganese in the sintered samples prepared using ozonation was performed using the formaldoxime procedure described by Morgan and Stumm [110]. The analytical procedures were as follows: The manganese oxide was ground with a mortar and pestle and 10 mg of the ground powder was added to 100 mL of 10^{-4} N KNO_3 and sonicated for 30 minutes (at an output of 58 watts) in an ice bath. In a 100 mL volumetric flask, 10 mL of the sonicated manganese oxide suspension was added (after being filtered through a 0.45 μm filter), along with 2 mL of the formaldoxime reagent (10 g of paraformaldehyde and 23.5 g of reagent grade hydroxylamine sulfate dissolved in DI water to give a final volume of 100 mL), 5 mL of 5 M NaOH and DI water to bring the final volume to 100 mL. The optical absorbance was then measured using the Spectronic Genesys spectrophotometer (Milton Roy, Iveland, PA) at a wavelength of 450 nm. In another volumetric flask, 5 mL of the manganese oxide colloid was added, along with 10 mL of 0.1% o-tolidine dihydrochloride, 25 mL of 3 M perchloric acid and sufficient DI water to bring the final volume to 100 mL. The absorbance was then measured at a wavelength of 440 nm. An aliquot of the sample used for the o-tolidine determination was then analyzed using atomic absorption (manganese atomic absorption standard solution, 1000 μg/mL Mn^{+2} in 1 wt% HNO_3, Aldrich, Milwaukee, WI) using the SpectrAA-200 Flame AA

Spectrometer (Varian, Inc., Palo Alto, CA) to determine the total Mn content of the solution.

The Mn(II) content of the sintered samples was determined by the formaldoxime method [110], the concentration of oxidized Mn (=Mn(III)+2Mn(IV)) was determined using the o-tolidine procedure [110] and the total Mn (=Mn(II)+Mn(III)+Mn(IV)) was measured by atomic absorption spectrophotometry. The concentration of the Mn present in each of the three oxidation states was determined by difference using these three measurements.

XRD was also used to determine the phases present in the sample prepared using ozonation. Half of each sintered disk was analyzed by XRD using a Rigaku Rotaflex RU-200B (45KV/100mA, copper radiation, Rigaku, Tokyo, Japan). High purity samples of both MnO_2 (Riedel-de Haën, 99% (complexometric)) and Mn_2O_3 (Aldrich, 99.999% (metals basis)) were purchased and used for XRD comparison.

TEM images were obtained using a JEOL 2200FS transmission electron microscope (JEOL, Tokyo, Japan) at an accelerating voltage of 200 kV. Photomicrographs were collected at magnifications between 150,000x an 250,000x using a Hamamatsu CCD digital camera (Hamamatsu City, Japan). Particle sizes were measured using the Simple Measure program (JEOL, Tokyo, Japan). Particle size measurements were made across the diagonal of the

particles and the average and standard deviation is calculated from measurements of 25 particles (Simple Measure, JEOL, Tokyo, Japan). X-ray photoelectron spectroscopy (XPS) was performed using a Perkin Elmer Phi 5400 electron spectroscopy for chemical analysis (ESCA) (magnesium Kα X-ray source, Perkin Elmer, Waltham, Massachusetts), thermal gravimetric analysis (TGA) was performed using a TGA Q50 (TA Instruments, New Castle, Delaware) and the UV-vis absorbance spectrum was obtained using a MultiSpec-1501 spectrophotometer (Shimadzu Scientific Instruments, Kyoto, Japan).

3.3 RESULTS AND DISCUSSION

3.3.1 CHARACTERIZATION OF PARTICLES PREPARED BY OZONATION

Figure 4 is a TEM micrograph of the manganese oxide colloidal particles prepared using ozonation. The TEM micrograph shows particles of approximately 92 nm ± 13 nm, having a flake-like morphology. Cheney et al., made similar observations of amorphous MnO_2 with diameters of ~100 nm [111].

Ozonation of Mn(II) should result in the formation of MnO_2 [88], however, to confirm that the manganese oxide prepared is in fact MnO_2, UV-vis absorption spectroscopy was used, since it was not possible to obtain selected area diffraction (SAD) patterns using the TEM because these flakes formed such a

thin layer on the TEM grids that they would not diffract the electron beam sufficiently to index the resulting diffraction pattern. The UV-vis spectrum (in Figure 5) showed a broad peak at 370 nm, indicative of MnO_2 [45, 46, 49]. Lume-Pereira et al. observed a broad 340 nm adsorption peak for an MnO_2 colloid [46], while Fujimoto et al. observed an absorption band for nanocrystalline MnO_2 (as confirmed by TEM and XRD) located around 360 nm [45] and Luo determined the absorbance peak for MnO_2 nanoparticles (as confirmed by the x-ray photoelectron spectra (XPS)) centered at 370 nm [49].

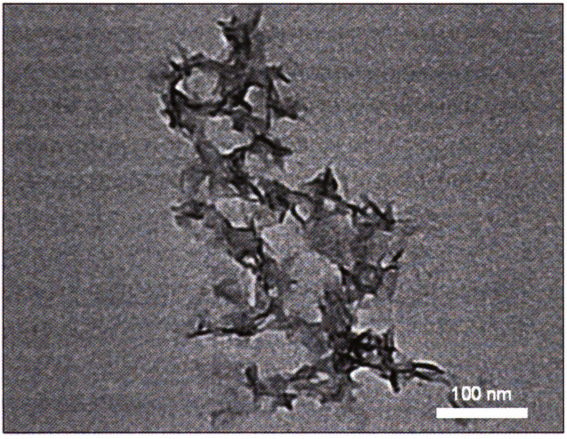

Figure 4. TEM micrograph of hydrated MnO_2 colloid prepared using ozonation, resulting in flakes of a non-crystalline hydrated manganese oxide, with an average particle size of 92 nm ± 13 nm.

TGA results (Figure 6) confirm that the manganese oxide prepared by ozonation is hydrated, with physisorbed water that is driven off at approximately 80°C (353 K). Reddy and Reddy also found physisorbed water to be removed from MnO_2 xerogel and ambigel between 30-250°C [112]. Since the MnO_2 particles prepared by mixing of PAH and $KMnO_4$ had a smaller particle size, they were used to coat the membranes to determine how the smaller particle size would affect the surface morphology of the coated membrane.

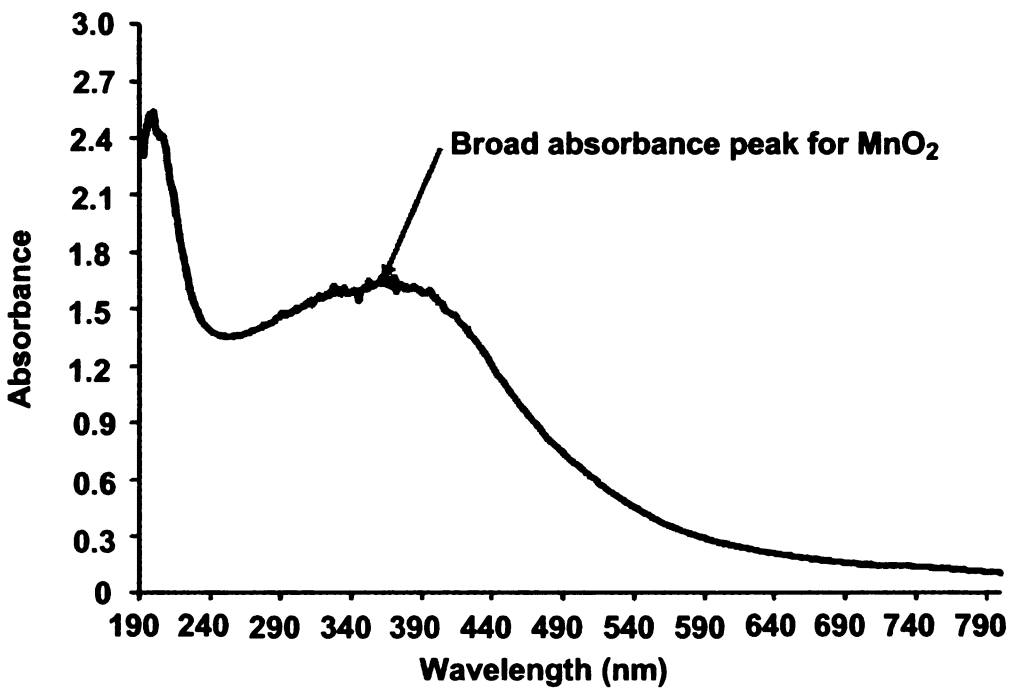

Figure 5. UV-vis absorbance spectrum of manganese oxide prepared by ozonation, confirming the presence of MnO_2.

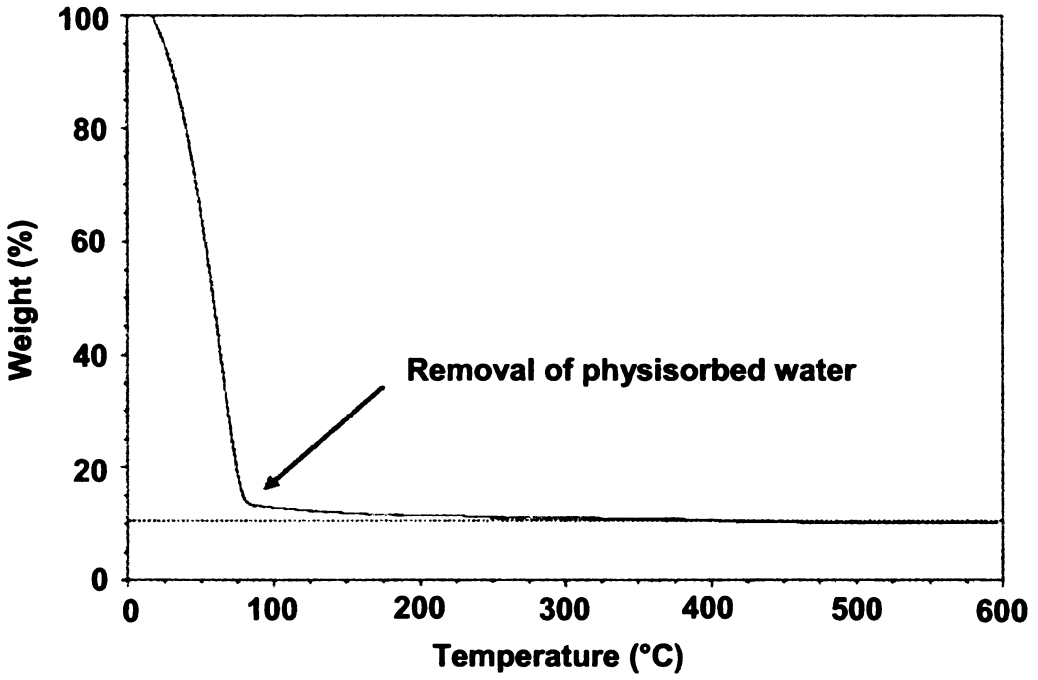

Figure 6. TGA of MnO_2 prepared using ozonation. Physisorbed water is removed at approximately 80°C [112].

3.3.2 CHARACTERIZATION OF SINTERED PARTICLES

Using the results of the formaldoxime, o-tolidine and atomic absorption analyses, the average oxidation state of Mn in the sample sintered at 550°C for 30 minutes was 3.88 ± 0.06 and was 3.08 ± 0.09 in the sample sintered at 500°C for 45 minutes.

Since the wet chemical analysis did not allow for the identification of the sintered samples as exactly MnO_2 or Mn_2O_3, XPS analysis was performed on the sintered samples to determine the oxidation state of the Mn. The Mn 2p3 binding energy

peak for the sample sintered at 550°C for 30 minutes was 641.7 eV, while for the sample sintered at 500°C for 45 minutes, was 642.3 eV (Figure 7). The Mn 2p3 peak for MnO_2 is at 642.5 eV, while for Mn_2O_3, the peak is at 641.6 eV.

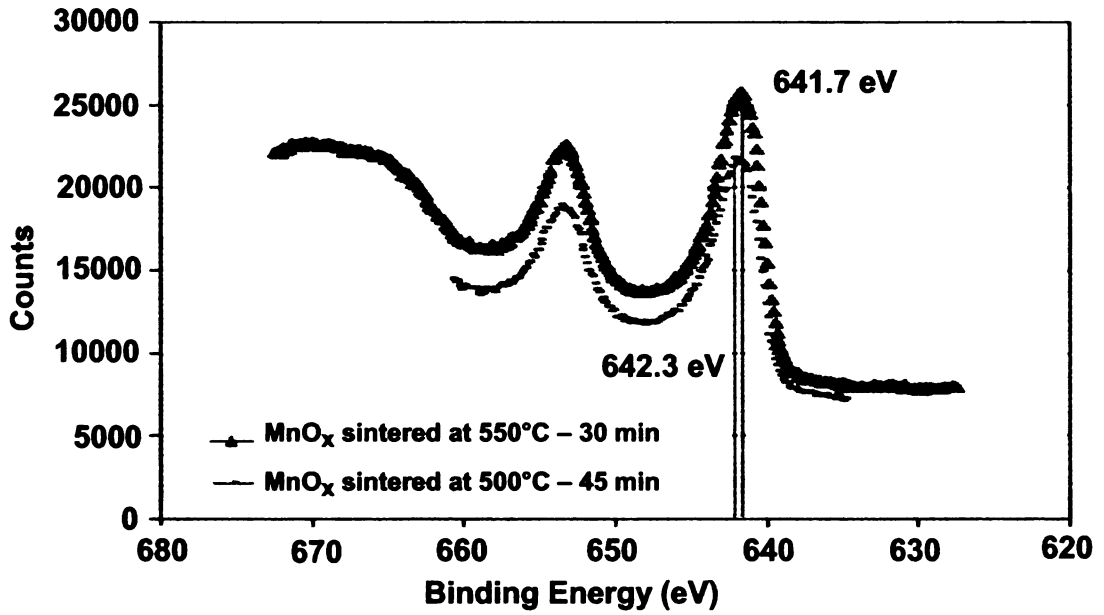

Figure 7. XPS results from the MnO_x samples that were pressed and sintered at 550°C for 30 minutes and at 500°C for 45 minutes showing peaks at 641.7 eV and 642.3 eV, respectively.

Using XRD, all of the peaks for both sintered samples, as well as the purchased Mn_2O_3 were indexed as α-Mn_2O_3, while the purchased MnO_2 that was not sintered was indexed as MnO_2 (pyrolusite), as shown in Figure 8. Therefore, sintering of the hydrated MnO_2 at either 500°C for 45 minutes or 550°C for 30 minutes resulted in a reduction to α-Mn_2O_3.

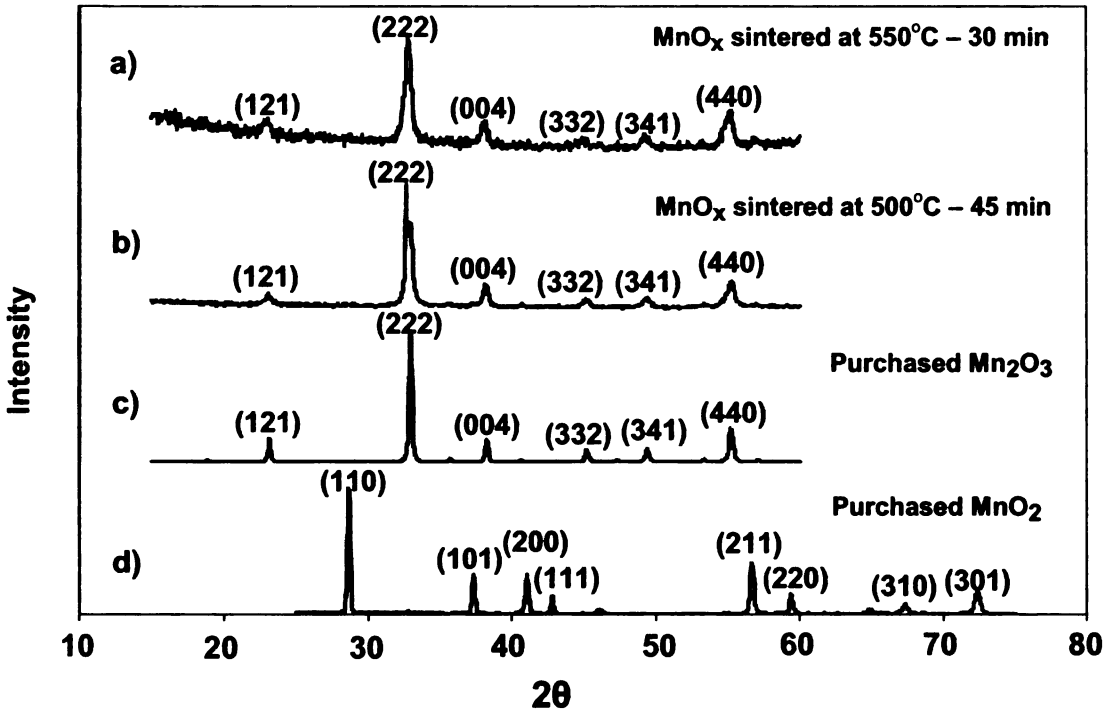

Figure 8. XRD results from manganese oxide that was pressed and sintered a) at 550°C for 30 minutes, b) at 500°C for 45 minutes, c) purchased Mn_2O_3 that is unsintered and d) purchased MnO_2 that is unsintered.

TEM microscopy and selected area diffraction (SAD) were also used to characterize the sintered particles. Figure 9 is a representative TEM micrograph of the manganese oxide sintered at 500°C for 45 minutes. The inset (Figure 9, inset at the top right) of the SAD pattern (100 nm aperture, 100 cm camera length) shows a polycrystalline ring pattern. The ring pattern was indexed as α-Mn_2O_3 (measurements were made with Simple Measure software, JEOL, Tokyo, Japan). Although the sintering temperature was below 550°C, the MnO_2 was still reduced to Mn_2O_3 during the sintering process, most likely due to the greater reactivity of the nanoparticles as compared to typical micron-sized particulate

sintering behavior [108, 109]. As shown in Figure 10, the particles of the sintered material are now smaller in size (average particle size 21 nm ± 5 nm) than the gel that was initially prepared. The removal of the physisorbed water and the rearrangement of the atoms from the hydrated MnO_2 gel structure to the crystalline structure with the concomitant reduction to α-Mn_2O_3, results in the decrease in particle size during sintering.

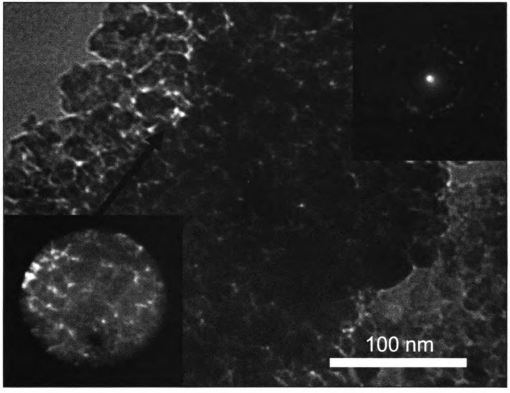

Figure 9. TEM micrograph of the manganese oxide prepared by ozonation, sintered at 500°C for 45 minutes. Inset is the selected area and diffraction pattern showing polycrystalline ring pattern (100 nm aperture).

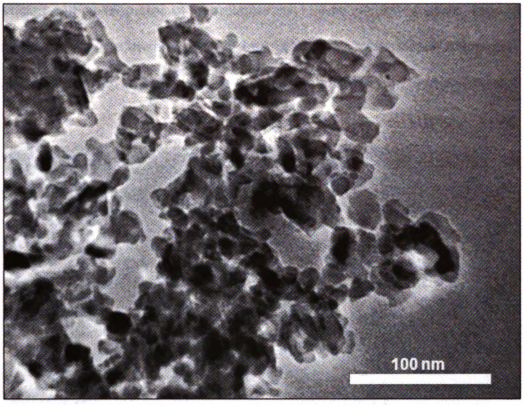

Figure 10. TEM micrograph of the manganese oxide prepared by ozonation and sintered at 500°C for 45 minutes, with an average particle size of 21 nm ± 5 nm.

3.3.3 CHARACTERIZATION OF PARTICLES PREPARED BY MIXING OF $KMnO_4$ AND PAH

To compare the effects of coating the membranes with MnO_2 nanoparticles that have a smaller initial particle size, a second method was used to prepare the colloid. This second method for preparing manganese oxide involved the mixing of $KMnO_4$ and PAH solutions [49]. This procedure yielded uniform spherical

particles with a diameter of approximately 11 nm ± 1 nm (Figure 11). This is consistent with the observations of Luo [49] who reported particles with a size distribution from 6 – 12 nm with the mode for the distribution being 10 nm.

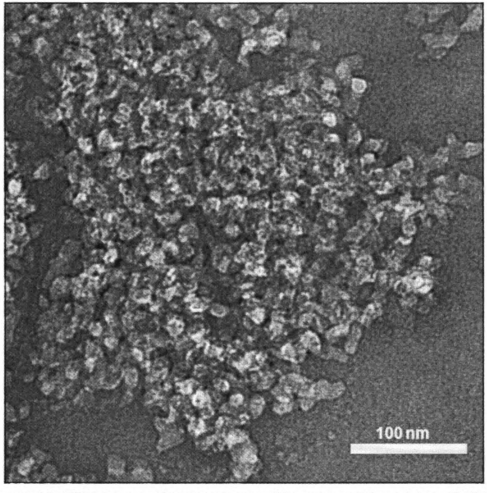

Figure 11. TEM image of manganese oxide prepared by mixing of $KMnO_4$ and poly(allylamine hydrochloride) (unsintered particles), with an average particle size of 11 nm ± 1 nm.

To confirm that the manganese oxide prepared using this method was in fact MnO_2, UV-vis absorption spectroscopy was used. The UV-vis spectrum (in Figure 12) shows the initial peaks centered at 315 nm, 525 nm and 545 nm from

the $KMnO_4$ (red curve), being replaced with a broad peak at 340 nm for the sample that was mixed with the PAH (black curve). This is indicative of the presence of MnO_2 [45, 46, 49]. These results are consistent with the results of Luo [49] where the time-dependent UV-vis spectra showed a gradual decline in the peaks at 315 nm, 525 nm and 545 nm with the gradual appearance of a new peak at 370 nm.

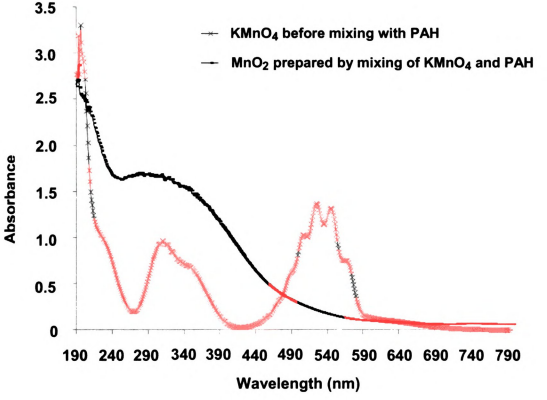

Figure 12. UV-vis absorbance spectrum of $KMnO_4$ before mixing with PAH and MnO_2 prepared by mixing of $KMnO_4$ and PAH. The broad peak at 340 nm is indicative of MnO_2 [45, 46, 49].

Both methods of preparing the manganese oxides resulted in nanoparticles of MnO_2. The method of mixing $KMnO_4$ and PAH resulted in MnO_2 nanoparticles of a much finer particle size (11 nm ± 1 nm) than the particles produced by ozonation (92 nm ± 14 nm), however, the particles prepared by mixing of $KMnO_4$ and PAH are highly agglomerated.

3.4 CONCLUSIONS

A novel method was used to produce manganese oxide nanoparticles. The ozonation of Mn(II) resulted in the formation of highly irregular flakes of hydrated MnO_2, as confirmed by TEM, UV-vis absorption spectroscopy and TGA. The average size of the hydrated particles was 92 nm ± 13 nm. Physisorbed water was driven off at approximately 80°C.

The determination of the phase of the pressed and sintered (at 500°C for 45 min or 550°C for 30 min) particles was inconclusive using wet chemical analysis and XPS. The manganese oxide in the sintered samples was identified as α-Mn_2O_3 using XRD and SAD. Although the 500°C sintering temperature was chosen to avoid the reduction of MnO_2, the nanoparticles did reduce to α-Mn_2O_3 upon sintering, even at the lower temperature.

Removal of the physisorbed water and the rearrangement of the atoms from the hydrated MnO_2 gel structure to the crystalline structure during the reduction to α-Mn_2O_3, resulted in a decrease in the particle size during sintering. The average size of the resulting sintered particles was 21 nm ± 5 nm.

The mixing of $KMnO_4$ and PAH solutions resulted in MnO_2 nanoparticles, as determined by UV-vis absorption spectroscopy. These particles were quite uniform in size and shape, with an average diameter of 11 nm ± 1 nm, although highly agglomerated.

CHAPTER 4

CATALYTIC MEMBRANE PREPARATION AND CHARACTERIZATION

4.1 INTRODUCTION

Coating a membrane with manganese oxide is expected to produce a catalytic surface, which in the presence of ozone, will reduce fouling caused by natural organic matter (NOM) that deposits on the membrane surface. The deposition of NOM on membranes changes the contact angle, surface charge and hydrophilicity of the membranes [61, 113-116].

Jucker and Clark [113] have shown that as the mass of hydrophilic humic substances on the surface of a membrane increases, the contact angle decreases. A decrease in the contact angle indicates an increase in the membrane hydrophilicity [113]. However, Violleau et al. [116] have shown that the wettability of fouled membranes follow the hydrophilic or hydrophobic nature

of the foulants. In addition to being influenced by the humic substances, the wettability of fouled membranes is also influenced by the membrane material [113, 114, 116-138].

Yuan and Zydney [115] have shown that the deposition of humic acid during fouling occurs primarily on the surface of the polyethersulfone (PES) polymeric membrane, rather than in the pore structure. This humic acid deposition on the surface of the membrane has the effect of changing the wettability of the membrane [115].

The flux decline during filtration of humic acids is due to several factors. It is a result of the adsorption of humic acid on or within the pores of the membrane, humic acid deposition during filtration and humic acid concentration polarization [115]. Yuan and Zydney [115], determined that the fouling is dominated by humic acid deposition for higher molecular weight cutoff membranes while the effects of concentration polarization dominate the fouling behavior for smaller pore size membranes. They also determined that humic acid adsorption had only a small contribution (<7%) to the flux decline due to the electrostatic repulsion between the negatively charged humic acid and the negatively charge PES membranes (at pH 7). Although the humic acid adsorption did not result large flux declines, it did contribute to large changes in the contact angle of the membranes [115]. After humic acid filtration, the contact angle increased 44° to 74°. These results of Yuan and Zydney indicate that there is a thin layer of humic acid adsorption

within the membrane pores although the humic acid deposition is primarily on the upper surface of the membrane [115].

Ozone is a powerful oxidant that has a high reactivity with NOM, mainly reacting with double bonds, activated aromatic systems and non-protonated amines [63, 139]. The reaction of ozone with NOM has been shown to reduce membrane fouling [2, 3, 54, 57, 59, 65].

When ozone is added to NOM containing waters, the rate of ozone consumption is faster than when ozone is added to non-NOM containing waters [140]. Westerhoff et al. [140] found that 60% of the ozone was consumed during the first minute when ozone was added to NOM containing water. The initial oxidation reactions, such as ring cleavage, result in the formation of new reactions sites during ozonation [140]. These oxidation products as well as the slower-reacting NOM sites (such as carbon-carbon single bonds) are responsible for the slower second-phase of ozone decomposition [140].

With low ozone doses, Zhu et al. [141] showed that the zeta potential of the suspended particles in the source water (secondary effluent from BeiXiaoHe waste water treatment plant, Beijing, China) to be lower, resulting in aggregation of particles. Increasing the ozone treatment time resulted in further oxygenation of the organic matter, increasing the absolute value of the zeta potential, decreasing the aggregation of the particles [141].

The degradation of organic matter by ozone and the breakdown of larger particles into smaller ones results in decreased membrane fouling [63, 65, 139-142]. The decrease in fouling is due to a reduction in the filtration cake layer formation [65, 141]. The resistance of the filtration cake results in a reduction in the flux through the membranes [65, 141].

Surface modification, such as the addition of coatings, affects the surface morphology of coated ceramic membranes [4, 143-149]. An increase in the roughness of the membrane surface has been shown to increase contact angles, increasing the hydrophobic nature of the membrane [113, 150]. Also, modification of the surface charges on ceramic membranes will change the contact angle as well as the separation performance of the membrane [151-153].

The surface of an oxide will contain a layer of hydroxyl groups, which will cause the surface to acquire a positive charge in an aqueous solution that has a pH less than the isoelectric point (IEP) of the oxide [154]. If the pH of the aqueous solution is higher than the IEP of the oxide, the surface will acquire a negative charge [154]. Since fouling is promoted by the absorption of ions or solute components to the surface of the membrane [155], the surface charge of the membrane affects its fouling performance.

The streaming potential is a method of determining the surface charge on membranes [155]. The streaming potential of multilayered membranes, however, are a combination of the streaming potentials of the multiple layers of the membrane since the different layers can have different charges in aqueous solutions [155]. The addition of a coating layer to the ceramic membranes will affect the overall streaming potential of the membrane. The work presented in this chapter will describe the surface morphology characterization of the coated and sintered ceramic membranes. The streaming potential was not measured in this particular work. However, additional studies should be completed to determine the effects of the surface coating on the streaming potential of the membranes.

In addition to the surface changes that result from the application of a coating to the membrane, the sintering of the coated membrane can also affect the surface morphology of the membrane [4, 68]. Characterization of the coated membranes is necessary [156-158] to determine the effects of the coating and sintering on the roughness, grain size and pore size of the filtration surface. Researchers have characterized membranes using AFM, SEM and TEM to study pore size [4, 144-147], roughness [4, 144-146] and grain size [4, 147].

This chapter discusses the effect of particle preparation method, the number of coating layers and the sintering temperature and time on the structure of the resulting catalytic coating. Atomic force microscopy (AFM), scanning electron

microscopy (SEM), energy dispersive x-ray spectroscopy (EDS) and transmission electron microscopy were used to characterize the surface morphology and topography as well as the coating thickness of manganese oxide coated ceramic membranes.

4.2 MATERIALS AND METHODS

Manganese oxide colloids were prepared by ozonation and by mixing of $KMnO_4$ and PAH using the methods described in Chapter 3.

4.2.1 LAYER-BY-LAYER COATING OF MEMBRANES

The particles produced using ozonation were washed and dispersed before use. First, centrifugation (ThermoForma General Purpose Centrifuge, Thermo Scientific, Waltham, MA, 30 min at 2500 rpm) was used to settle the MnO_2 particles and the supernatant was subsequently decanted and discarded. The solids were then mixed with 10^{-4} N KNO_3 (≥99.0%, J.T. Baker Co., Phillipsburg, NJ), and sonicated (58 W, Branson Ultrasonics Corporation Model 250 Sonifier, Danbury, CT) for 30 min in an ice bath to disperse the nanoparticles.

A layer-by-layer technique developed by Lvov et al. [91] and Espinal et al. [94] was used to coat the ceramic membranes with manganese oxide nanoparticles. The coating procedure was as follows: the ceramic membrane was immersed for 15 min in a 0.2 wt% poly(diallyldimethylammonium chloride) (PDDA) solution (Aldrich, average MW < 100,000), then rinsed for 15 s with 0.01 M NaOH (≥98.0%, J.T. Baker Co., pH 12), immersed for 15 min in the manganese oxide suspension and rinsed for 15 s with 0.01 M NaOH. This sequence produced one layer. The sequence was then repeated to obtain the desired number of layers of nanoparticles. After coating, the membrane was sintered in air at either 550°C for 30 min or 500°C for 45 min (temperature ramping up at a rate of approximately 10°C/min and allowed to free cool over 8 hours).

The ceramic membrane (INSIDE CéRAM, TAMI North America, St. Laurent, Québec, Canada) had a tubular design with 7-channels, and as documented on the TAMI website [159], composed of a titanium oxide ceramic support with a titanium oxide filtration layer (although EDS also shows zirconium oxide present on the surface of the membrane). The outside diameter of the membrane was 1 cm with a length of 25 cm. The nominal molecular weight cut-off was 5 kDa.

4.2.2 MICROSCOPY SAMPLE PREPARATION

A schematic representation of the AFM sample preparation is given in Figure 13a. AFM sample preparation started with cutting a 1 mm thick cross section from the coated membrane using a diamond-wafering saw. An arc-shaped specimen taken from this section was mounted on a stainless steel disc (12 mm in diameter) using double-sided adhesive tabs so that the manganese oxide coated surface was pointing upward.

AFM images were obtained using a Nanoscope III Multimode Atomic Force Microscope (Digital Instruments Inc.) in air, using the contact mode. A triangular Si_3N_4 NP probe (Veeco Instruments, CA), with a nominal cantilever spring constant of 0.12 N/m and nominal frequency of 20 kHz, was used. The tip height was 2.5 μm to 3.5 μm, with a nominal radius of 20 nm and a side angle of 35°. Five different areas, of dimension 20 μm x 20 μm, were scanned at a rate of 0.5 Hz on each sample so that average values could be determined for the roughness and height of each sample.

AFM roughness and height data was obtained using the Nanoscope program (Nanoscope 5.30 r3 sr3, Veeco Instruments, CA). The average roughness (R_a) for the image is defined as the arithmetic average of the absolute values of the surface height deviations measured from the mean plane, rather than the frequency or spacing of the features. The height comparisons were performed

using the maximum roughness (R_{max}), defined as the maximum vertical distance between the highest and lowest data points in the image.

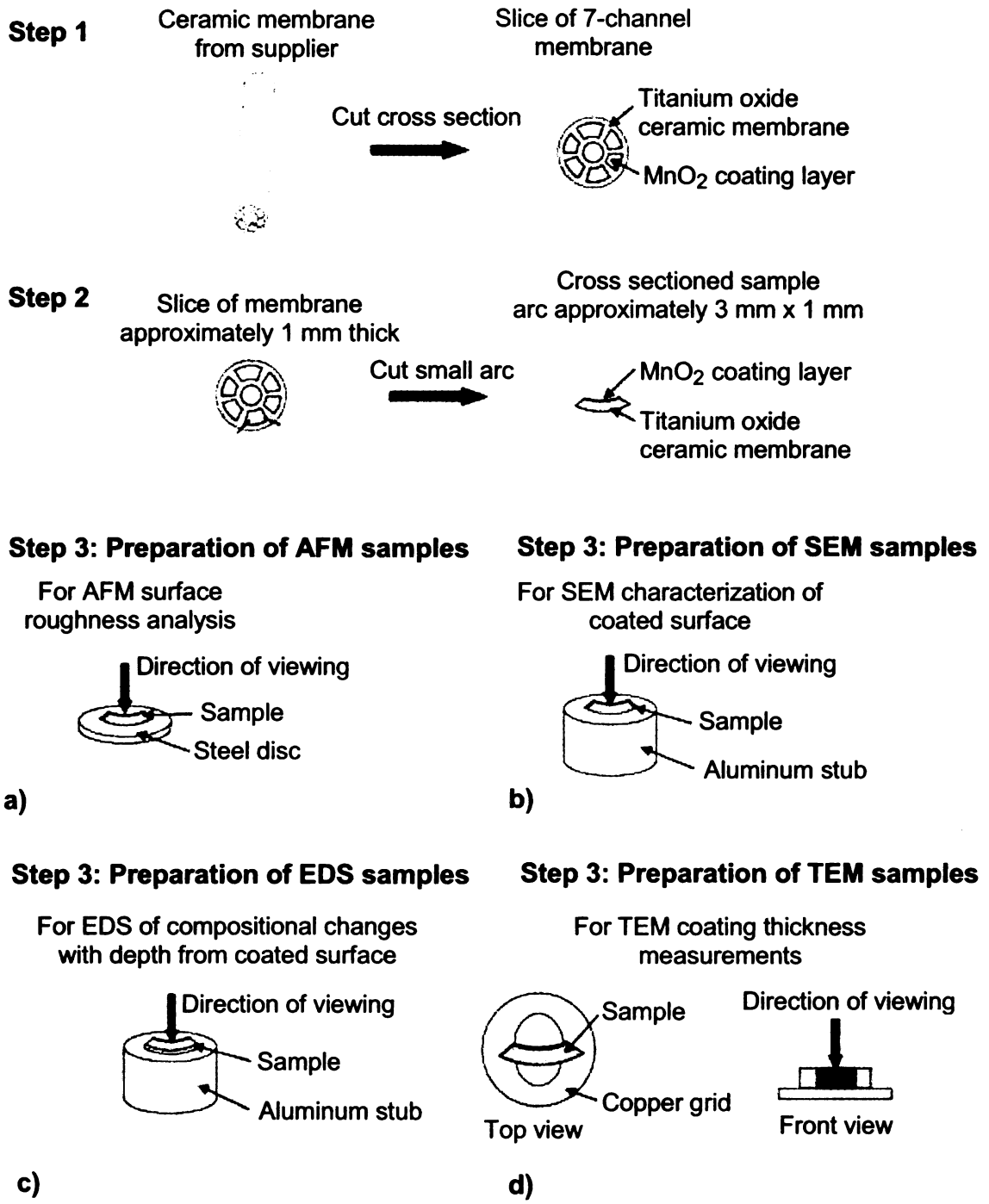

Figure 13. Schematic representation of the sample preparation for a) AFM, b) SEM, c) EDS and d) TEM.

Fourier transform analysis (MATLAB R2008b, The MathWorks, Natick, MA) was also used to analyze AFM images. To look for possible changes in amplitude or frequency of the surface features, 30 AFM line scans were analyzed per sample using the fast Fourier transform (FFT) function. The Fourier transforms were plotted and the amplitude and frequencies of the surface features were compared.

In a similar method as for the AFM samples, SEM samples were prepared by cutting a 1 mm thick cross section from the coated membrane using a diamond-wafering saw. This section was then cut into a small arc-shaped specimen of approximately 3 mm in length. The arc-shaped specimen was then placed on an aluminum SEM stub with carbon tape, so that the coated surface of the membrane was pointing upward. A schematic representation of the SEM sample preparation is given in Figure 13b.

A schematic representation of the EDS sample preparation is given in Figure 13c. Samples were prepared so that the small arc-shaped portions of the membrane were placed flat on the aluminum stub such that the cross sectional surface of the membrane was pointing upward so that the depth of penetration of the manganese into the membrane could be observed using EDS. In this manner, a map of the spatial distribution of manganese within the sample was determined.

Since the samples were non-conductive, they were gold-coated for SEM and carbon-coated for the EDS analyses. A layer of gold was applied using a gold sputter coater (Emscope SC 500, Ashford, Kent, Great Britain) at a rate of 7 nm/min, with a current of 20 mA, for a total thickness of approximately 21 nm. For EDS analysis, the samples were carbon-coated using a carbon string evaporator (EFFA Mk II carbon coater, Ernest Fullam Inc., Latham, NY), since the gold coating would interfere with the detection of the surface elements.

SEM micrographs were obtained using a JEOL 6400V SEM (Japan Electron Optics Laboratories, Tokyo, Japan) with a LaB_6 emitter (Noran EDS, Noran Instruments Inc., Middleton, WI) at an accelerating voltage of 15 kV and magnification of 25,000x. Average grain size measurements were calculated from five SEM micrographs of each sample using the intercept method (ASTM Standard E 112-96 (2004)) where an average of 200 grains were measured per micrograph. A Noran EDS analyzer (Noran Instruments Inc., Middleton, WI, accelerating voltage of 20 kV and magnification of 1,000x) was used for EDS microanalysis.

TEM analysis was used to characterize the microstructure, the coating thickness and the phase of manganese oxide present on the surface of the coated ceramic membranes. XRD was not used to determine the phase of the manganese oxide on the surface of the membrane (as it had been used to determine the phase of the sintered particles in Chapter 3) since the penetration of the x-ray beam into

the sample would not allow for accurate determination of the very thin surface layer of manganese oxide. A schematic representation of the process used to prepare the TEM samples is given in Figure 13d. To prepare TEM grids, a diamond-wafering saw was used to slice the membrane into a thin wafer, approximately 1 mm thick. This thin wafer was then cut into an arc, approximately 3 mm long, using a razor blade. The arc was mounted on a stub in order to thin and was hand polished using 15 μm then 5 μm polishing paper, followed by 6 μm, 3 μm and 1 μm diamond paste. The polished surface was then mounted face down on a slotted copper TEM grid (3 mm outer diameter) and the entire grid and sample were mounted on a stub for further polishing, using the same sequence of successively finer polishing paper and diamond paste, until a thickness of approximately 100 μm was achieved.

The sample was then dimpled (GATAN Precision Dimple Grinder, Model 656, Pleasanton, CA) to thin the center to approximately 50 μm, while avoiding damage to the outer portion of the sample and then ion milled (GATAN Precision Polishing System Model 691, Pleasanton, CA) at an accelerating voltage of 4.0 keV and a beam inclination angle of 4° until a hole just started to form at the center of the coated membrane surface. The final specimens were examined using a TEM (JEOL 2200FS, Tokyo, Japan, 200 kV accelerating voltage). Photomicrographs were collected using a Hamamatsu CCD digital camera (Hamamatsu City, Japan) to observe the layered structure of the ceramic membranes. Selected area diffraction patterns were collected using a

nanoaperture of 100 nm in diameter and a camera length of 100 cm and indexed (using the Simple Measure software, JEOL, Tokyo, Japan) to identify the manganese oxide phase present on the surface of the coated membrane.

One-way ANOVA testing, with Tukey's mean comparison tests (95% confidence interval) (Minitab statistical software, Minitab Inc.), was used to determine if differences in feature heights, roughness and grain size measurements were statistically significant.

4.3 RESULTS AND DISCUSSION

4.3.1 ATOMIC FORCE MICROSCOPY (AFM) ANALYSIS

AFM analysis was performed on membranes that were 1) as received, 2) uncoated and sintered at 500°C and at 550°C, 3) coated with manganese oxide prepared using ozone with 20 layers and sintered at 500°C and 550°C, 4) coated with 30 and 40 layers and sintered at 500°C, 5) coated with manganese oxide prepared by mixing of $KMnO_4$ and PAH with 20 layers and sintered at 500°C and 550°C and 6) coated with 30 layers and sintered at 550°C.

The feature height, determined by AFM imaging (the average and standard deviation of the R_{max} for 5 different 20 μm x 20 μm areas of each sample) is shown in Figure 14.

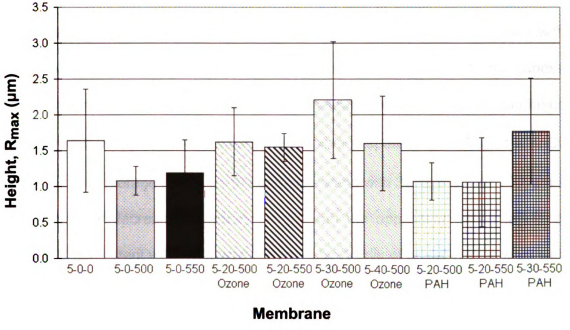

Figure 14. Feature height data from AFM images of membranes that were uncoated or coated and sintered at various conditions. The nomenclature for the naming of the samples is that the first number is the molecular weight cut-off of the membrane (e. g. 5 kDa), the second is the number of coating layers and the third is the sintering temperature (in °C, where 0 indicates that the membrane was unsintered). For the coated membranes, the word ozone after the name of the sample indicates that the manganese oxide particles were prepared using ozonation while PAH indicates that the manganese oxide particles were prepared by mixing of $KMnO_4$ and PAH. Error bars indicate the standard deviation based on 5 different scans of each sample.

Although not statistically significant, the means show differences in feature heights. For example, upon sintering an uncoated sample (average height 1.64 μm ± 0.72 μm), there is a decrease in the feature height (average heights for the

sample sintered at 500°C and at 550°C are 1.08 μm ± 0.20 μm and 1.19 μm ± 0.46 μm, respectively). This decrease in feature height is to be expected since the partial pressure of the diffusing species is higher over a convex surface, such that there is a driving force during sintering that causes atoms to move from the convex to the concave areas [97]. As the number of manganese oxide layers increases from 20 to 30, the feature height also increases, then decreases with 40 layers. The height is greatest for the membrane coated with 30 manganese oxide layers prepared using ozone, with the average height for this sample being 2.21 μm ± 0.82 μm. With the manganese oxide prepared by mixing of $KMnO_4$ and PAH, the average height for the sample coated with 30 layers was 1.77 μm ± 0.74 μm. This decrease in feature height with the application of 40 layers of coating is consistent with what was observed by Karnik et al. [4] in their work with Fe_2O_3 coated ceramic membranes. The decrease in feature height with the application of 40 layers is likely due to the coating material filling the valleys between the features, having the effect of reducing the overall feature height with increasing number of coating layers.

The roughness data for all membranes is shown in Figure 15. Trends similar to those observed for the maximum feature height were observed for the roughness data. The differences in roughness were not statistically significant. There was a decrease in overall roughness when the uncoated membrane (average roughness 150 nm ± 57 nm) was sintered. The roughness of the membrane sintered at 500°C (average roughness 111 nm ± 9 nm) was less than the

membrane sintered at 550°C (average roughness 146 nm ± 56 nm). The decrease in roughness due to sintering is also expected expected since the partial pressure of the diffusing species is higher over a convex peaks on the sample, with the driving force during sintering causing atoms to move from the convex to the concave valleys [97]. Although the mean of the roughness for the sample sintered at 550°C is higher than the sample sintered at 500°C, the statistically there is no difference due to the high deviation in the roughness for the sample sintered at 550°C. As the number of layers of the manganese oxide particles was increased, there was little change in roughness of the samples. The roughness was greatest for the membrane coated with 30 layers of the manganese oxide particles prepared using ozone, with the average roughness for this sample being 170 nm ± 43 nm, while with the manganese oxide prepared by mixing of $KMnO_4$ and PAH, the average roughness for the sample coated with 30 layers is 150 nm ± 59 nm. This is consistent with the results of Kamik et al. [4] for iron oxide nanoparticle layers on ceramic water filtration membranes and Reilly et al. [160] found that for multilayer films of polyelectrolyte molecules on glass slides, there was little change in roughness with an increasing number of coating layers.

Although the height and roughness of the uncoated membranes decrease after sintering, the number of features appeared to increase (see Figure 16 a-c). The number of features present after coating the membranes with manganese oxide prepared using ozone (Figure 16 d-g) and with manganese oxide prepared by

mixing of $KMnO_4$ and PAH (Figure 16 h-j) and sintering at 500°C and 550°C appeared to increase with the number of coating layers.

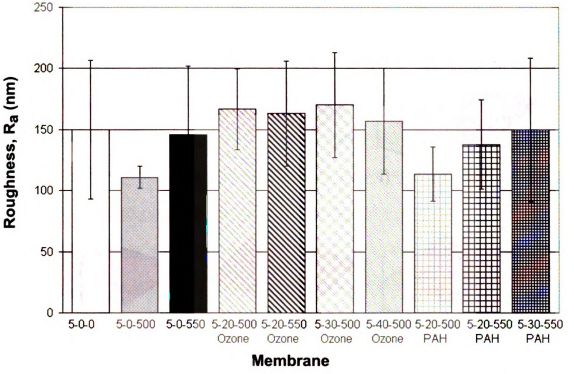

Figure 15. Roughness data based on AFM imaging of membranes that were uncoated or coated and sintered at various conditions. The nomenclature for the naming of the samples is the same as for Figure 14. Error bars indicate the standard deviation based on 5 different scans of each sample.

Fourier transform analysis [161] of line scans of the samples, however, did not show any significant change in the amplitude or frequency of the surface features on any of the samples. In all samples, the highest amplitudes were at the lowest frequencies with a steady decline in amplitude with increasing frequencies. A representative figure of the Fourier transform data for the AFM samples is shown in Appendix A.

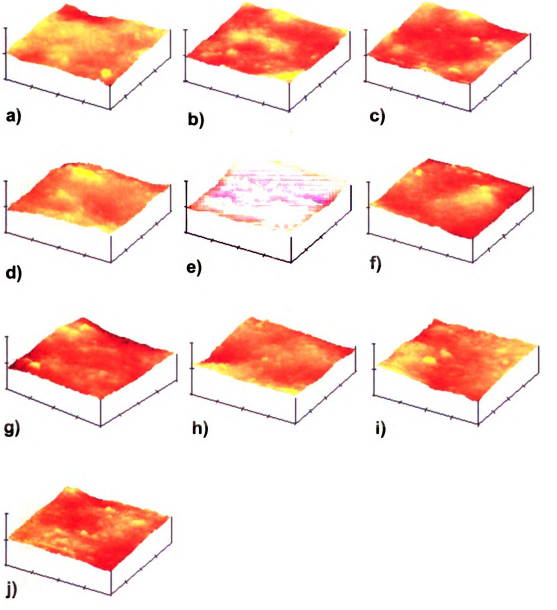

Figure 16. AFM images of ceramic membranes a) 5-0-0, b) 5-0-500, c) 5-0-550, d) 5-20-500 Ozone, e) 5-20-550 Ozone, f) 5-30-500 Ozone, g) 5-40-500 Ozone, h) 5-20-500 PAH, i) 5-20-550 PAH and j) 5-30-550 PAH. The scale for all samples is x: 5.00 µm/division and y: 3000 nm/division. The nomenclature for the naming of the samples is the same as for Figure 14.

The manganese oxide coatings were applied to porous substrates. Other studies of coatings on porous substrates have shown similar changes in surface topography [162-164]. Cai et al. [162] and Shaoqiang et al. [163] observed a decrease in AFM feature height with the application of coatings on porous silicon substrates, due to the partial filling of the coating particles into the pores of the substrate. Ghosh et al. [164] observed an initial increase in the average roughness of a porous silicon substrate with the deposition of an indium tin oxide coating and then a decrease in the average roughness with increasing deposition of the coating.

4.3.2 SCANNING ELECTRON MICROSCOPY (SEM) ANALYSIS

The SEM micrographs of the uncoated and coated ceramic membranes are shown in Figure 17 a-j. Although the difference in grain size is not statistically significantly, analysis of the SEM data showed a similar coarsening of the grains as was seen in the roughness data from the AFM analysis (a summary of the AFM and SEM observations is provided in Table 1). The average grain size for the uncoated membrane increases from 71 nm ± 5.1 nm to 76 nm ± 5.5 nm when the uncoated membranes were sintered at 500°C. The grain size did not change when the uncoated membrane was sintered at 550°C, compared to the unsintered membrane.

For both coating preparation methods, the grain size (where the average size and standard deviation were calculated from five SEM micrographs with an average of 200 grains measured per micrograph) increased as the number of manganese oxide coating layers increased. A statistically significant difference was observed between the grain size for the membrane coated with 40 layers (87nm ± 7.6 nm) of the manganese oxide prepared by ozonation and all other samples (shown in Figure 18). A statistically significant difference was also observed between the grain size for the membrane coated with 30 layers of the manganese oxide prepared by mixing of $KMnO_4$ and PAH (79 nm ± 3.8 nm) and the uncoated and unsintered membrane (71 nm ± 5.1 nm), the uncoated membrane sintered at 550°C (71 nm ± 7.0 nm) and the membrane coated with 20 layers of the manganese oxide prepared by ozonation and sintered at 500°C (72 nm ± 5.8 nm). These observations were consistent with what was observed by Karnik et al. [4] with the Fe_2O_3 coated ceramic membranes, where little change in grain size was seen until 40 layers had been applied.

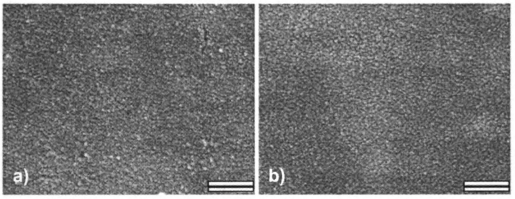

Figure 17. SEM micrographs of ceramic membranes a) 5-0-0, b) 5-0-500, c) 5-0-550, d) 5-20-500 Ozone, e) 5-20-550 Ozone, f) 5-30-500 Ozone, g) 5-40-500 Ozone, h) 5-20-500 PAH, i) 5-20-550 PAH and j) 5-30-550 PAH. The nomenclature for the naming of the samples is the same as for Figure 14.

Figure 17. Continued

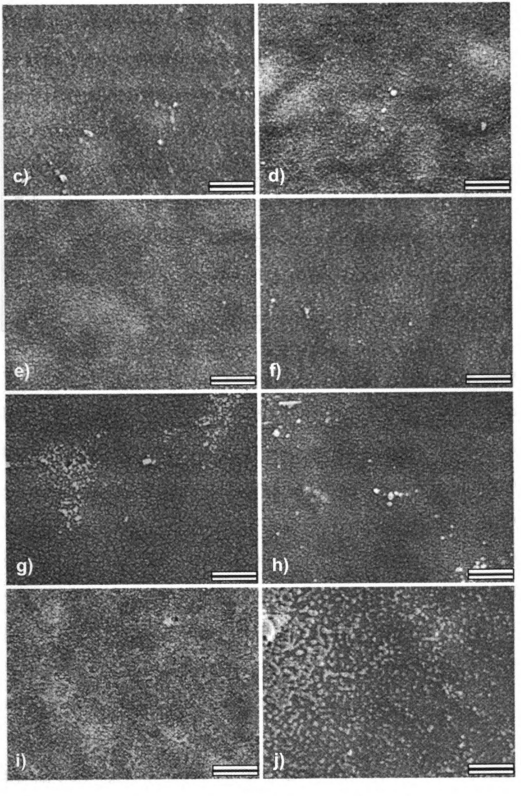

Table 1: Summary of AFM and SEM observations for all membrane samples.

	Parameter	Maximum Feature Height (μm)	Average Roughness (nm)	Average Grain Size (nm)
	Method Used	AFM	AFM	SEM
Membrane	**5-0-0**	1.64 ± 0.72	150 ± 57	71 ± 5.1
	5-0-500	1.08 ± 0.20	111 ± 9	76 ± 5.5
	5-0-550	1.19 ± 0.46	146 ± 56	71 ± 7.0
	5-20-500 Ozone	1.62 ± 0.47	167 ± 33	72 ± 5.8
	5-20-550 Ozone	1.55 ± 0.19	163 ± 43	74 ± 4.9
	5-30-500 Ozone	2.21 ± 0.82	170 ± 43	75 ± 6.3
	5-40-500 Ozone	1.60 ± 0.66	157 ± 43	87 ± 7.6
	5-20-500 PAH	1.07 ± 0.26	114 ± 22	77 ± 4.7
	5-20-550 PAH	1.06 ± 0.62	138 ± 37	75 ± 4.3
	5-30-550 PAH	1.77 ± 0.74	150 ± 59	79 ± 3.8

When comparing membranes with the same sintering conditions, there is an increase in grain growth with increasing coating layers. Since the colloids are prepared and sonicated and then used to coat the membranes; with the additional number of coating layers, the colloids are more likely to have agglomerated by the time that the suspension is used to coat a membrane with a greater number of coating layers (it takes over 20 hours to coat a membrane with 40 layers). The increase in agglomerates as additional material is applied results in the changes in the sintering behavior. The agglomerated particles will sinter together into the larger gains. Sintering of agglomerates does not allow the material to densify and will maintain porosity [97].

During sintering, large grains will grow at the expense of smaller grains and will result in grain coarsening [97, 98, 165, 166]. As the grain boundaries migrate, the

pores between the grains will move with the grain boundaries and coalesce into larger pores at the intersection of grain boundaries [97]. Therefore, sintering of the agglomerates has the effect of coarsening the grains, and subsequently the pores, on the filtration surface of the membrane.

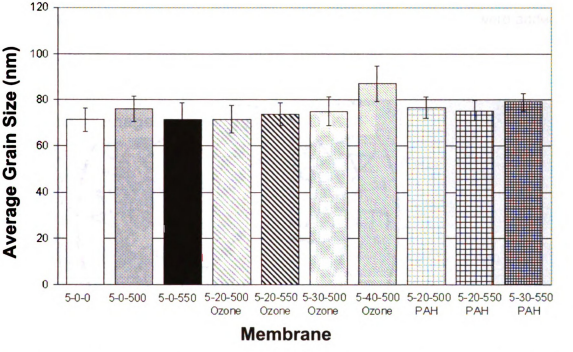

Figure 18. Comparison of grain sizes (calculated using intercept method) for uncoated and coated ceramic filtration membranes. The nomenclature of the naming of the samples is the same as for Figure 14.

4.3.3 ENERGY DISPERSIVE X-RAY SPECTROSCOPY (EDS) ANALYSIS

Energy Dispersive X-ray Spectroscopy (EDS) microanalysis mapping was performed on a cross section of an uncoated ceramic membrane. EDS mapping of the as-received, uncoated and unsintered membrane (Figure 19) showed the

membrane composition to be a porous TiO_2 support with ZrO_2 and TiO_2 on the filtration surface (the filtration surface is on the right hand side of the images). The membrane supplier's product characteristics data, however, describes this membrane as having only a TiO_2 active layer for the 5 kD, INSIDE CéRAM membranes used in this study [159]. The details of the membrane manufacturing are not known, however, it is likely that the small amounts of zirconia were added to aid in the manufacturing process of the filtration layer.

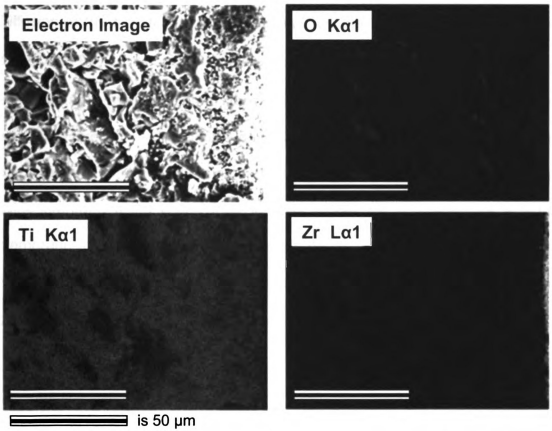

Figure 19. EDS mapping image of uncoated and unsintered ceramic membrane. The filtration surface is on the right hand side of the images.

Cross-sectioned samples of the membranes coated with 40 layers of the manganese oxide prepared using ozone and 30 layers of the manganese oxide prepared by mixing of $KMnO_4$ and PAH were analyzed with EDS mapping (Figure 20). The Mn elemental map clearly demonstrates that Mn is present throughout the membrane, rather than remaining on the filtration surface. Thus, the manganese oxide nanoparticles have penetrated into the membrane, adding to the catalytic ability of the membrane.

Diffusion of the manganese oxide coatings into the membrane is similar to the diffusion of Fe_2O_3 nanoparticles in the alumina-zirconia-titania (AZT) membranes used by Karnik et al. [4]. The uniform diffusion of manganese into the membrane was confirmed by a quantitative analysis of the EDS line scans of the coated membranes (Figure 21). The membrane coated with 30 layers of the manganese oxide prepared using ozone tend to have higher Mn counts further into the membrane (the data was normalized based on Mn counts at the surface of each membrane sample) than the membrane coated with 30 layers of the manganese oxide prepared by mixing of $KMnO_4$ and PAH.

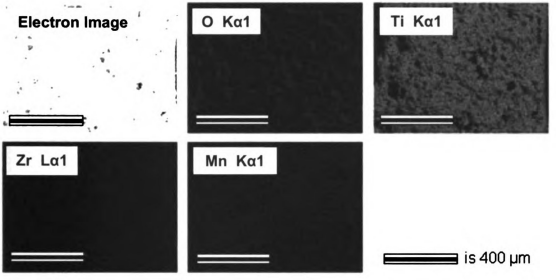

a) 5-40-500 Ozone

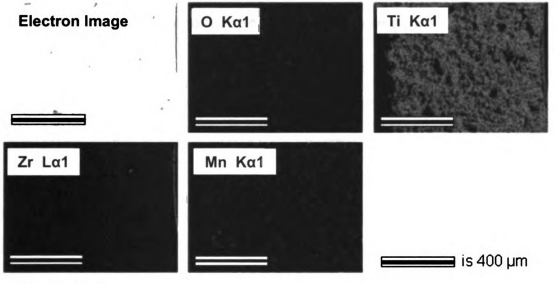

b) 5-30-550 PAH

Figure 20. EDS mapping image of 5 kDa ceramic membrane a) coated with 40 layers of the MnO_2 coating prepared using ozone and sintered at 500°C for 45 min and b) coated with 30 layers of MnO_2 prepared by mixing of $KMnO_4$ and PAH and sintered at 550°C for 30 min. The MnO_2 coated filtration surface is on the right hand side of the images.

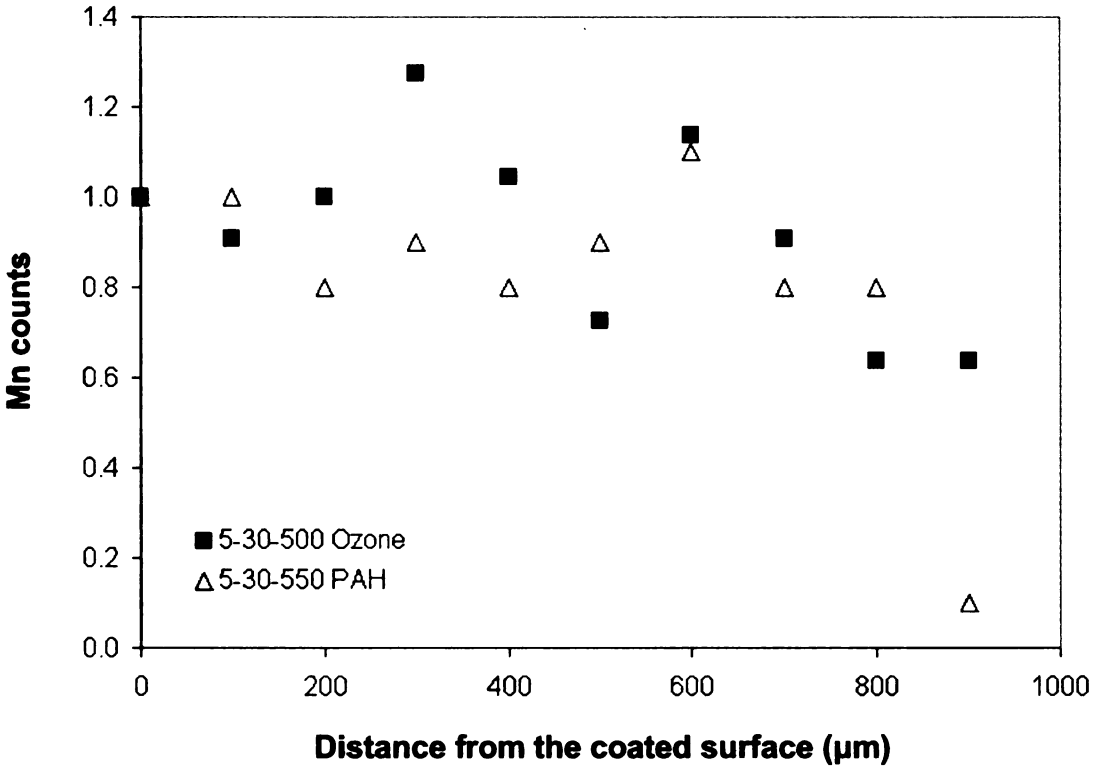

Figure 21. EDS line scan of 5 kDa ceramic membrane coated with 30 layers of the manganese oxide coating prepared using ozone and sintered at 500°C for 45 min and with 30 layers of manganese oxide prepared by mixing of $KMnO_4$ and PAH and sintered at 550°C for 30 min. EDS line scan counts were normalized based on Mn counts at the surface of each membrane sample.

Since Mn was seen throughout the membrane after coating and sintering, an estimate of the diffusivity has been calculated. Using equation (2), the diffusivity, D, can be estimated using the diffusion coefficient, Do, and the activation energy, Q, for a transition metal in an oxide host (D_o = 1.8 x 10^{-9} m^2/s, Q = 202 x 10^3 J/mol [167], for Ni in MgO) at a temperature of 500°C (773 K), the resulting diffusivity is 4.0 x 10^{-23} m^2/s (calculations provided in Appendix B).

$$D = D_O \exp\left(\frac{-Q}{RT}\right) \qquad (2)$$

Using equation (3), an estimate of the diffusivity can be calculated for diffusion across the entire membrane wall thickness (1 mm) for a sintering time of 45 minutes (2700 s). This would require a diffusivity of 3.7×10^{-7} m^2/s (calculations provided in Appendix B). This is 16 orders of magnitude higher than the diffusivity estimated for a transition metal in an oxide host.

$$x \approx \sqrt{Dt} \qquad (3)$$

If equation (3) is used to determine the diffusion distance using the diffusivity estimated for a transition metal in an oxide host, for a sintering time of 45 minutes, the resulting diffusion distance is 0.33 nm (calculations provided in Appendix B). This diffusion distance would not explain the presence of Mn throughout the membrane. Therefore, rather than diffusing through the membrane entirely by solid state diffusion, the coating must be dispersed through the membrane during the coating process and then diffuses into the grains of the membrane by solid state diffusion during sintering.

The ceramic membrane is composed of very fine pores on the filtration surface and large pores within the support of the membrane. Liquid filling of a channel is dominated by capillary action due to surface tension as the channel size decreases to the nanoscale [168]. This capillary action draws the coating material through the pores of the filtration layer and into the pores of the support layer of the membrane during the coating process. The coarse membrane support, with high porosity, is shown in Figure 22. During sintering, solid state diffusion allows the manganese oxide coating to diffuse from the pores into the

grains of the membrane, resulting in the distribution of manganese throughout the cross section of the coated membrane.

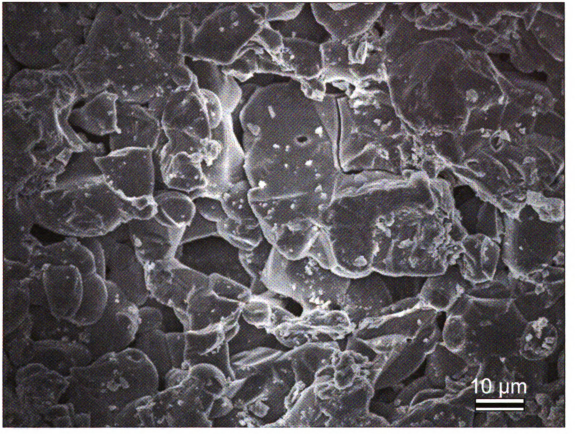

Figure 22. SEM micrograph of the coarse grained membrane support layer with high porosity.

The large particle size of the as prepared MnO_2, however, would be too large to fit through the small pores (approximately 1.5 nm) on the filtration surface of the membrane. Therefore, for the Mn to be present throughout the membrane, there must be some residual Mn ions present in the colloid that is used for coating the membranes. To study this, after the MnO_2 was dispersed in the KNO_3 and sonicated, rather than using it to coat a membrane, it was then separated by

centrifugation once again and the resulting supernatant was used to coat a membrane. The EDS map of a membrane coated with 10 layers of this supernatant and sintered at 500°C for 45 minutes is shown in Figure 23. The presence of Mn throughout the membrane indicates that the Mn ions that are in the MnO_2 suspension disperse into the pore structure of the membrane during coating then diffuse into the grains of the membrane during sintering.

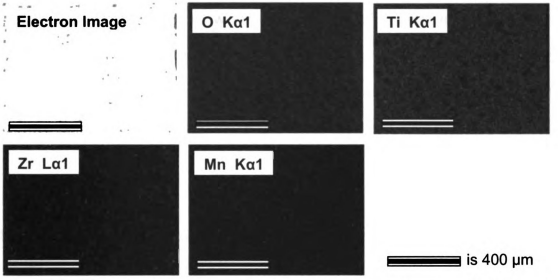

Figure 23. EDS mapping image of a 5 kDa ceramic membrane coated with 10 layers of the supernatant from the MnO_2 colloid and sintered at 500°C or 45 minutes, showing Mn present throughout the membrane. The filtration surface is on the right hand side of the images.

Since Mn is present throughout the membrane as well as on the surface, this would serve to improve the long-term performance of the membrane. During service the membrane may wear away [72] and while such wear is much less for ceramic membranes as compared to that observed with polymeric membranes

[72], because Mn has diffused throughout the membrane, enhanced performance would be expected to continue even if the coated surface layer has eroded.

Another advantage to having the catalyst throughout the membrane is that the catalytic activity will be inside the membrane's porosity, not only on the coated surface. This would allow for smaller molecular weight compounds, which pass through the membranes, to be catalytically oxidized by ozone within the pores of the membranes. This will allow for the oxidation of smaller molecular weight compounds without requiring the use of a membrane with a lower molecular weight cut-off (MWCO), since membranes with lower MWCOs require higher operating pressures, which increases the operating costs.

4.3.4 TRANSMISSION ELECTRON MICROSCOPY (TEM) ANALYSIS

Figure 24a shows a TEM photomicrograph of a cross section of an as received membrane. This micrograph reveals the underlying TiO_2 support and the outer filtration layer with a thickness varying from approximately 110 nm to 360 nm. The inset diffraction pattern shows a diffuse ring pattern, indicating that the filtration layer is amorphous. Figure 24b is a TEM photomicrograph of a membrane that was coated with 40 layers of the manganese oxide coating and sintered at 500°C for 45 minutes. This micrograph reveals an uneven coating layer, varying between approximately 20 nm to 73 nm in thickness, over the ZrO_2

filtration layer. The inset diffraction pattern shows a polycrystalline ring pattern, which was indexed as α-Mn_2O_3, which is consistent with the XRD and SAD data of the sintered particles (Figures 8 and 9).

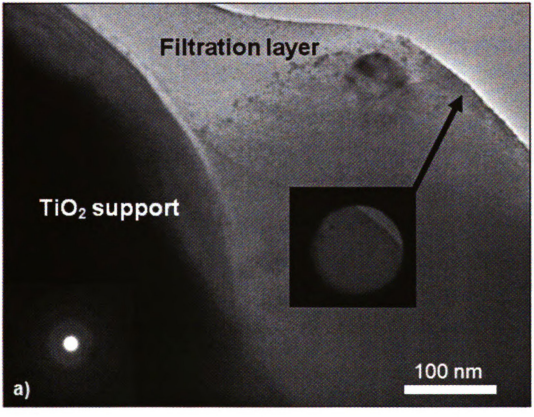

Figure 24. a) TEM photomicrograph of a cross section of an as received ceramic water filtration membrane. Inset are the selected area and the diffraction pattern showing an amorphous ring pattern (100 nm aperture). b) TEM photomicrograph of cross section of a membrane with 40 layers of manganese oxide, sintered at 500°C for 45 minutes. Inset are the selected area and the diffraction pattern showing polycrystalline ring pattern (100 nm aperture).

Figure 24. Continued

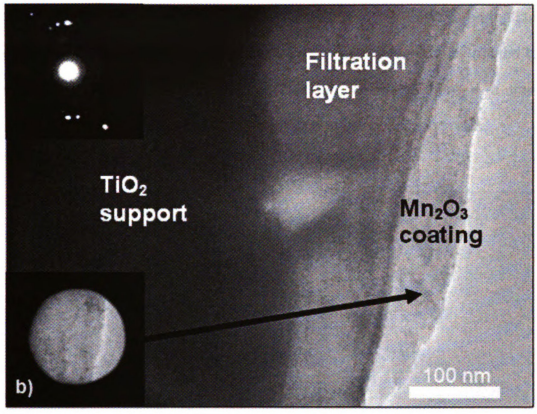

When 20 layers of the manganese oxide were applied to a membrane and sintered, the resulting coating thickness varied between approximately 14 nm to 54 nm (Figure 25). However, when 30 layers were applied, the resulting thickness varies between approximately 19 nm to 110 nm (Figure 26). With an approximately particle size of 20 nm, and assuming a close-packed arrangement of spherical particles, the expected coating thicknesses would be 296 nm, 444 nm and 592 nm, for the 20, 30 and 40 layers, respectively, if the coating remains only on the surface of the membrane (Figure 27). Since the flakes of the hydrated MnO_2 are not spherical, but rather have a higher aspect ratio, the

application of the hydrated MnO_2 flakes does not result in uniform increases in thickness with each coating layer, depending on how the flakes lie on the surface of the membrane. The coating thickness is therefore not directly related to the number of layers applied in a linear fashion, however, there is a trend of increasing coating thickness with increasing number of coating layers.

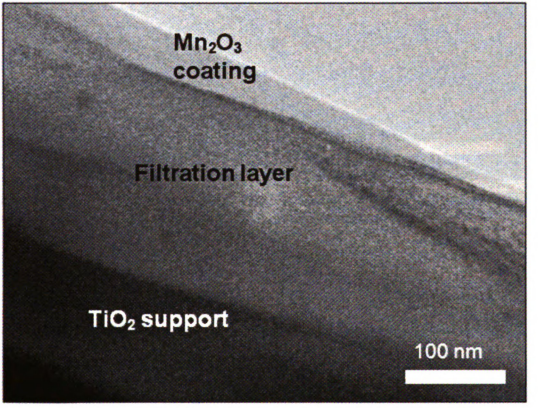

Figure 25. TEM photomicrograph of cross section of a membrane with 20 layers of manganese oxide, sintered at 500°C for 45 minutes.

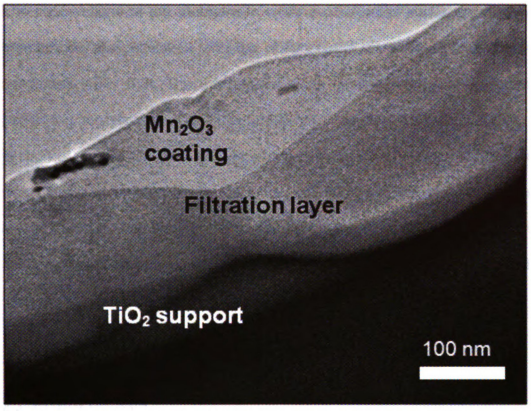

Figure 26. TEM photomicrograph of cross section of a membrane with 30 layers of manganese oxide, sintered at 500°C for 45 minutes.

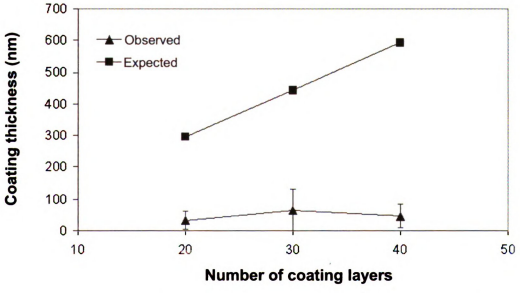

Figure 27. Comparison of the observed coating thickness to the expected coating thickness for 20, 30 and 40 coating layers. The expected coating thickness assumes a close-packed arrangement of the Mn_2O_3 nanoparticles.

The observations of the manganese oxide coated cross sections of the porous membranes are consistent with the observations of other coatings on porous substrates [162, 163]. The manganese oxide coatings were cohesive with the underlying membranes. Cai et al. [162] made similar observations of a cross section of a ZnO film on a porous silicon substrate which revealed that the film was closely connected to the substrate, likely due to the partial filling of the coating particles into the surface pores. Shaoqiang et al. [163] also made similar observations of hydroxyapatite growth into the porous silicon substrate during sintering to produce a well bonded coating on the substrate.

4.4 CONCLUSIONS

Coating a ceramic water filtration membrane with these nanoparticles using a layer-by-layer process, followed by sintering, yields an α-Mn_2O_3 surface layer as well as evidence that the Mn is present in the interior of the membrane.

The AFM and SEM data showed that with increasing number of coating layers, the roughness remains unchanged, the grain size increased and the feature height decreased. The increase in grain size with increased number of coating layers indicates that grain growth occurs as the thickness of the coating on the surface of the membrane increases due to agglomeration of the coating material

with additional coating layers, since there was no significant change in the grain size due to sintering.

Since the as prepared MnO_2 particles are too large to diffuse into the fine pores on the filtration surface of the membranes, Mn ions that remain in the MnO_2 coating suspension disperse into the pore network by capillary action during coating. The Mn present within the pores then diffuses into the grains of the membrane during sintering, as is indicated by the EDS mapping and line scans of cross sectioned samples. Since Mn is present throughout the membrane as well as on the surface, this would likely serve to improve the long-term performance of the membrane, since the catalyst will still be present even if the surface layer has eroded as well as allowing small molecular weight compound contaminants to be oxidized as they pass through the membrane.

Although there is not a direct linear relationship between the number of layers applied and the resulting coating thickness, the trend is that the coating thickness does increase with increasing application of coating layers.

CHAPTER 5

HYBRID OZONATION-MEMBRANE FILTRATION

5.1 INTRODUCTION

The use of a hybrid ozonation-membrane filtration system has been shown to improve the water flux recovery as compared to convention membrane filtration without ozonation [2, 3, 63, 65, 71]. Ozone decomposition, resulting in OH radical formation, results in the decomposition of organic foulants on the surface of the membrane, allowing for improved flux through the membrane [65, 66].

Degradation of organic matter by manganese oxide catalysts with ozone has been studied by others [6-44]. Naydenov and Mehandjiev used MnO_2 to catalytically oxidize benzene by ozone [6]. They achieved complete oxidation of benzene by ozone on MnO_2 catalysts in a temperature range of 10-80°C (283-353 K). Einaga et al. [18-24] also studied the effects of catalyst support, reaction

conditions and manganese loading on the ability of manganese oxide to catalyze the oxidation of benzene in gas phase reactions. Einaga et al. determined that alumina-supported manganese oxides catalyze the oxidation of benzene to CO_2 and CO by ozone at room temperature although the rate of oxidation is independent of the Mn loading (between 5-20 wt%) [18, 20, 24]. The alumina-supported manganese oxide catalyst was the only catalyst to show a steady-state activity for cyclohexane decomposition, compared to Ag, Fe, Co, Cu and Ni catalysts on alumina supports at room temperature [19].

Einaga et at. also determined that the addition of water vapor to reaction gases suppressed the deactivation of the Al_2O_3-supported [21] and SiO_2-supported [23] manganese oxide catalyst. The water vapor increased the oxidation of the organic byproducts, such as formic acid, to CO_2.

Andreozzi et al. demonstrated the catalytic ability of MnO_2 for the ozonation of pyruvic acid [9, 11], oxalic acid [8] and metol [10]. They found that pyruvic acid did not react with either MnO_2 or O_3, however, significant oxidation was observed when ozone was used in combination with MnO_2 [9, 11]. Andreozzi et al. found that oxalic acid reacted only slightly with MnO_2 in the absence of ozone, however, the reactivity was greatly increased with the addition of ozone [8]. Although these experiments were done in a semibatch process with suspended

MnO_2 particles, rather than on a coated membrane, the catalytic properties of the MnO_2 in the presence of ozone seem quite promising.

Lee et al. examined the catalytic ozonation of humic acids [12]. Humic acid was used as a model organic compound because it is a major constituent of natural organic matter. The authors observed a significant decrease in UV absorption with MnO_2 combined with ozone, indicating the oxidation of the humic acids [12].

Ma and Graham [13, 14] showed that manganese oxide catalysts enhanced the oxidation of atrazine by promoting ozone decomposition and hydroxyl radical formation. Ma and Graham's work also demonstrated that humic substances have a positive effect on the oxidation of atrazine as compared to that observed with the manganese catalyst and ozone alone [13, 14].

Manganese-containing catalysts have also been shown to be effective for the decomposition of organic compounds in gas phase reactions [25, 30-32, 34-40, 43, 44]. Delagrange et al. [32] have shown that when non-thermal plasma techniques are used to oxidize volatile organic compounds (VOCs), the formation of CO, CO_2 and O_3 was observed. With the addition of manganese oxide based catalysts, the ozone that is generated in the plasma reactor decomposes the VOCs and eliminates the ozone [32].

The catalytic oxidation of VOCs allows for the reduction in the reaction temperature [36-38]. This reduction in the reaction temperature allows for air pollution control in industrial applications without the need for heating and cooling large volumes of air [32]. The lower reaction temperature also allows the manganese catalysts to be effective for the decomposition of VOCs during engine warm-up, in automotive applications [38].

MnO_2 can therefore be an effective catalyst for the ozonation of organic matter. The favorable catalytic properties of manganese dioxide suggest that experimentation with a MnO_2 coating on the ceramic filtration membranes for the use in combined ozonation-filtration is logical.

This chapter will describe the effect of the membrane coatings on the water flux and the quality of the water (using TOC measurements) treated by the hybrid ozonation-membrane filtration system. The optimum choice of the MnO_2 preparation method, the number of coating layers, the sintering conditions and the surface reactions that act to lower the concentrations of water contaminants will be studied.

5.2 MATERIALS AND METHODS

Manganese oxide colloids were prepared by ozonation and by mixing of $KMnO_4$ and PAH using the methods described in Chapter 3. These colloids were used to coat ceramic water filtration membranes, as described in Chapter 4 and were sintered in air at either 500°C for 45 minutes or 550°C for 30 minutes.

The membranes were used in a hybrid ozonation-membrane filtration system [63], operated in total recycling (permeate and retentate) mode. Figure 28 shows a schematic representation of the hybrid ozonation-membrane filtration system. The membrane module is equipped with a stainless-steel housing (TAMI North America, St. Laurent, QC, Canada). The permeate was recycled using a pump (Masterflex, Cole-Parmer Inc., Vernon Hills, IL) into the feed tank at 15 min intervals. The transmembrane pressure and crossflow velocity were controlled using a recirculation pump (Gear Pump Drive, Micropump, Cole-Parmer Inc., Vernon Hills, IL) and a back pressure regulator (Swagelok, Solon, OH). The temperature of the water was maintained at 22.5 ± 0.5°C. The temperature, crossflow rate and pressure were monitored in the recirculation line using a multifunctional sensor (L Series, Alicat Scientific, Tucson, AZ) and recorded using a Lab View data acquisition system (National Instruments, Austin, TX). The permeate mass was measured at 60 second intervals using an electronic balance (Adventurer Pro Analytical Balance, Ohaus Corporation, Pine Brook, NJ).

Pure oxygen from a compressed gas cylinder was passed through a moisture trap containing anhydrous calcium sulfate (Drierite, Xenia, OH) into a high-pressure ozone generator (Atlas Series, Absolute Ozone Generator, Absolute System Inc., Edmonton, AB, Canada) and injected directly into the pressurized system. The input ozone pressure (20 – 30 kPa greater than the transmembrane pressure) was monitored using a pressure gauge (Ashcroft Inc., Stratford, CT). The ozone gas flow rate was regulated using a mass flow controller (Model GFC 17, Aalborg, Orangeburg, NY) which was installed between the ozone generator and the membrane module. The ozone concentration in the gas phase was measured by an ozone gas monitor (Model 450H, Teledyne Instruments, City of Industry, CA) and the dissolved ozone concentration in the retentate and recirulation loop was continuously monitored using an amperometric ozone microsensor (AMT Analysenmesstechnik GmbH, Rostock, Germany) and recorded using a LabView data acquisition system.

TOC was measured using an OI Analytical model 1010 analyzer (OI Analytical, College Station, TX) using the UV/persulfate method [169] as a surrogate parameter to estimate the potential for disinfection by-product (DBP) formation during chlorination [170-172]. Suwannee River NOM (International Humic Substances Society, St. Paul, MN) was used. This material was isolated from the Suwannee River using reverse osmosis. The NOM solutions were prepared in deionized water at a concentration of 9.9 ± 0.4 mg C/L (pH 8.0).

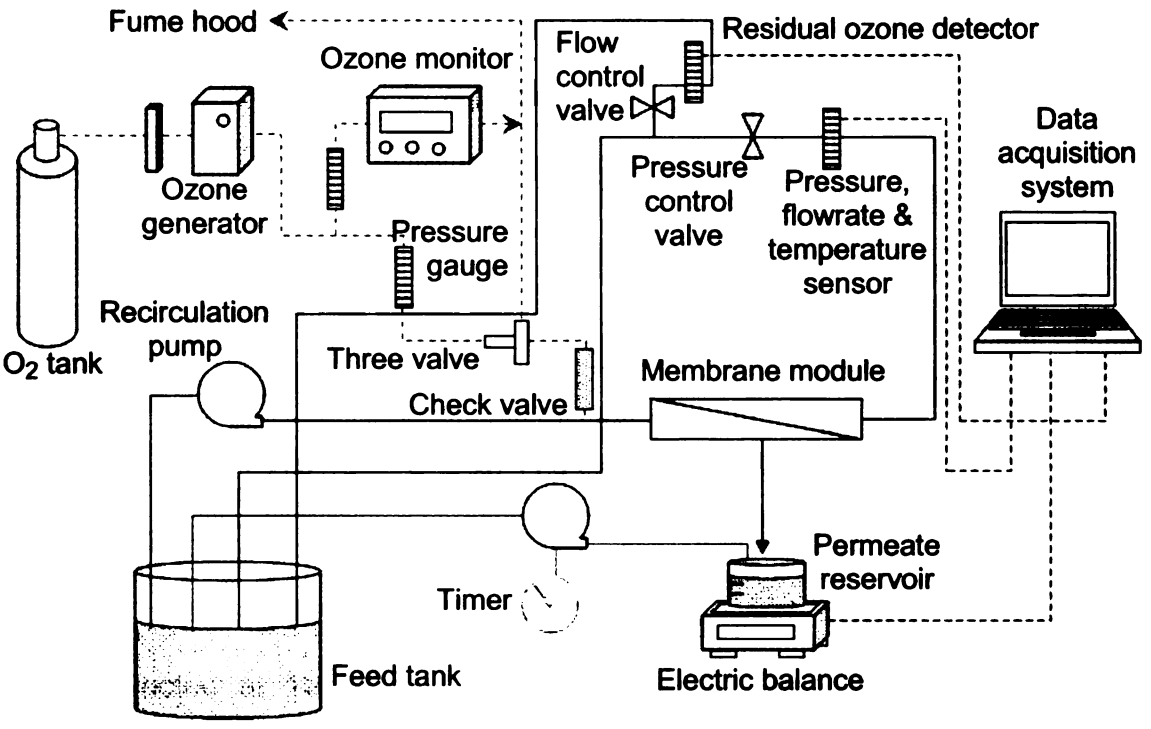

Figure 28. Schematic representation of the hybrid ozonation-membrane filtation system.

Water samples from Lake Lansing (Haslett, MI), a borderline eutrophic lake with a dissolved organic carbon (DOC) of ~11 mg C/L were treated in the hybrid ozonation-membrane filtration system [63] (O_3 gas flow rate: $1x10^{-5}$ m^3/min, crossflow velocity: 0.47 m/s, transmembrane pressure: 200-228 kPa, initial flux: 104-115 $L/m^2 \cdot hr$, temperature: 22.5 ± 0.5°C). The flux through the membrane was measured and normalized with respect to the initial Lake Lansing water permeability.

One-way ANOVA testing, with Tukey's mean comparison tests ($p \leq 0.05$) (Minitab statistical software, Minitab Inc.), was used to determine if differences in measurements are statistically significant.

5.3 RESULTS AND DISCUSSION

5.3.1 TOTAL ORGANIC CARBON (TOC) REMOVAL

Samples of the permeate (the water that has passed through the membrane) were collected at 10, 40, 80, 120, 140 and 160 minutes of operation and analyzed for total organic carbon (TOC). The average TOC was reported in milligrams of carbon per liter of water (Figure 29) [173]. The effect of the membrane sintering temperature on the average TOC in permeate samples from the hybrid ozonation-membrane filtration system was compared. For the membranes coated with 20 layers of manganese oxide prepared using the ozonation method, the average TOC in the permeate for the membrane sintered at 500°C (5-20-500 Ozone) was 5.7 ± 0.9 mg C/L, while for the membrane sintered at 550°C (5-20-550 Ozone) it was 6.8 ± 0.9 mg C/L. Since the average TOC in the permeate collected using the membrane sintered at 500°C (5-20-500 Ozone) was lower than for the membrane sintered at 550°C (5-20-550 Ozone), although not statistically significant, the 500°C sintering temperature was used for the membrane that was coated with 30 layers of the manganese oxide

prepared by ozonation (5-30-500 Ozone). The average TOC in the permeate samples for the 5-30-500 Ozone membrane was 4.4 ± 0.7 mg C/L.

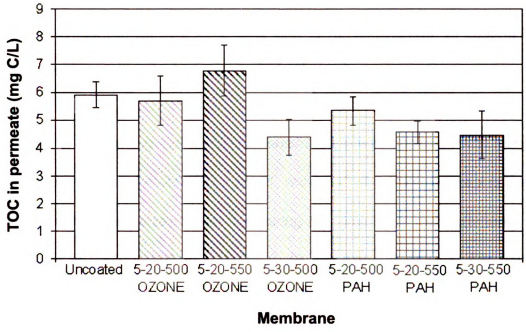

Figure 29. Total organic carbon present in permeate samples after combined ozonation and catalytic membrane filtration. Initial feed water TOC: 9.9 ± 0.4 mg C/L, temperature: 22.5 ± 0.5°C, transmembrane pressure: 138 kPa.

For the membranes coated with 20 layers of the MnO_2 prepared by mixing of $KMnO_4$ and PAH, the average TOC in the permeate for the membrane sintered at 500°C (5-20-500 PAH) was 5.4 ± 0.5 mg C/L, while for the membrane sintered at 550°C (5-20-550 PAH) it was 4.6 ± 0.4 mg C/L. Since the average TOC in the permeate collected using the membrane sintered at 550°C (5-20-550 PAH) was lower than for the membrane sintered at 500°C (5-20-500 PAH), although not statistically significant, the 550°C sintering temperature was used for the

membrane that was coated with 30 layers of the MnO_2 prepared by mixing of $KMnO_4$ and PAH (5-30-550 PAH). The average TOC in the permeate samples for the 5-30-550 PAH membrane was 4.5 ± 0.9 mg C/L. This trend of decreasing organic content in permeate samples with increasing number of coating layers was also seen in the work of Karnik et al. [3].

A trend of decreasing average TOC concentration was observed with increasing average grain size ($y=-2.0852x + 85.71$, with an r^2 of 0.4424, where x is the TOC and y is the grain size), when comparing the grain size measurements made using SEM micrographs in Chapter 4, to the average TOC in the permeate samples. The largest average grain size for the catalytic coating of 79 nm (5-30-500 PAH) resulted in only 4.5 mg C/L in the permeate sample, while the smallest average grain size of 71 nm (5-0-0) resulted in 5.9 mg C/L in the permeate sample, as shown in Figure 30.

Comparing the two different coating methods, treatment with the membrane that was coated with 30 layers of the manganese oxide prepared by ozonation resulted in a lower average TOC concentration in the permeate samples (although not statistically significant) than that observed with the membrane coated with the manganese oxide prepared by mixing of $KMnO_4$ and PAH (4.4 ± 0.7 mg C/L vs. 4.5 ± 0.9 mg C/L, respectively). The flux recovery was measured using an uncoated membrane as well as membranes coated with 20, 30 and 40

layers of the manganese oxide prepared by ozonation and sintered in air at 500°C for 45 minutes.

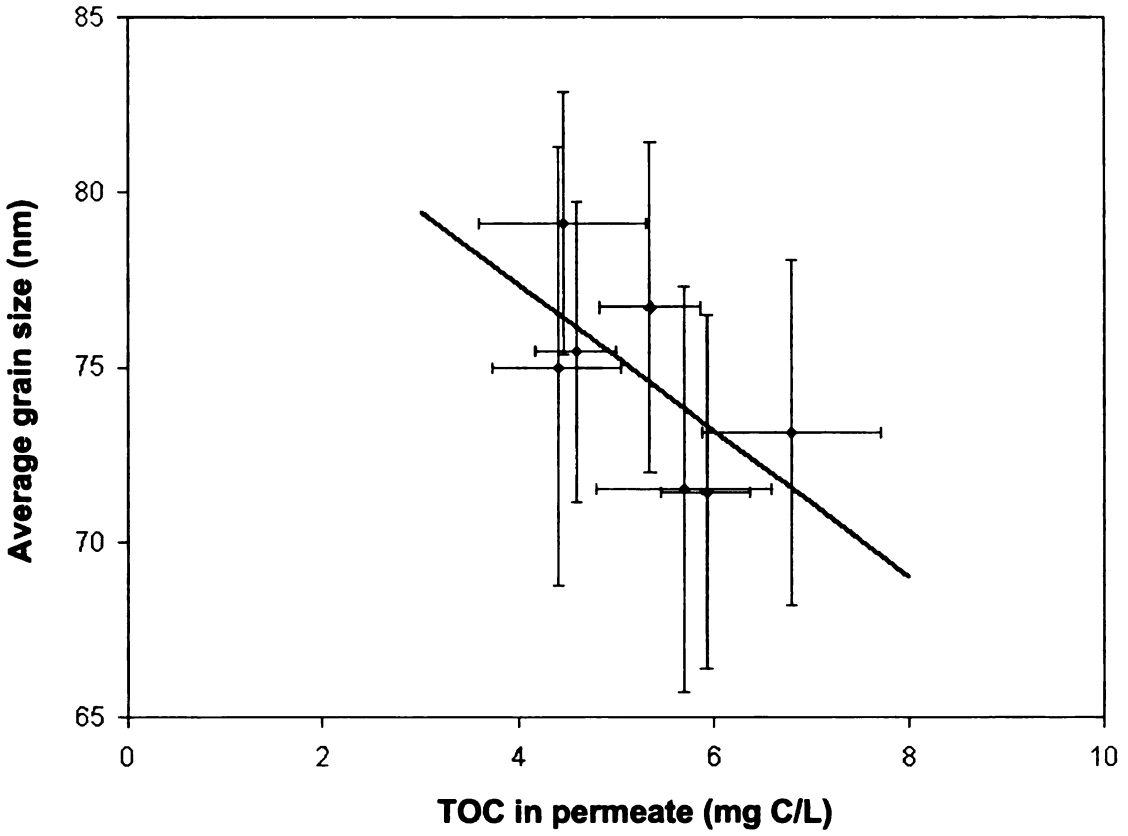

Figure 30. Comparison of grain size to the amount of total organic carbon present in permeate samples after combined ozonation and catalytic membrane filtration. Initial feed water TOC: 9.9 ± 0.4 mg C/L, temperature: 22.5 ± 0.5°C, transmembrane pressure: 138 kPa.

The decrease in the TOC in the permeate water samples indicate that the manganese oxide coating does in fact act as a catalyst for the oxidation of organic matter [174, 175] when used in a hybrid ozonation-membrane filtration system.

5.3.2 FLUX RECOVERY

Since the deposition of organic foulants on the membrane surface results in a decrease in the water flux through the membrane, the performance of the system can be evaluated using water flux measurements [173], as shown in Figure 31. When the uncoated membrane was used in the hybrid ozonation-membrane filtration system, the flux decreased steadily during the first hour to approximately 60% of the clean water flux with no recovery over the remaining 6.5 hours of measurements. When the coated membranes were used in the hybrid system, there was also an initial decrease in the flux during the first hour due to fouling of the membrane but then there was a steady recovery of the flux. The membrane coated with 20 layers achieved approximately a 95% recovery after 5.5 hours, while the membrane coated with 30 layers achieved approximately a 90% recovery after 7.5 hours and the membrane coated with 40 layers achieved approximately an 85% recovery after 7.5 hours. This recovery of the permeate flux due to the oxidation of the organic foulants by ozone was also observed by Karnik et al. [65].

The improved flux recovery for the coated membranes, as compared to the uncoated membrane, is the result of the catalytic activity of the coating for the oxidation of the organic matter by ozone [3, 63, 65, 174]. This demonstrates the ability of the manganese oxide coated membrane to catalyze the degradation of foulants at the membrane surface when used in combination with ozonation.

Increasing the number of coating layers, however, does not result in an improvement in the flux recovery.

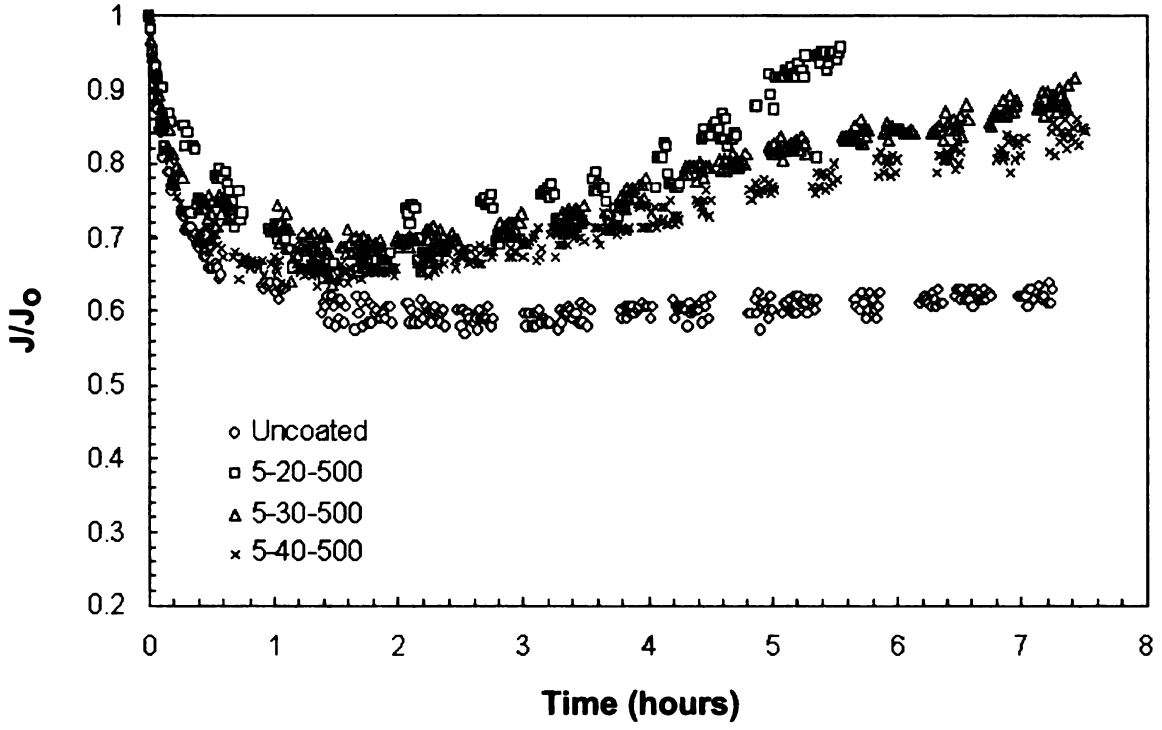

Figure 31. Normalized flux for an uncoated membrane as well as membranes coated with 20, 30 and 40 layers of the manganese oxide prepared using ozonation. O_3 gas flow rate: $1x10^{-5}$ m^3/min, crossflow velocity: 0.47 m/s, transmembrane pressure: 200-228 kPa, initial flux: 104-115 L/m^2·hr, temperature: 22.5 ± 0.5°C.

5.4 CONCLUSIONS

Surface modification of ceramic water filtration membranes, by coating with manganese oxide and sintering, has been shown to reduce the average TOC in the permeate when the membranes are used in a combined ozonation and membrane filtration system. Increasing the number of coating layers resulted in a

decrease in the TOC concentration in permeate samples. The optimum coating material and sintering condition, in terms of TOC removal, was manganese oxide prepared using ozonation that was sintered at 500°C for 45 minutes. This decrease of organic content in permeate samples with increasing number of manganese oxide coating layers on a ceramic membrane used in a hybrid ozonation-membrane filtration system was also seen in the work of Karnik et al. [3] with Fe_2O_3 coated ceramic membranes.

The application of the manganese oxide coating results in improved water flux through the membrane, when compared to an uncoated membrane in a combined ozonation and membrane filtration system. Reed et al. [37] have shown that increasing the loading of manganese oxide on a silica-supported catalyst from 3% to 10% gave higher reaction rates for both acetone oxidation and ozone decomposition in gas phase reactions. In our studies of manganese oxide coatings on ceramic water filtration membranes, increasing the amount of manganese oxide, by increasing the number of coating layers, did not show an increase in the oxidation of the foulants that result in the decreased water flux through the membrane. The membrane coated with 20 layers shows improved flux recovery over the uncoated membrane and the membranes coated with 30 or 40 layers.

Although the hydrated MnO_2 was reduced to α-Mn_2O_3 during the sintering process, the decrease in TOC demonstrates that α-Mn_2O_3 is an effective catalyst

for the oxidation of organic matter by ozone in aqueous solutions. In gas phase reactions Radwan et al. [82] determined that the amount of Mn_2O_3 (between 5 to 20 wt.%) added to a cordierite support increased the catalytic activity towards CO oxidation by O_2 as well as H_2O_2 decomposition. In our studies of the manganese oxide coating on the ceramic water filtration membranes, the amount of Mn_2O_3 catalyst was adjusted by changing the number of coating layers applied to the membrane. Increasing the amount of manganese oxide on the surface of the membrane did improve the TOC removal from permeate water samples.

Fouling of water filtration membranes is a result of the adsorption and deposition of organic substances on the surface of the membrane, which results in a decrease in the water flux through the membrane [115]. You et al. [54] determined that ozone reduces fouling of membranes by destroying aromatic rings and forming linear chains, thereby changing the chemical structure and characteristics of the filtration cake. This change in the characteristics of the filtration cake allows the water flowing across the membranes to flush away loose fragments, which decreases the fouling of the membrane [54]. The increase in the flux recovery with the use of the manganese oxide coated membranes in our study demonstrate that α-Mn_2O_3 is an effective catalyst for the catalytic oxidation of organic matter by ozone. Mn_2O_3 has been shown to be an effective catalyst for gas phase reactions [81-83]. The water flux improvement and the reduction of TOC in permeate samples in this work indicates that Mn_2O_3 is also an effective

catalyst for the degradation of organic compounds in aqueous systems [2, 3, 63, 65, 174].

CHAPTER 6

THERMAL STABILITY OF CERAMIC MEMBRANES

6.1 INTRODUCTION

Ceramic membranes have been used for purification of gases [176-180] as well as water [2-4, 61-74]. In gas-phase applications, the ceramic membranes may be exposed to elevated temperatures [176-178], requiring high thermal stability of the membranes. In the high temperature gas-phase applications, silica membranes [178] or membranes that are silicon based [176] or palladium based [177] have been used. Where titania membranes have been used for high temperature applications, they have been coated with an alumina separation layer [181].

Ceramic membranes have also been studied for use in hybrid ozonation-membrane filtration systems due to their resistance to ozone [2-4, 61-71]. When

preparing catalytic membranes, the coating material is applied then the membrane is sintered or calcined at elevated temperatures to ensure adherence of the coating to the underlying membrane [3, 4, 182, 183]. As ceramic membranes become more widely used, there is a growing concern about the effect of sintering temperature on the underlying membrane structure [95, 96].

When ceramic membranes are coated with materials that necessitate high temperature treatment, the morphology and microstructure of the underlying membrane may be altered during the sintering of the coating. This may in turn result in changes to the underlying membrane properties such as the pore size and structure.

During sintering, the grains can either grow with very little densification or there can be an increase in the density, to approximately 95% of theoretical density, followed by grain growth [97]. Alternatively, grain growth and densification can occur simultaneously [97]. The driving force for the increase in grain size is the reduction in the surface energy. By increasing the average grain size, there is a reduction in the total surface area, resulting in a reduction in the surface energy [97].

When the iron oxide coating was applied to alumina-zirconia-titania (AZT) ceramic membranes in the work of Karnik et al., the membranes were sintered in air at 900°C [3, 4]. However, because of its significantly lower melting point, the

manganese oxide coated titania membranes are sintered at 500-550°C, also in air. As the AZT membranes used in the work of Karnik et al. are no longer available for purchase, during the course of experimentation, the titania membranes were coated with the nano-Fe_2O_3 coating and sintered in air at 900°C. The deionized (DI) water permeability of these membranes increased from 360 $L/m^2 \cdot hr \cdot MPa$ (uncoated and unsintered) to 10250 $L/m^2 \cdot hr \cdot MPa$ after coating with 40 layers of the Fe_2O_3 nanoparticles and sintering at in air 900°C (unpublished results). When these membranes were coated with 40 layers of manganese oxide nanoparticles and sintered in air at 500°C, the permeability of the membranes was only 650 $L/m^2 \cdot hr \cdot MPa$.

Ahmad et al. [181] have also seen this increase in the permeability of titania membranes when they were coated with an alumina separation layer and sintered. Although the alumina separation layer allows for high temperature gas separation, the titania membrane support undergoes pore coarsening when the alumina is sintered to the titania support [181]. In the preparation of a titania membrane with a titania support, Wang et al. [184] saw an increase in the mean pore size distribution with increased sintering temperature and a concomitant increase in the pure water permeability.

Kim et al. [185] used a hydrothermal process to improve the thermal stability of titania membranes. In this hydrothermal process, a titania sol was autoclave aged at 135°C for 12 hours before being used to prepare unsupported titania

membranes. The hydrothermal process retarded the anatase-to-rutile phase transformation when the membranes were calcined at 600°C. However, the pore size of the membranes prepared using the hydrothermal process shifted to a larger pore size after calcination at 600°C due to crystallite growth [185].

During the grain growth process, pores located at the grain boundaries can move with the grain boundaries and coalesce into larger pores at the intersections of the grains [97, 98]. During sintering of ceramics, the velocity of an inclusion, such as a pore, υ_p, can be related to the pore mobility, B_p, and the driving force, F_p, according to equation (4) [98]:

$$\upsilon_p = B_p F_p \qquad (4)$$

When the pore is dragged by the grain boundary, the velocities of the pore and boundary are identical, however, unhindered, the grain boundary mobility, B_b, is much greater than the pore mobility ($B_b \gg B_p$). Therefore, at some point when the boundary moves beyond the pore, the pore becomes unpinned, resulting in an isolated pore. This makes further densification increasingly difficult since pore diffusion through the bulk is much slower than along the grain boundaries. The resulting grain boundary velocity, υ_b, is controlled by the driving force on the boundary, F_b, along with the pore mobility and the number of pores per grain boundary, p, according to equation (5) [98]:

$$\upsilon_b = \frac{B_p F_b}{p} \qquad (5)$$

In fine grained oxides, an increase in pore size is observed in the initial stages of sintering. As sintering time continues, however, there is a marked increase in grain size [97, 98].

Since the nanoparticle coated membranes examined in this study are sintered for relatively short periods of time, the underlying membrane support only experiences the early stages of sintering and is not able to completely eliminate the agglomerated pores or further densify. An increase in the pore diameter of porous ceramic membranes with increasing sintering temperature (when sintered for short periods of time) has previously been observed by Baticle et al. [99].

The addition of zirconia (up to 20 mol%) to titania membranes by Sekulić et al. [186] resulted in a smaller pore sizes when the membranes were calcined at 450°C. It is believe that this is a result of the supression of the anantase-to-rutile phase transition by the zirconia forming clusters between anatase particles. These clusters prevent the contact of the anatase particles, suppressing the phase transformation to rutile [186]. Bae et al [187] also demonstrated that the addition of Fe_2O_3, CeO_2 and Pt dopants to titania membranes decreased the average pore size of sintered membranes.

Different ceramic membranes, although possessing the same molecular weight cut-off (MWCO), because of differences in membrane composition, will have greater or less thermal stability. The focus of this chapter, therefore, is to link the

application of high temperature coatings and/or high temperature sintering to changes in the membrane performance.

6.2 MATERIALS AND METHODS

Two commercial titania membranes (INSIDE CéRAM, TAMI North America, St. Laurent, Québec, Canada) having a 7-channel, tubular design, MWCO of 5 kDa with an outside diameter of 1 cm and length of 25 cm were each cut into three equal pieces. The permeability of the six sections of membrane was measured using DI water with a flow rate of 0.8 L/min and transmembrane pressure of 103 kPa.

After testing their initial permeability, one sample was left unsintered and the other five membrane samples were sintered (in air) at either 500°C, 600°C, 700°C, 800°C or 900°C by placing the sample in the furnace and increasing the temperature at a rate of approximately 10°C/min to the desired sintering temperature, holding that temperature for 30 minutes and then turning the furnace off and allowing the samples to cool to room temperature in the furnace over the next 8 hours.

Manganese oxide nanoparticles were prepared by ozonation using the method described in Chapter 3. This nanoparticle colloid was used to coat ceramic water

filtration membranes, as described in Chapter 4. Membranes were coated with 20 layers then sintered (in air) either using the same ramped heating and cooling profile as for the uncoated samples (with sintering temperatures of 350°C, 400°C and 450°C for 45 minutes), or else the furnace was heated to the desired sintering temperature, the samples were placed in the furnace and sintered for 30 minutes (at 350°C, 450°C and 500°C) and then they were removed from the furnace to cool to room temperature.

XRD samples of the unsintered membrane were prepared by cutting a 5 mm section from the membrane using a diamond-wafering saw then further cutting this section to expose the inner filtration surface of the membrane. The pieces were then adhered to a glass slide using a double-sided adhesive tab so that an area of approximately 1 cm^2 of the filtration surface of the membrane was exposed.

Another section of the unsintered membrane was also cut from the membrane and it was ground into a powder with a mortar and pestle for XRD testing.

To compare to the AZT ceramic membrane that had been used in the work of Karnik et al., an unsintered section of the AZT ceramic membrane was also prepared in the same manner as described above to obtain XRD samples of the filtration surface as well as the powdered membrane.

XRD spectra were obtained using a Rigaku Rotaflex RU-200B XRD (Tokyo, Japan, 45KV/100mA, copper radiation).

To study the morphological changes that occur in the titania membranes during sintering at the different temperatures, SEM samples were prepared by cutting an approximately 3 mm thick cross section from each sample using a diamond-wafering saw. An arc of approximately 3 mm was cut from this cross section and was adhered to an aluminum stub using carbon paste cement. Since the ceramic samples are non-conductive, they were coated with osmium for SEM observation. The conductive Os coating is completely amorphous, precisely follows the contours of the specimen surface and shows no granularity, even when viewed at high magnification.

SEM analysis was performed using a JEOL JSM-7500F SEM (Japan Electron Optics Laboratories, Tokyo, Japan) at an accelerating voltage of 15 kV and magnification of 75,000x. The average grain size for each sample was determined by taking six micrographs from each sample and measuring an average of at least 100 grains per micrograph using the mean linear intercept method (ASTM Standard E 112-96 (2004)). To determine if differences were statistically significant, all measurements were analyzed using one-way ANOVA testing, with Tukey's mean comparison tests ($p \leq 0.05$, Minitab statistical software, Minitab Inc.).

To study the topographical changes of the sintered titania membrane samples, AFM samples were prepared in a similar manner to that used for SEM analysis. Samples were adhered to a 12 mm diameter steel disc using double-sided adhesive tabs, so that the filtration surface was pointing upward.

A Nanoscope III Multimode Atomic Force Microscope (Digital Instruments Inc.), operating in contact mode, was used for AFM imaging. The probe was a triangular silicon nitride (Si_3N_4) NP probe (Veeco Instruments, CA, nominal cantilever spring constant: 0.12 N/m, nominal frequency: 20 kHz, tip height: 2.5 μm to 3.5 μm, nominal radius: 20 nm, side angle: 35°). Each sample had five different areas, of dimension 5 μm x 5 μm, scanned at a rate of 1.0 Hz to determine the average roughness of each sample. To determine if differences were statistically significant, all measurements were analyzed using one-way ANOVA testing, with Tukey's mean comparison tests ($p \leq 0.05$, Minitab statistical software, Minitab Inc.).

The MWCO was determined by measuring the rejection of 1, 5, 25, 50 and 80 kDa dextrans (Sigma-Aldrich Co., St. Louis, MO) by the ceramic membranes. The MWCO is the lowest molecular weight that has a rejection of greater than 80% by the membrane [188, 189].

Titania membranes with a nominal MWCO of 5 kDa were coated with 10, 20, 30 and 40 layers of manganese oxide and sintered in air at 500°C for 45 min. One

uncoated membrane was also sintered in air at 500°C for 45 min and one membrane was left uncoated and unsintered. Dextran feed solutions were prepared using 1, 5, 25, 50 and 80 kDa dextran molecules (Sigma-Aldrich Co., St. Louis, MO), at a concentration of 10 mg/L [173]. The dextran solutions were filtered using 25 cm long ceramic membranes in a stainless-steel housing (TAMI North America, St. Laurent, QC, Canada). Tests were conducted with DI water using a crossflow velocity of 0.47 m/s and transmembrane pressure of 172-207 kPa (transmembrane pressure adjusted to give an initial permeate flux of 110 ± 5 L/m^2hr) at a temperature of 25 ± 0.5°C. Approximately 35 mL of permeate was collected and the total organic carbon (TOC) content was measured using a OI Analytical model 1010 analyzer with a 1051 auto-sampler (O.I. Corporation, College Station, TX). Only one sample was collected for each molecular weight dextran sample and membrane combination, therefore, the statistical differences between samples were not determined.

6.3 RESULTS AND DISCUSSION

6.3.1 X-RAY DIFFRACTION (XRD) ANALYSIS

Figure 32a-d shows the intensity vs. 2θ for the filtration surface of the titania membrane, the ground titania membrane, the filtration surface of the AZT membrane and the ground AZT membrane, where θ is the angle between the

incident x-ray beam and the scattering planes, used to determine the atomic plane spacing, d, according to Bragg's law, equation (6):

$$n\lambda=2d \sin \theta \qquad (6)$$

where λ is the x-ray wavelength. Indexing of the XRD spectra of the filtration surface (Figure 32a) and the powdered (Figure 32b) titania membrane demonstrates that the titania is present as the rutile phase. The differences in the intensities of the indexed planes between the two samples indicates that there is a preferred orientation of the (110) and (211) planes on the filtration surface. Although rutile is a stable phase of TiO_2 [190, 191], the rutile phase exhibits rapid grain growth around 800°C [191]. The Zr that was observed from the EDS mapping of the titania and AZT membranes, however, was not observed in the XRD spectra. This is due to the penetration of the x-ray beam into the XRD sample, such that the small amounts of Zr present on the filtration surface were not able to be detected. Adding ZrO_2 to TiO_2 has the effect of inhibiting the phase transformation of the TiO_2 from anatase to rutile due to the substitution of Zr^{4+} ions for Ti^{4+} ions, causing an increase in the strain energy which lowers the driving force for the phase transformation [98, 186]. While the manufacturer will not disclose the rationale or the chemistry of the surface layers of either the AZT or the titania membrane, the Zr may have been added to the filtration surface to promote the adsorption of viruses on the membrane [192].

Indexing of the XRD spectra of the filtration surface (Figure 32c) and the powdered (Figure 32d) AZT membrane shows additional titania peaks for the

filtration surface, indicating that the filtration surface is composed of titania with an alumina-zirconia-titania membrane support, as was described in the work of Karnik et al. [68]. The presence of the alumina and zirconia with the titania in the AZT membranes improves the high temperature stability [193, 194]. The melting temperature of titania is 1840-1870°C [193, 194], while the melting temperatures of alumina and zirconia are 2030-2050°C [181, 193] and 2700°C [193], respectively. Since diffusion occurs at approximately half of the melting temperature [195], sintering the titania membrane at 900°C facilitates grain growth due to diffusion. With the essentially pure titania membrane, we saw extensive grain growth upon sintering. However, in the membrane containing the higher temperature Al_2O_3 and ZrO_2 phases, as expected, less grain growth was observed.

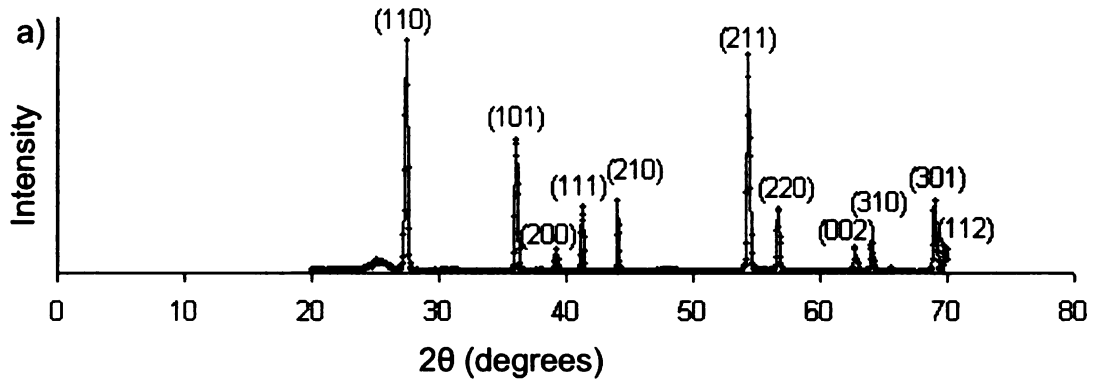

Figure 32. XRD spectra of a) the filtration surface of the titania membrane, indexed as the rutile phase, b) powdered titania membrane, indexed as the rutile phase, c) filtration surface of the AZT membrane, where the indexed pattern shows the alumina (A), zirconia (Z) and titania (T) peaks and d) powdered AZT membrane, where the indexed pattern shows the alumina (A), zirconia (Z) and titania (T) peaks.

Figure 32. Continued

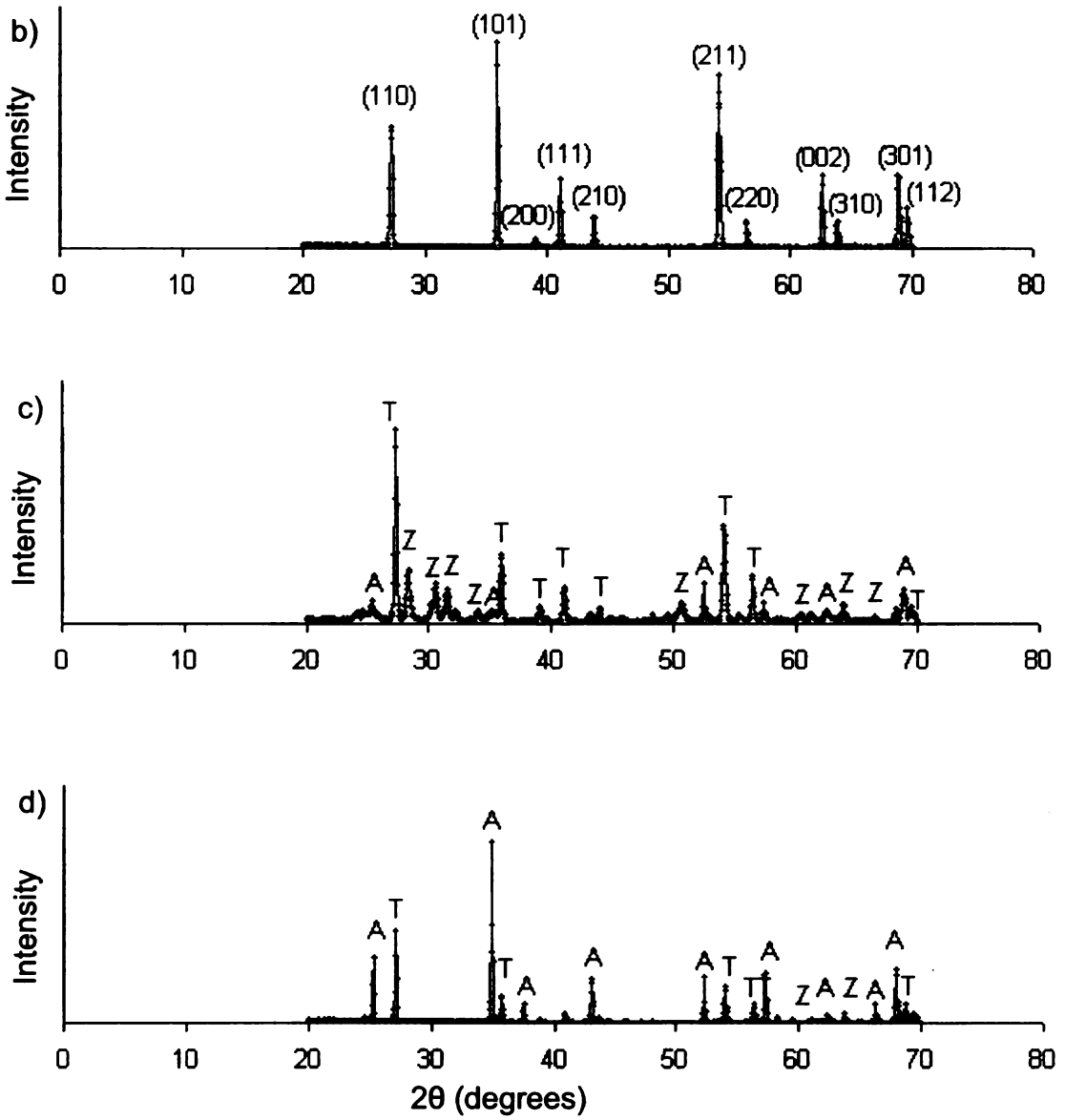

6.3.2 DEIONIZED WATER PERMEABILITY

The deionized (DI) water permeability of the six sections cut from the two uncoated and unsintered titania membranes is shown in Table 2.

Table 2: DI water permeability of unsintered membrane sections (flow rate: 0.8 L/min, transmembrane pressure: 103 kPa).

	Membrane section					
	1	2	3	4	5	6
Permeability ($L/m^2 \cdot hr \cdot MPa$)	53	91	180	131	61	94
Standard Deviation ($L/m^2 \cdot hr \cdot MPa$)	1	2	5	5	1	2

Since membrane section 3 had higher permeabilities than the others, presumably due to discrepancies in the membrane manufacturing, that piece was left unsintered. For comparison, the remaining pieces of membrane that were the closest in permeabilities were then sintered as follows: section 1 at 500°C, section 2 at 600°C, section 4 at 700°C, section 5 at 800°C and section 6 at 900°C. All samples were sintered in air. The samples were placed in the furnace and the ramped heating profile (approximately 10°C /min) was used and the samples were sintered for 30 minutes, once the desired sintering temperature was achieved. The samples were then allowed to cool in the furnace (to room temperature) over 8 hours.

After sintering, the clean water permeability of the membrane samples was once again tested and the results are shown in Table 3.

Although there is large variability in the permeabilities of the uncoated membranes, there is an order of magnitude increase in the permeability from the unsintered membrane to the membrane sintered at 500°C. There is a steady

increase in the permeability of the membranes as the sintering temperature is increased. Since the ends of the membrane sections were resealed prior to the second set of permeability tests, there were some small changes in the sealing area. Even small changes in the sealing area can have a large effect on the effective area of membrane filtration since the membrane lengths used in these tests is so small [173]. This change in the effective area resulted in the large increase in the standard deviation between the first set of tests and the second set of tests.

Table 3: DI water permeability of sintered membrane sections (flow rate: 0.8 L/min, transmembrane pressure: 103 kPa).

	Membrane Section					
	1	2	3	4	5	6
Sintering Condition	500°C	600°C	unsintered	700°C	800°C	900°C
Permeability ($L/m^2 \cdot hr \cdot MPa$)	1830	4150	152	5070	9600	11300
Standard Deviation (between experiments) ($L/m^2 \cdot hr \cdot MPa$)	203	216	22	365	299	424

6.3.3 SINTERED MEMBRANE ANALYSIS

6.3.3.1 SCANNING ELECTRON MICROSCOPY (SEM) ANALYSIS

Since such large changes in permeabilities were observed, the microstructure of the sintered and unsintered membranes were compared by SEM analysis. SEM

micrographs of the filtration surface of the titania membrane samples (Figure 33a-f) for membranes sintered at 500°C (33b), 600°C (33c) and 700°C (33d) show little increase in grain size, while the grain size of the membrane sintered at 800°C (33e) appears slightly larger, with a large increase in grain size for the membrane sintered at 900°C (Figure 33f). However, grain size measurements demonstrate that the unsintered sample has spherical grains with an average grain size of 38.0 ± 1.2 nm (statistically significant difference from all other measurements at 95% confidence interval), which increases to 47.2 ± 3.3 nm for the sample sintered at 500°C, to 47.7 ± 3.8 nm for the sample sintered at 600°C and to 48.1 ± 3.8 nm for the sample sintered at 700°C (no statistically significant difference between the samples sintered at 500°C, 600°C and 700°C at 95% confidence interval). The membrane section sintered at 800°C shows some increase in irregularity in the shape of the grains (Figure 33e) and has an average grain size of 56.3 ± 4.8 nm (statistically significant difference from all other measurements at 95% confidence interval). The sample sintered at 900°C has very large, irregular grains (Figure 33f) and has an average grain size of 90.5 ± 13.0 nm (statistically significant difference from all other measurements at 95% confidence interval). This increase in grain size beginning at 800°C is well known and has been described by others [190, 191]. The large increase in grain size is also accompanied by an increase in pore size, as can be seen by the large pores between the grains in the sample sintered at 900°C (Figure 33f).

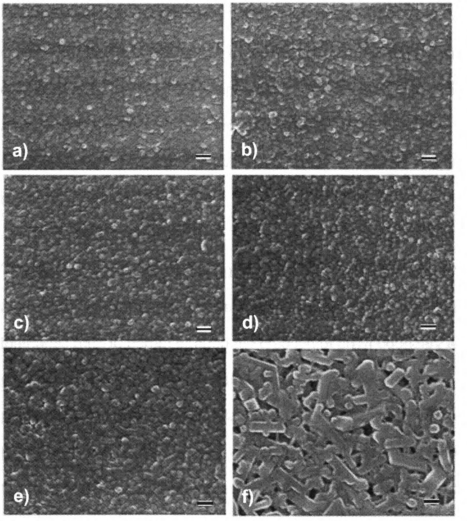

Figure 33. SEM micrographs of the titania membrane a) unsintered, b) sintered at 500°C for 30 min, c) sintered at 600°C for 30 min, d) sintered at 700°C for 30 min, e) sintered at 800°C for 30 min and f) sintered at 900°C for 30 min. All scale bars are 100 nm.

At elevated temperatures (approximately half of the melting temperature and above), the atoms that comprise the grains of the ceramic material have sufficient energy for diffusion to occur [195]. The melting temperature for TiO_2 is 1840-1870°C [193, 194], therefore, atomic diffusion would be expected when the titania membrane is sintered at 900°C, the sintering temperature used for the

Fe_2O_3 coating on the AZT membranes. In contrast, when the AZT membrane was sintered by Karnik et al. [3, 4], this significant increase in grain size was not observed since the melting temperatures for alumina (2030-2050°C) [181, 193] and zirconia (2700°C) [193] are significantly higher than that of titania. This results in higher thermal stability of the AZT membrane than the titania membrane.

The driving force during sintering is the reduction of surface energy. This can be achieved by coarsening of the particles or by the reduction of solid/vapor interfaces (due to pores) through the creation of grain boundary area, followed by grain growth, resulting in densification [97]. The increase in the membrane permeability after sintering indicates that densification has not occurred, rather, the pores have coarsened during sintering. During sintering, the grains on the filtration surface of the membrane are believed to follow the pure coarsening trajectory shown in the plot of grain size versus percent of theoretical density in Figure 34. Following this trajectory, large grains are formed as well as large pores. The mechanisms that lead to coarsening are evaporation-condensation, surface diffusion and lattice diffusion from the surface to the neck area between grains. These mechanisms do not lead to densification because they do not allow the particle centers to move closer together. As the grain boundaries migrate, the pores between grains can move along the grain boundary and coarsen as well [97]. For densification to occur, the mechanisms involved are volume diffusion from the grain boundary area to the neck area or grain boundary diffusion from

the grain boundary area to the neck area. This allows the particle centers to move closer together [97] and follows the densification followed by grain growth trajectory shown in Figure 34.

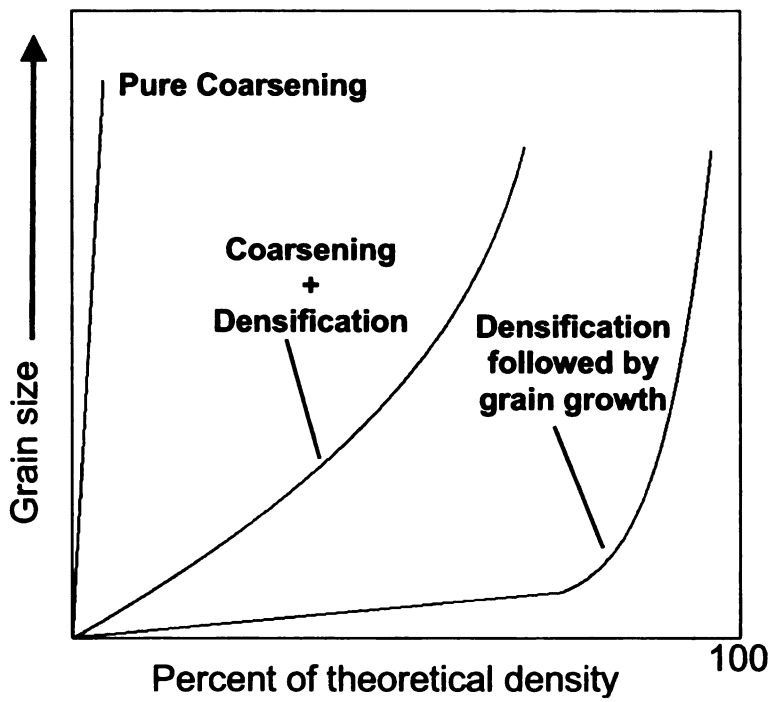

Figure 34. Grain size versus percent of theoretical density for pure coarsening, coarsening and densification and densification followed by grain growth (Adapted from Figure 10.5a in [97]).

Measurement of the SEM micrographs of the sintered membrane surfaces along with the permeability data indicates that grain and pore coarsening has occurred, rather than densification. Therefore, the prevailing sintering mechanisms are surface diffusion rather than bulk diffusion.

A graph of the increase in grain size with increased sintering temperature can be seen in Figure 35. The DI water permeability of the sintered and unsintered

membranes is also shown in Figure 35. Both the grain size and the DI water permeability show a steady increase as the sintering temperature increases. This increased permeability is due to an increase in the pores on the filtration surface of the membrane at the elevated sintering temperatures [72]. Even with the small change in the grain size, and the accompanying coarsening of the pores, there are large changes in the DI water permeability of the membranes. Since the molecular weight of water is so small (18 Da), even slight changes in the pore size have a pronounced effect on the permeability of the membranes.

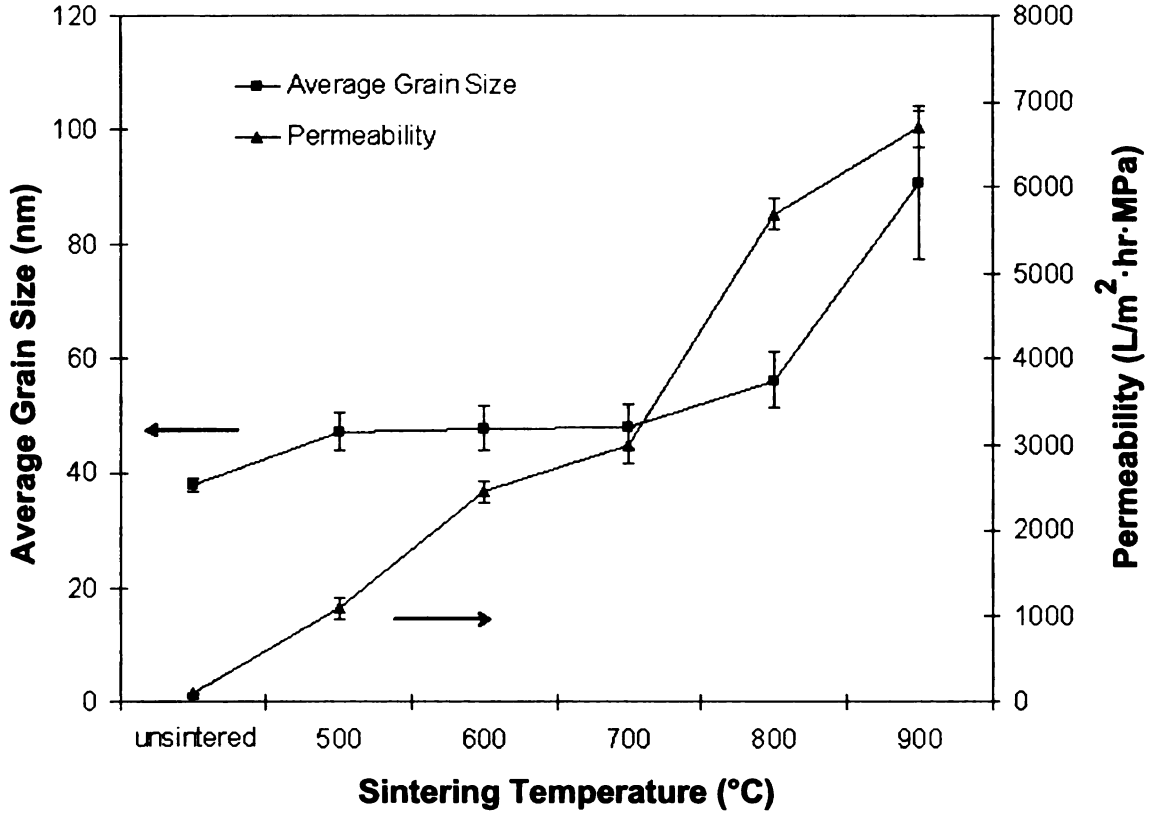

Figure 35. Comparison of the average grain size and permeability for the unsintered and sintered membranes. The average and standard deviation for the grain size measurements were determined by measurement at least 600 grains using the intercept method (ASTM Standard E 112-96 (2004)). The average and standard deviation of the permeability measurements were determined by testing each membrane at least 4 times until steady state conditions were achieved (permeability test conditions: flow rate: 0.8 L/min, transmembrane pressure: 103 kPa).

6.3.3.2 ATOMIC FORCE MICROSCOPY (AFM) ANALYSIS

AFM analysis of the average roughness (R_a) (shown in Figure 36), which is the arithmetic average of the absolute values of the surface height deviations as measured from the mean plane, shows no statistically significant difference (at 95% confidence interval) in the average roughness values for the unsintered sample (30.2 ± 4.8 nm) and the samples sintered in air at 500°C (24.6 ± 8.9 nm), 600°C (30.8 ± 6.3 nm), 700°C (34.4 ± 11.2 nm) or 800°C (32.4 ± 4.4 nm). However, there is a statistically significant difference between the sample sintered in air at 900°C (64.5 ± 26.6 nm) and all other samples. Comparing the grain size changes to the average roughness, the larger grains on the surface of the titania membrane sintered at 900°C correspond to the increased roughness of the filtration surface. As would be expected with the large increase in grain size, and the accompanying coarsening of the pores, this results in an increased roughness of the filtration surface. This increase in the roughness with an increase in the grain size for nanoparticle grains was observed by Dias et al. [196].

This significant increase in roughness, when the membrane was sintered at 900°C, was not seen by Karnik et al. in their work with the AZT membranes [4]. The improved thermal stability of the AZT membranes did not result in the topographical changes that the titania membranes underwent, when sintered at 900°C.

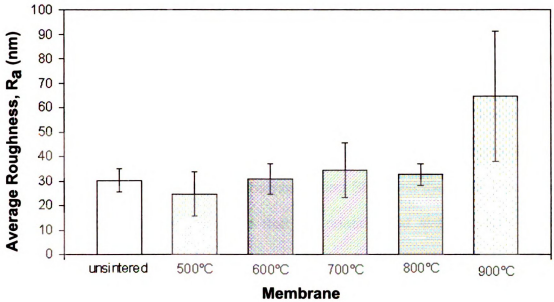

Figure 36. AFM average roughness (R_a) for the unsintered and sintered membranes.

6.3.4 COATED MEMBRANE ANALYSIS

To study the effect of coating the membranes and sintering temperature, six additional membrane sections were prepared. To study the effect of lowering the sintering temperature, three membrane sections were coated with 20 layers of the manganese oxide coating and then sintered in air at 350°C, 400°C and 450°C for 45 min using the same heating and cooling profile that was used for the uncoated samples. To investigate whether the grain growth can be decreased by decreasing the time that the membranes are at the elevated temperatures, three membrane sections were coated with 20 layers of the manganese oxide coating and then sintered in air at 350°C, 450°C and 500°C for

30 minutes. Rather than using the previously described heating and cooling profile, the furnace was heated to the sintering temperature, the samples were inserted, sintered for 30 minutes and then removed from the furnace to cool to room temperature. The maximum sintering temperature used with this stepped sintering profile was 500°C since higher temperatures would cause thermal shock. These samples were then analyzed using SEM and the grain sizes were measured. To determine the effect that the coating and sintering has on the MWCO of the membranes, the rejection of 1 kDa, 5 kDa, 25 kDa, 50 kDa and 80 kDa dextran was measured.

6.3.4.1 SCANNING ELECTRON MICROSCOPY (SEM) ANALYSIS

SEM micrographs of the coated and sintered samples (Figure 37) do not appear to show any changes in the grain size of the coated membrane surface. However, grain size measurements of the samples sintered at 400°C (41.0 ± 2.7 nm) and 450°C (43.5 ± 3.1 nm) using the ramped heating and cooling method demonstrate a statistically significant difference from the unsintered sample (38.0 ± 1.2 nm). The grain size of the samples sintered at 450°C (41.9 ± 3.0 nm) and 500°C (43.5 ± 2.7 nm) without the ramped heating and cooling profile also demonstrate a statistically significant difference from the unsintered sample. There is no statistical difference in grain size between the samples sintered at

350°C with the ramped (39.3 ± 2.3 nm) or without the ramped (39.6 ± 3.4 nm) heating and cooling method and the unsintered sample.

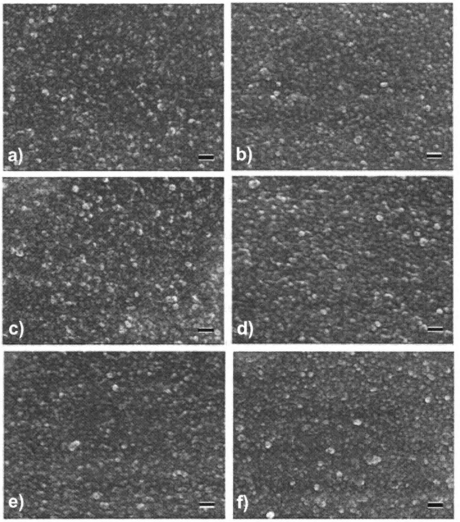

Figure 37. SEM micrographs of the titania membrane coated with 20 layers of the manganese oxide coating and sintered at a) 350°C for 45 min, b) sintered at 400°C for 45 min and c) sintered at 450°C for 45 min, each with a ramped heating/cooling profile, as well as d) sintered at 350°C for 30 min, e) sintered at 450°C for 30 min and f) sintered at 500°C for 30 min without a ramped heating/cooling profile. All scale bars are 100 nm.

Grain size measurements indicate that it is possible to sinter the manganese oxide coating onto the titania membrane without coarsening the grains by using a sintering temperature of 350°C (with or without a ramped heating and cooling profile).

Using the ramped heating and cooling profile and calculating the resulting diffusivity, using equation (2) (approximating using a transition metal in an oxide host, D_o = 1.8 x 10^{-9} m^2/s and Q = 202 x 10^3 J/mol for Ni in MgO [167]) the diffusivity can be plotted with respect to time for the ramped profile (Figure 38). Although the sample experiences elevated temperatures for a longer period of time when sintered using the ramped heating and cooling profile, the diffusivity increases and decreases very rapidly during the heat up and cool down periods, respectively. Therefore, very little diffusion occurs outside of the hold time for the sintering process. This is why changing from a ramped to a stepped heating and cooling profile did not limit the amount of grain growth experienced during sintering. Lowering the sintering temperature, however, reduced the grain growth, since the diffusivity is function of the sintering temperature, as shown by equation (2).

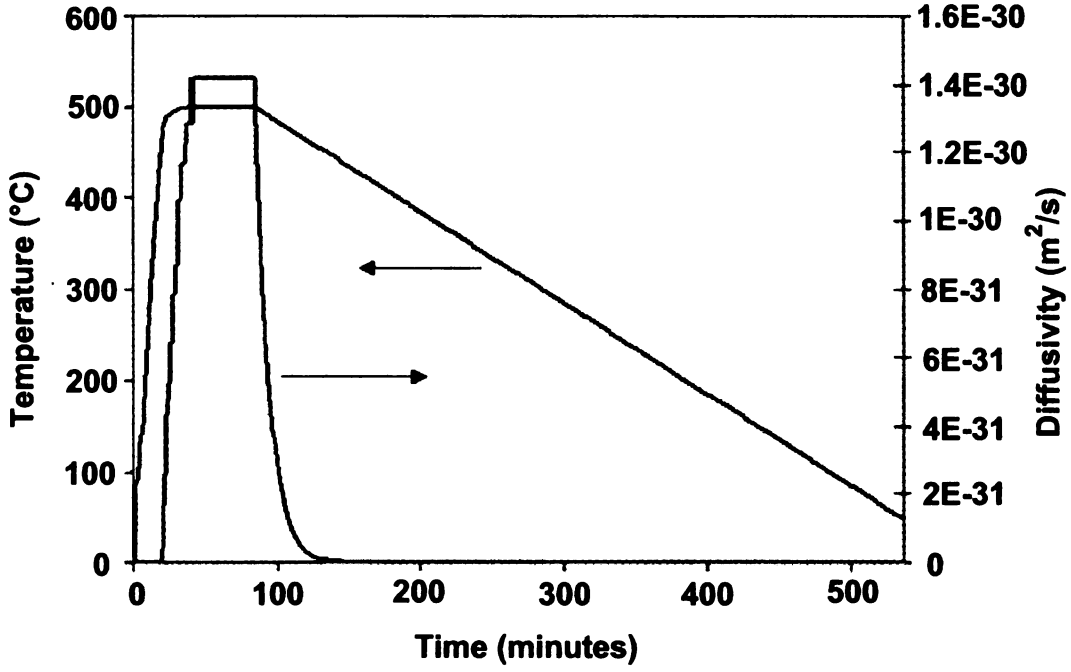

Figure 38. A plot of the temperature versus time and diffusivity versus time for the ramped heating and cooling profile.

Comparing the permeability of the coated membranes to the grain size, a trend of increasing permeability with increasing grain size is observed (Figure 39). This is consistent with the results of the uncoated membranes. This correlation between the grain size and permeability has been observed by others [197, 198] and is due to the coalescence of the pores during sintering [97]. At the low sintering temperatures and short times used for the manganese oxide coated titania membranes, the nanoparticle coating is able to sinter to the underlying membrane because of the enhanced reactivity of nanoparticles [199, 200], while for the supporting membrane, the larger particles are only able to undergo the initial stages of sintering: grain growth and pore coarsening [98].

As would be expected, the grain sizes of the coated samples sintered between 350°C-500°C, either with or without the ramped heating and cooling profile (grain sizes range between 39.3 ± 2.3 nm and 43.5 ± 3.1 nm), are within the range of the grain sizes observed for the uncoated and unsintered sample (38.0 ± 1.2 nm) and the uncoated sample that was sintered at 500°C (47.2 ± 3.3 nm). Since there was no statistically significant difference (at 95% confidence interval) in the AFM roughness measurements between the unsintered sample and the uncoated samples sintered up to 800°C, the roughness of the coated samples that were sintered at or below 500°C was not measured, since no statistically significant difference would be expected.

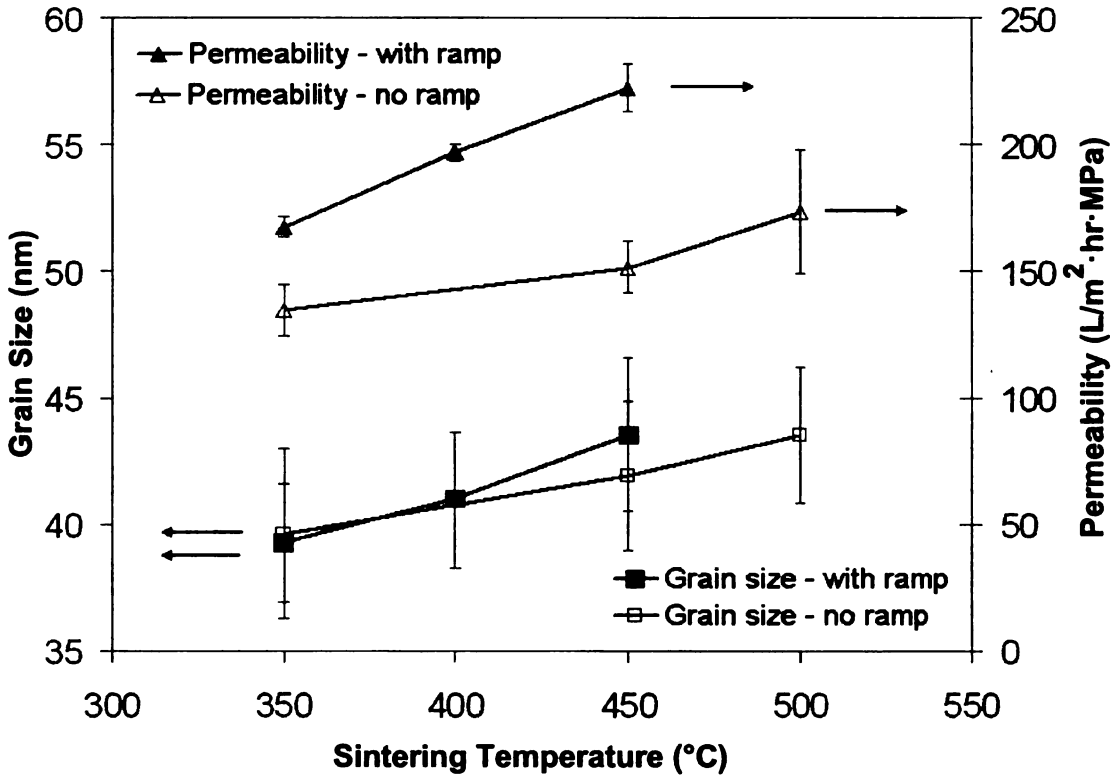

Figure 39. Comparison of the average grain size and permeability for the membrane samples coated with 20 layers of manganese oxide and sintered with and without a ramped heating and cooling profile.

6.3.4.2 MOLECULAR WEIGHT CUT-OFF (MWCO) MEASUREMENTS

Since an increase in the permeability of the membranes was observed at the 500°C sintering temperature that is used with the manganese oxide coating, the effect of the increased permeability on the MWCO of the membranes was studied. The rejection of 1 kDa, 5 kDa, 25 kDa, 50 kDa and 80 kDa dextran was measured using an uncoated and unsintered membrane, an uncoated membrane that was sintered at 500°C, and membranes that were coated with 10, 20, 30 and 40 layers of manganese oxide and sintered in air at 500°C (Figure 40).

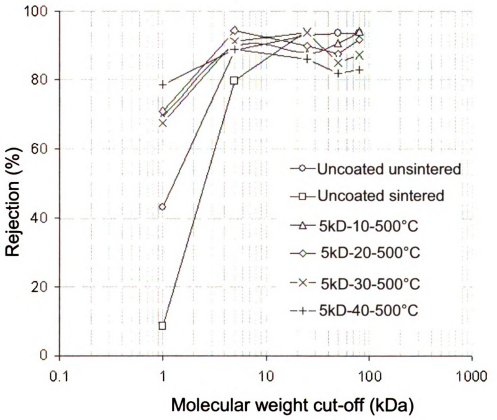

Figure 40. Percent rejection of 1 kDa, 5 kDa, 25 kDa, 50 kDa and 80 kDa dextran for titania, 7-channel, 5 kDa membranes that are uncoated and unsintered, uncoated and sintered at 500°C and coated with 10, 20, 30 and 40 layers of manganese oxide and sintered in air at 500°C.

The uncoated membrane that was sintered in air at 500°C has lower rejection of the 1 kDa and 5 kDa dextran (8.4% and 79.7%, respectively) than the uncoated and unsintered membrane (43.0% and 88.5%, respectively). However, the membranes that were coated with the manganese oxide coating all have higher rejection of the 1 kDa dextran (69.5%, 71.1%, 67.5% and 78.7% for the 10, 20, 30 and 40 coating layers, respectively) than the uncoated and unsintered membrane. The 5 kDa dextran rejection for the coated and sintered membranes (89.6%, 94.5%, 91.2% and 88.7% for the 10, 20, 30 and 40 coating layers, respectively) was also equal to or higher than the uncoated and unsintered membrane (88.5%). The 25 kDa dextran rejection for the membranes coated with 10, 20 and 40 layers of the manganese oxide and sintered at 500°C (87.8%, 89.9% and 86.1%, respectively) was slightly lower than the uncoated and unsintered membrane (93.1%), however, the membrane coated with 30 layers had a 93.8% rejection of the 25 kDa dextran. With the 50 kDa dextran, the rejection for the coated membranes were all lower (90.6%, 87.5%, 85.0% and 81.9% for the 10, 20, 30 and 40 coating layers, respectively) than the uncoated and unsintered membrane (93.5%). The 80 kDa dextran rejection was slightly lower than the uncoated and unsintered membrane (93.6%) for the membranes coated with 20, 30 and 40 coating layers (91.7%, 87.3% and 82.9%, respectively), however, the membrane coated with 10 coating layers had a rejection of 94.2% for the 80 kDa dextran.

Sintering of the uncoated membrane resulted in an increase in the permeability of the membrane. The rejection of 1 kDa and 5 kDa dextrans also decreased when the uncoated membrane was sintered. However, the addition of the manganese oxide coating resulted in an increase in the 1 kDa and 5 kDa dextran rejection. Since the permeability was tested using DI water, which has a molecular weight of 18 Da, the increase in pore size due to sintering resulted in an increase in its permeability. However, the dextrans having molecular weights of 1 kDa and 5 kDa are rejected at percentages >69.5% with the coated and sintered membranes (the nominal MWCO of the membranes, as received from the supplier, is 5 kDa).

The increase in the MWCO with sintering has been observed by Schaep et al. [201]. However, the increase in permeability of the membranes while maintaining the molecular weight cut-off with the coated membranes is unique. Ma et al. [202] found that coating of Al_2O_3 membranes with a Si-doped TiO_2 resulted in a decrease in the MWCO of the membrane with a concomitant decrease in the permeability. However, the coatings on these membranes were calcined at 500°C and the alumina membrane has a higher thermal stability than the titania membrane [193].

6.5 CONCLUSIONS

The large increase in DI water permeability of the titania membranes is due to a pore coalescence in the filtration layer, marked by the increase in grain size of the filtration surface of this membrane during sintering. This significant coarsening was not seen with the AZT membranes since the alumina and zirconia in the AZT membrane have higher melting temperatures than the TiO_2. The lower melting temperature TiO_2 allows for increased diffusion at the Fe_2O_3/AZT sintering temperatures of 900°C. The large grains that result from sintering the titania membrane at 900°C also increase the surface roughness of the sintered membrane.

Characterization of the titania water filtration membranes indicates that it has lower thermal stability than the AZT membranes. This lower thermal stability results in an increase in permeability from 152 $L/m^2 \cdot hr \cdot MPa$ for the unsintered membrane to 11,300 $L/m^2 \cdot hr \cdot MPa$ for the membrane sintered at 900°C. Therefore, when a coating is applied to the titania membrane, it cannot be sintered at as high of temperatures as the AZT membrane. This is consistent with the work of Sekulić et al. [186] and Bae et al. [187], in which dopants had to be added to titania membranes in order to suppress the increase in pore size during high temperature treatments.

Since titania membranes have poor thermal stability above 500°C (due to the anatase to rutile phase transformation) [187], dopants can be used to retard the anatase to rutile transformation and any subsequent grain growth. The addition of ZrO_2 to TiO_2 has been shown to inhibit this transformation by substituting Ti^{4+} ions with Zr^{4+} ions, causing an increase in strain energy, which lowers the driving force for the phase transformation [98, 186]. Further, Zr has been shown by Wegmann et al. to have the added benefit of promoting virus adsorption onto the surface of the membranes [192].

Evaluation of the dextran rejection by the membranes coated with manganese oxide and sintered at 500°C shows that the nominal 5 kDa MWCO was maintained, while the permeability of the membranes actually increased (because of the effects of membrane sintering). This is of benefit because it allows for lower operating pressures, and hence a lower cost of operation, to maintain a constant flux through the membrane.

In the preparation of gas separation membranes, Ahmad et al. [181] determined that the addition of a sintered alumina coating on a titania membrane increased the selective permeability of the membrane. Alumina was used since it is stable up to its melting temperature of 2030-2050°C [181, 193]. Although an increase in pore size was observed as a result of the sintering (at 800°C and 1000°C) of the alumina to the base titania membrane, there was an improvement in the separation of gas mixtures containing H_2 and N_2. This improvement in

performance, despite the increase in pore size, is consistent with the results of the improvement in low MW dextran rejection by the manganese oxide coated titania membranes that were sintered at 500°C.

CHAPTER 7

SUMMARY AND CONCLUSIONS

7.1 SUMMARY AND CONCLUSIONS

The engineering significance of the work performed is that it has shown that it is possible to produce an effective catalytic manganese oxide coating on ceramic water filtration membranes for use in a hybrid ozonation-membrane filtration system. Although polymeric membranes are widely used for water purification due to their lower cost than ceramic membranes [57, 77-80], the longevity of ceramic membranes and their resistance to degradation by ozone allows ceramic membranes to be used in combination with ozonation [2-4, 57, 61-74].

A manganese oxide nanoparticle colloid for coating of the ceramic membranes was prepared by a novel method, the ozonation of Mn(II). This resulted in a colloidal suspension of hydrated MnO_2, with a flake-like morphology and average

particle size of ~92 nm. Physisorbed water is driven off the hydrated MnO_2 at approximately 80°C. Sintering of the hydrated MnO_2, at either 500°C for 45 minutes or 550°C for 30 minutes, both result in the reduction of the MnO_2 to α-Mn_2O_3. When the hydrated MnO_2 colloid is applied to a ceramic water filtration membrane and sintered, the resulting α-Mn_2O_3 coating acts as a catalyst for the oxidation of NOM at the surface of the membrane when used in combination with ozonation. The degradation of the NOM results in an improved water flux through the membrane as well as a decrease in the TOC concentration in permeate samples, when compared to uncoated ceramic membranes.

With increasing number of coating layers, the roughness of the coated membrane surface remains relatively unchanged, however the maximum feature height decreases, likely due to the filling of the valleys between the features with the MnO_2 nanoparticles. The grain size of the coated membrane surface increased with increasing number of coating layers, with a trend of decreasing TOC in permeate with an increase in the grain size. This is consistent with the observations of Kamik et al. [4], where no statistically significant change in roughness was observed with increasing number of Fe_2O_3 coating layers on AZT membranes, however, an increase in grain size was observed.

There was no change in the grain size of the filtration surface with the addition of 20 or 30 coating layers. There was, however, an increase in the grain size of the

filtration layer of the membrane that was coated with 40 layers of the manganese oxide and then sintered at 500°C. Since the sintering conditions remained the same for the different number of coating layers, the increase in grain size is likely due to the agglomeration of the manganese oxide colloid resulting in increased grain growth. Sintering of agglomerates results in the coarsening the grains, and subsequently the pores, of the filtration surface of the membranes.

EDS mapping showed Mn present throughout the coated and sintered membrane. Since solid state diffusion across the entire cross section of the membrane would not be possible at the sintering temperatures and times used, the Mn dispersed into the pores of the membrane during coating and then diffused into the grains of the membrane by solid state diffusion during sintering. The MnO_2 particles, however, are too large to fit into the pores of the filtration layer, therefore, Mn ions that were present in the colloid dispersed into the porous membrane by capillary action during coating. During the sintering process, the Mn ions diffuse into the grains of the membrane. The presence of the manganese within the membrane will be of benefit in the long term performance of the membranes since the catalytic performance will be maintained, even if there is wear at the surface of the membrane. Additionally, since the manganese is present within the pore structure of the membrane, small molecular weight compounds can be oxidized as they pass through the membranes.

TEM micrographs show that the manganese oxide produced a cohesive coating on the ceramic membrane substrate. This cohesion of nanoparticle coatings on porous substrates was observed by others [162, 163] and is likely due to the partial filling of the pores during the coating and sintering process. There was a trend of increasing thickness of the manganese oxide coating with increasing number of coating layers, however, the thicknesses varied considerably.

Increasing the number of coating layers improved the TOC removal by the membranes when used in the hybrid ozonation-membrane filtration system. The catalytic degradation of the organic foulants on the surface of the membrane was observed by improved water flux through the coated membranes. The water flux through the membranes recovered more fully and quickly with the membrane coated with only 20 layers, compared to the uncoated membrane and the membranes coated with 30 or 40 layers. No additional benefit is seen by increasing the number of coating layers beyond 20. Despite the reduction of the MnO_2 to α-Mn_2O_3 during sintering, the α-Mn_2O_3 is an effective catalyst for the degradation of organic matter in the water, as observed by the decreased TOC in the permeate and improved flux through the membranes.

The titania membranes used in these studies have lower thermal stability than alumina-zirconia-titania membranes. In the course of experimentation, the titania membranes were coated with Fe_2O_3 nanoparticles (since AZT membranes were no longer available for purchase) to compare to the results of Karnik et al. [3, 4,

66-68] (where Fe_2O_3 nanoparticle coatings were applied to AZT membranes and sintered at 900°C). However, when these membranes were sintered at 900°C, a large increase in the permeability was observed. The lower thermal stability of the titania membranes, as compared to the AZT membranes resulted in increasing grain size during sintering. This correlation between increased grain size and increased permeability was observed by others [197, 198] and is the result of the coalescence of pores during the sintering process [97].

Pore coarsening during grain growth causes increased DI water permeability. Although the coated membranes that are sintered at 500°C show an increase in permeability, they are still able to maintain a MWCO of 5 kDa. The increase in permeability of the membranes while maintaining the molecular weight cut-off with the coated membranes is unique and would allow for high water production without sacrificing the rejection by the membrane.

CHAPTER 8

RECOMMENDATIONS FOR FUTURE WORK

8.1 RECOMMENDATIONS FOR FUTURE WORK

Although a 500°C sintering temperature was chosen to prevent the reduction of the MnO_2 to Mn_2O_3, this reduction still occurred. However, the resulting α-Mn_2O_3 coating has been shown to be an effective catalyst for the degradation of NOM in the water samples when used in the hybrid ozonation-membrane filtration system. Since sintering the coated membranes at higher temperatures results in higher permeability of the membranes (without sacrificing the 5 kDa MWCO), future work could study the use of a higher sintering temperature for the manganese oxide coated membranes, since the reduction to α-Mn_2O_3 has already occurred. Using the 500°C sintering temperature is not required to avoid the reduction of the coating material.

If a higher sintering temperature is used, the manganese oxide coated membrane may be able to maintain the 5 kDa MWCO while having higher permeabilities. This would decrease the operating cost of the hybrid ozonation-membrane filtration system if lower pressures could be used. Studies would have to be completed to determine how high the permeability can be increased before the MWCO of the membrane is compromised. Also, since only one test of the dextran rejection was completed for each membrane, additional testing of the MWCO should be completed for coated and sintered membranes to determine the reproducibility of the results.

If the manganese oxide colloids has agglomerated before it is applied to the ceramic membrane, the agglomerates will sinter together into larger grains on the surface of the membrane [97]. These larger grains will grow at the expense of the smaller grains and will result in grain coarsening [97, 98, 165, 166]. Since it is believe that the manganese oxide colloid is agglomerating over time (resulting in the increase in the grain size of the coated surface for the membrane coated with 40 layers), a study should be completed to determine the extent of agglomeration over time. The manganese oxide colloid should be prepared and sonicated and then holey carbon coated TEM grids should be dipped into the suspension at evenly spaced time intervals over the a 24 hour time period. Then TEM micrographs of these samples could be used to measure the change in agglomerate size over time.

The streaming potential can be used to determine the surface charge on a membrane [155]. Changing the membrane's surface charge will affect the adsorption of foulants on the membrane surface [155]. Since the application of the manganese oxide coating will affect the surface charge of the membrane, the streaming potential of the coated membranes should be determined. The work completed has characterized the morphology of the coated membrane surface, however, the streaming potential of the coated membranes has not been studied.

SEM analysis of membranes that have been used in the filtration system did not show any microcracking of the filtration surface, even after the membranes were left in water for over ten months (images of these samples are shown in Appendix C). A comprehensive study of the long term performance of the membranes should be completed to look at the durability of the coated ceramic membranes. This study should include microscopy characterization of the coated membranes after they have been used in the hybrid system for extended periods of time.

Additionally, the long term performance of the coating should be studied to ensure that the catalytic properties are maintained after extended use. These studies should include the water quality measurements obtained from permeate samples after extended use of the membrane in the hybrid ozonation-membrane filtration system. Also, any changes in the permeability of the membranes should be monitored.

The manganese oxide coating has been shown to reduce the TOC in permeate samples. Additional work should be completed to study the reduction of disinfection by-product formation, as well as the ability to remove other contamintants in water such as pharmaceuticals, chemicals, bacteria and viruses.

Since AZT membranes are no longer available for purchase, the work completed with the manganese oxide coatings was performed using titania membranes. The lower thermal stability of the titania membranes limits the sintering temperatures, and hence the type of coating material that can be applied. Future work should include the production of the membrane so that the thermal properties can be tailored to the application, without relying on commercially available membranes. This would also allow for modifications, such as the addition of the catalytic coating layer to be made during the production of the membrane, rather than as a secondary process. Adding the manganese oxide during the initial fabrication of the membrane would not only decrease the production time for the catalytic membranes, but it would also allow for the manganese oxide to be combined within the support of the membrane in larger quantities than can disperse into the membrane during the coating process.

Flat ceramic membranes could be produced using membrane preparation methods such as the sol-gel process or slip casting, as described in Chapter 2.

The preparation of alumina membranes has been studied by others [203-206] and could be applied to this application. During the production of the membranes, the pore sizes can be tailored so that the desired MWCO can be obtained. In addition, AZT membranes could be prepared to have similar thermal properties as the AZT membranes used by Karnik et al. [2-4, 65-68].

APPENDIX A

REPRESENTATIVE FOURIER TRANSFORM DATA

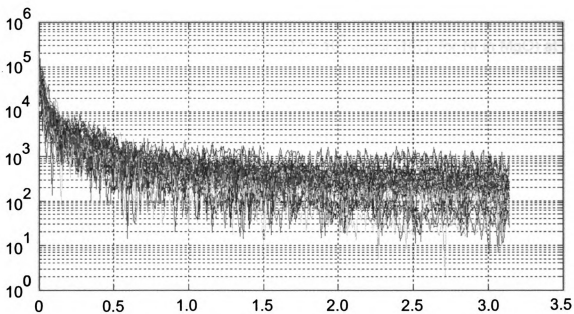

Figure A1. Representative Fourier transform analysis of 30 AFM line scans from a ceramic membrane coated with 20 layers of the manganese oxide coating prepared using ozone and sintered at 500°C for 45 minutes.

APPENDIX B

DIFFUSION CALCULATIONS

Calculations for the estimation of the diffusivity, D, using Equation (2) and the diffusion coefficient, Do, and the activation energy, Q, for a transition metal in an oxide host (Do = 1.8 x 10^{-9} m^2/s, Q = 202 x 10^3 J/mol [167], for Ni in MgO) at a temperature of 500°C (773 K):

$$D = D_0 \exp\left(\frac{-Q}{RT}\right)$$

D_0 = 1.8 x 10^{-9} m^2/s
Q = 202 kJ/mol
= 202 x 10^3 J/mol

R = 8.314 J/mol-K
T = 500°C
= 773 K

$$D = (1.8 \times 10^{-9} m^2/s) \exp\left(\frac{-202 \times 10^3 J/mol}{(8.314 J/mol \cdot K)(773 K)}\right)$$

D = 4.0 x 10^{-23} m^2/s

Calculations for the estimation of the diffusivity, D, using Equation (3), for diffusion across the entire membrane wall thickness (1 mm) for a sintering time of 45 minutes:

$$x \approx \sqrt{Dt}$$

$$x^2 \approx Dt$$

$$D \approx \frac{x^2}{t}$$

$t = 45\text{min}$
$= 2700\ \text{s}$

$x = 1\ \text{mm}$
$= 1 \times 10^{-3}\ \text{m}$

$$D \approx \frac{(1 \times 10^{-3}\text{m})^2}{2700\,\text{s}}$$

$$D \approx 3.7 \times 10^{-7}\ \text{m}^2/\text{s}$$

Calculations for the estimate of the diffusion distance using the diffusivity estimated for a transition metal in an oxide host, for a sintering time of 45 minutes:

$$x \approx \sqrt{4.0 \times 10^{-23}\text{m/s})(2700\text{s})}$$

$$x \approx 3.3 \times 10^{-10}\text{m}$$

$$x \approx 0.33\text{nm}$$

APPENDIX C

SCANNING ELECTRON MICROSCOPY (SEM) IMAGES OF MEMBRANES AFTER USE IN HYBRID SYSTEM

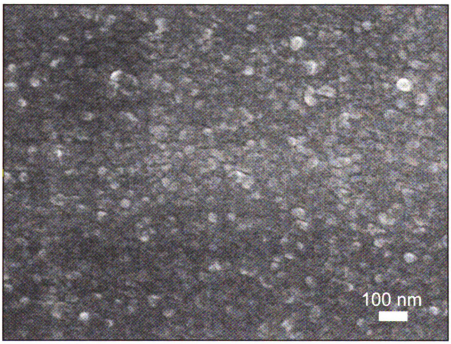

Figure C1. SEM micrograph of a titania membrane coated with 40 layers of manganese oxide prepared by ozonation (sintered in air at 500°C for 45 minutes) and used in the filtration system.

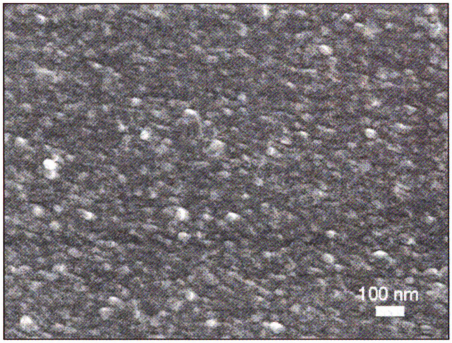

Figure C2. SEM micrograph of a titania membrane coated with 40 layers of manganese oxide prepared by ozonation (sintered in air at 500°C for 45 minutes), used in the filtration system and then soaked in water from 11/21/2008 to 09/30/2009.

REFERENCES

[1] Gracia, R., Aragües, J.L., Ovelleiro, J.L. Study of the catalytic ozonation of humic substances in water and their ozonation byproducts. Ozone Sci. Eng. 1996, 18, 195-208.

[2] Karnik, B.S., Davies, S.H., Baumann, M.J., Masten, S.J. The effects of combined ozonation and filtration on disinfection by-product formation. Water Res. 2005, 39, 2839-2850.

[3] Karnik, B.S., Davies, S.H., Baumann, M.J., Masten, S.J. Fabrication of catalytic membranes for the treatment of drinking water using combined ozonation and ultrafiltration. Environ. Sci. Technol., 2005, 39, 7656-7661.

[4] Karnik, B.S., Baumann, M.J., Masten, S.J., Davies, S.H. AFM and SEM characterization of iron oxide coated ceramic membranes. J. Mater. Sci, 2006, 41, 6861–6870.

[5] Spasova, I., Nikolov, P., Mehandjiev, D. Ozone decomposition over alumina-supported copper, manganese and copper-manganese catalysts. Ozone Sci. Eng., 2007, 29, 41-45.

[6] Naydenov, A., Mehandjiev, D. Complete oxidation of benzene on manganese dioxide by ozone. Appl. Catal. A: General, 1993, 97, 17-22.

[7] Mehandjiev, D., Naydenov, A., Ivanov, G. Ozone decomposition, benzene and CO oxidation over $NIMnO_3$-ilmenite and $NiMn_2O_4$-spinel catalysts. Appl. Catal. A, 2001, 206, 13-18.

[8] Andreozzi, R., Insola, A., Caprio, V., Marotta, R., Tufano, V. The use of manganese dioxide as a heterogeneous catalyst for oxalic acid ozonation in aqueous solution. Appl. Catal. A: General 1996, 138, 75-81.

[9] Andreozzi, R., Caprio, V., Insola, A., Marotta, R., Tufano, V. The ozonation of pyruvic acid in aqueous solutions catalyzed by suspended and dissolved manganese. Water Res. 1998, 32, 1492-1496.

[10] Andreozzi, R., Simona Lo Casale, M., Marotta, R., Pinto, G., Pollio, A. N-methyl-p-aminophenol (metol) ozonation in aqueous solutions: kinetics, mechanism and toxicological characterization of ozonized samples. Water Res. 2000, 34, 4419-4429.

[11] Andreozzi, R., Caprio, V., Marotta, R., Tufano, V. Kinetic modeling of pyruvic acid ozonation in aqueous solutions catalyzed by Mn(II) and Mn(IV) ions. Wat. Res. 2001, 35, 109-120.

[12] Lee, J.E., Jin, B.S., Cho, S.H., Han, S.H., Joo, O.S., Jung, K.D. Catalytic ozonation of humic acids with Fe/MgO. React. Kinet. Catal. Lett. 2005, 85, 65-71.

[13] Ma, J., Graham, N.J.D. Preliminary investigation of manganese-catalyzed ozonation for the destruction of atrazine. Ozone Sci. Eng., 1997, 19, 227-240.

[14] Ma, J., Graham, N.J.D. Degradation of atrazine by manganese-catalysed ozonation: influence of humic substances. Water Res., 1999, 33, 785-793.

[15] Ma, J., Graham, N.J.D. Degradation of atrazine by manganese-catalysed ozonation: influence of radical scavengers. Water Res., 2000, 34, 3822-3828.

[16] Ma, J., Sui, M.-H., Chen, Z.-L., Wang, L.-N. Degradation of refractory organic pollutants by catalytic ozonation-activated carbon and Mn-loaded activated carbon as catalysts. Ozone Sci. Eng., 2004, 26, 3-10.

[17] Futamura, S., Zhang, A.H., Einaga, H., Kabashima, H. Involvement of catalyst materials in nonthermal plasma chemical processing of hazardous air pollutants. Catal. Today, 2002, 72, 259-265.

[18] Einaga, H., Futurama, S. Catalytic oxidation of benzene with ozone over alumina-supported manganese oxides. J. Catal., 2004, 227, 304-312.

[19] Einaga, H., Futamura, S. Comparative study on the catalytic activities of alumina-supported metal oxides for oxidation of benzene and cyclohexane with ozone. React. Kinet. Catal. Lett., 2004, 81, 121-128.

[20] Einaga, H., Futamura, S. Oxidation behavior of cyclohexane on alumina-supported manganese oxides with ozone. Appl. Catal. B, 2005, 60, 49-55.

[21] Einaga, H., Futamura, S. Effect of water vapor on catalytic oxidation of benzene with ozone on alumina-supported manganese oxides. J. Catal., 2006, 243, 446-450.

[22] Einaga, H., Futamura, S. Catalytic oxidation of benzene with ozone over Mn ion-exchanged zeolites. Catal. Comm., 2007, 8, 557-560.

[23] Einaga, H., Ogata, A. Benzene oxidation with ozone over supported manganese oxide catalysts: Effects of catalyst support and reaction conditions. J. Hazard. Mater., 2009, 164, 1236-1241.

[24] Einaga, H., Harada, M., Ogata, A. Relationship between the structure of manganese oxides on alumina and catalytic activities for benzene oxidation with ozone. Catal. Lett., 2009, 129, 422-427.

[25] Wang, H.C., Chang, S.H., Hung, P.C., Hwang, J.F., Chang, M.B. Synergistic effect of transition metal oxides and ozone on PCDD/F destruction. J. Hazard. Mater., 2009, 164, 1452-1459.

[26] Yang, L., Hu, C., Nie, Y., Qu, J. Catalytic ozonation of selected pharmaceuticals over mesoporous alumina-supported manganese oxide. Environ. Sci. Technol., 2009, 43, 2525-2529.

[27] Martins, R.C., Quinta-Ferreira, R.M. Manganese-based catalysts for the catalytic remediation of phenolic acids by ozone. Ozone Sci. Eng., 2009, 31, 402-411.

[28] Xiao, H., Liu, R., Zhao, X., Qu, J. Enhanced degradation of 2,4-dinitrotoluene by ozonation in the presence of manganese(II) and oxalic acid. J. Mol. Catal. A., 2008, 286, 149-155.

[29] Xing, S.T., Hu, C., Qu, J.H., He, H., Yang, M. Characterization and reactivity of MnO_x supported on mesoporous zirconia for herbicide 2,4-D mineralization by ozone. Environ. Sci. Technol., 2008, 42, 3363-3368.

[30] Batakliev, T., Rakovsky, S., Zaikov, G.E. Investigation of metal oxide catalyst in ozone decomposition. Oxid. Comm., 2008, 31, 145-150.

[31] Tkachenko, S.N., Golozman, E.Z., Lunin, V.V., Kozlova, I.V., Egorova, G.V., Boevskaya, A.E., Tkachenko, I.S., Nechugovskii, A.I., Yaroshenko, M.P. A study of a catalyst based on oxides of base transition metals for decomposition of ozone and oxidation of toxic organic compounds. Rus. J. Appl. Chem., 2007, 80, 1353-1359.

[32] Delagrange, S., Pinard, L., Tatibouet, J.M. Combination of a non-thermal plasma and a catalyst for toluene removal from air: Manganese based oxide catalysts. Appl. Catal. B., 2006, 68, 92-98.

[33] Crisan, M., Raileanu, M., Preda, S., Zaharescu, M., Valean, A.M., Popovici, E.J., Teodorescu, V.S., Matajec, V., Mrazek, J. Manganese doped sol-gel materials with catalytic properties. J. Optoelect. Adv. Mater., 2006, 8, 815-819.

[34] Oyama, S.T., Li, W., Zhang, W.M. A comparative study of ethanol oxidation with ozone on supported molybdenum and manganese oxide catalysts. Sci. Technol. Catal., 1999, 121, 105-110.

[35] Reed, C., Xi, Y., Oyama, S.T. Distinguishing between reaction intermediates and spectators: A kinetic study of acetone oxidation using ozone on a silica-supported manganese oxide catalyst. J. Catal., 2005, 235, 378-392.

[36] Xi, Y., Reed, C., Lee, Y.-K., Oyama, S.T. Acetone oxidation using ozone on manganese oxide catalysts. J. Phys. Chem. B, 2005, 109, 17587-17596.

[37] Reed, C., Lee, Y.K., Oyama, S.T. Structure and oxidation state of silica-supported manganese oxide catlysts and reactivity for acetone oxidation with ozone. J. Phys. Chem. B, 2006, 110, 4207-4216.

[38] Trawczynski, J., Bielak, B., Mista, W. Oxidation of ethanol over supported manganese catalysts-effect of the carrier. Appl. Catal. B, 2005, 55, 277-285.

[39] Oda, T., Takahashi, T., Yamaji, K. TCE decomposition by the nonthermal plasma process concerning ozone effect. IEEE Trans. Ind. Appl., 2004, 40, 1249-1256.

[40] Oda, T., Han, S., Ono, R. Dilute trichloroethylene decomposition in air by the non-thermal plasma process combined with the manganese oxide. J. Adv. Oxid. Technol., 2005, 8, 18-24.

[41] Tong, S.P., Liu, W.P., Leng, W.H., Zhang, Q.Q. Characteristics of MnO_2 catalytic ozonation of sulfosalicylic acid and propionic acid in water. Chemosphere, 2003, 50, 1359-1364.

[42] Villaseñor, J., Reyes, P., Pecchi, G. Catalytic and photocatalytic ozonation of phenol on MnO_2 supported catalysts. Catal. Today, 2002, 76, 121-131.

[43] Gervasini, A., Pirola, C., Ragaini, V. Destruction of carbon tetrachloride in the presence of hydrogen-supplying compounds with ionisation and catalytic oxidation. Appl. Catal. B, 2002, 38, 17-28.

[44] Gervasini, A., Pirola, C., Zilio, S., Ragaini, V. Destruction of carbon tetrachloride in the presence of hydrogen-supplying compounds with ionisation and catalytic oxidation – Part 2. Methane as hydrogen font. Appl. Catal. B, 2004, 47, 257-267.

[45] Fujimoto, T., Mizukoshi, Y., Nagata, Y., Maeda, Y., Oshima, R. Sonolytical preparation of various types of metal nanoparticles in aqueous solution. Scripta Mater. 2001, 44, 2183-2186.

[46] Lume-Pereira, C., Baral, S., Henglein, A., Janata, E. Chemistry of colloidal manganese dioxide. 1. Mechanism of reduction by an organic radical (a radiation chemical study). J. Phys. Chem. 1985, 89, 5772-5778.

[47] Stadniychuk, H.P., Anderson, M.A., Chapman, T.W. Sol-gel-derived thin-film manganese dioxide cathodes. J. Electrochem. Soc. 1996, 143, 1629-1632.

[48] Ulrich, H.J., Stone, A.T. Oxidation of chlorophenols absorbed to manganese oxide surfaces. Environ. Sci. Technol. 1989, 23, 421-428.

[49] Luo, Y. Preparation of MnO_2 nanoparticles by directly mixing potassium permanganate and polyelectrolyte aqueous solutions. Materials Letters, 2007, 61, 1893-1895.

[50] Kijima, N., Yasuda, H., Sato, T., Yoshimura, Y. Preparation and characterization of open tunnel oxide α-MnO_2 precipitated by ozone oxidation. J. Solid State Chem., 2001, 159, 94-102.

[51] Shanbhag, P.V., Guha, A.K., Sirkar, K.K. Membrane-based ozonation of organic compounds. Ind. Eng. Chem. Res. 1998, 37, 4388-4398.

[52] Shen, Z.S., Semmens, M.J., Collins, A.G. A novel-approach to ozone water mass-transfer using hollow fiber reactors. Environ. Technol. 1990, 11, 597-608.

[53] Oh, B.S., Jang, H.Y., Jung, Y.J., Kang, J.W. Microfiltration of MS2 bacteriophage: Effect of ozone on membrane fouling. J. Membr. Sci. 2007, 306, 244-252.

[54] You, S.H., Tseng, D.H., Hsu, W.C. Effect and mechanism of ultrafiltration membrane fouling removal by ozonation. Desalination, 2007, 202, 224-230.

[55] Castro, K., Zander, A.K. Membrane air-stripping-effects of pretreatment. J. Am. Water Works Assoc., 1995, 87, 50-61.

[56] Pines, D.S., Min, K.N., Ergas, S.J., Reckhow, D.A. Investigation of an ozone membrane contactor system. Ozone Sci. Eng., 2005, 27, 209-217.

[57] Lee, S., Lee, K., Wan, W.M., Choi, Y. Comparison of membrane permeability and a fouling mechanism by pre-ozonation followed by membrane filtration and residual ozone in membrane cells. Desalination, 2005, 178, 287-294.

[58] Mori, Y., Oota, T., Hashino, M., Takamura, M., Fujii, Y. Ozone-microfiltration system. Desalination, 1998, 117, 211-218.

[59] Hashino, M., Mori, Y., Fujii, Y., Motoyama, N., Kadakawa, N., Howshikawa, N., Nishijima, W., Okada, M. Pilot plant evaluation of an ozone-microfiltration system for drinking water treatment. Water Sci. Technol., 2000, 41, 17-23.

[60] Park, Y.G. Effect of ozonation for reducing membrane-fouling in the UF membrane. Desalination, 2002, 147, 43-48.

[61] Kim, J., Shan, W., Davies, S.H.R., Baumann, M.J., Masten, S.J., Tarabara, V.V. Interactions of aqueous NOM with nanoscale TiO_2: Implications for ceramic membrane filtration-ozonation hybrid process. Environ. Sci. Technol., 2009, 43, 5488-5494.

[62] Lehman, S.G., Liu, L. Application of ceramic membranes with pre-ozonation for treatment of secondary wastewater effluent. Wat. Res., 2009, 43, 2020-2028.

[63] Kim, J., Davies, S.H.R., Baumann, M.J., Tarabara, V.V., Masten, S.J. Effect of ozone dosage and hydrodynamic conditions on the permeate flux in a hybrid ozonation-ceramic ultrafiltration system treating natural waters. J. Membr. Sci., 2008, 311, 165-172.

[64] Cremades, L.V., Rodriguez-Grau, E., Mulero, R., Cusidó, J.A. Comparative Study of the performance of three cross-flow ceramic membranes for water treatment. Water SA, 2007, 33, 253-259.

[65] Karnik, B.S., Davies, S.H.R., Chen, K.C., Jaglowski, D.R., Baumann, M.J., Masten, S.J. Effects of ozonation on the permeate flux of nanocrystalline ceramic membranes. Water Research, 2005, 39, 728-734.

[66] Karnik, B.S., Davies, S.H., Baumann, M.J., Masten, S.J. Use of salicylic acid as a model compound to investigate hydroxyl radical reaction in an ozonation–membrane filtration hybrid process. Environ. Eng. Sci., 2007, 24, 852-860.

[67] Karnik, B.S., Davies, S.H., Baumann, M.J., Masten, S.J. Removal of Escherichia coli after treatment using ozonation-ultrafiltration with iron oxide-coated membranes. Ozone Sci. Eng., 2007, 29, 75-84.

[68] Karnik, B.S., Baumann, M.J., Corneal, L.M., Masten, S.J., Davies, S.H., TEM characterization of iron-oxide-coated ceramic membranes. J. Mater. Sci., 2009, 44, 4148-4154.

[69] Sun, Z.Z., Ma, J., Wang, L.B., Zhao, L. Degradation of nitrobenzene in aqueous solution by ozone-ceramic honeycomb. J. Environ. Sci., 2005, 17, 716-721.

[70] Lee, S., Cho, J. Comparison of ceramic and polymeric membranes for natural organic matter (NOM) removal. Desalination, 2004, 160, 223-232.

[71] Schlichter, B., Mavrov, V., Chmiel, H. Study of a hybrid process combining ozonation and membrane filtration – filtration of model solutions. Desalination, 2003, 156, 257-265.

[72] Burggraaf, A.J., Cot, L. Fundamentals of inorganic membrane science and technology, Elsevier Science B.V., Amsterdam, Netherlands, 1996.

[73] Bhave, R.R. Inorganic Membranes, Synthesis, Characteristics, and Applications, Van Nostrand Reinhold, New York, 1991.

[74] Alem, A., Sarpoolaky, H., Keshmiri, M. Titania ultrafiltration membrane: Preparation, characterization and photocatalytic activity. J. Eur. Ceram. Soc., 2009, 29, 629-635.

[75] Chen, A.S.C., Stencel, N., Ferguson, D. Using ceramic membranes to recycle two nonionic alkaline metal-cleaning solutions. J. Membr. Sci., 1999, 162, 219-234.

[76] Lehman, S.G., Liu, L. Application of ceramic membranes with pre-ozonation for treatment of secondary wastewater effluent. Wat. Res., 2009, 43, 2020-2028.

[77] Baruah, G.L., Nayak, A., Belfort, G. Scale-up from laboratory microfiltration to a ceramic pilot plant: Design and performance. J. Membr. Sci., 2006, 274, 56-63.

[78] Owen, G., Bandi, M., Howell, J.A., Churchouse, S.J. Economic assessment of membrane processes for water and waste water treatment. J. Membr. Sci., 1995, 102, 77-91.

[79] Wang, P., Xu, N., Shi, J. A pilot study of the treatment of waste rolling emulsion using zirconia microfiltration membranes. J. Membr. Sci., 2000, 173, 159-166.

[80] Bottino, A., Capannelli, C., Del Borghi, A., Colombino, M., Conio, O. Water treatment for drinking purpose : ceramic microfiltration application. Desalination, 2001, 141, 75-79.

[81] Chen, L., Horiuchi, T., Mori, T. Catalytic reduction of NO over a mechanical mixture of $NiGa_2O_4$ spinel with manganese oxide: influence of catalyst preparation method. App. Catal. A, 2001, 209, 97-105.

[82] Radwan, N.R.E., El-Shobaky, G.A., Fahmy, Y.M. Cordierite as catalyst support for cobalt and manganese oxides in oxidation-reduction reactions. App. Catal. A, 2004, 274, 87-99.

[83] Ramesh, K., Chen, L., Chen, F., Zhong, Z., Chin, J., Mook, H., Han, Y-F. Preparation and characterization of coral-like nanostructured α-Mn_2O_3 catalyst for catalytic combustion of methane. Catal. Commun. 2007, 8, 1421-1426.

[84] Dampier, F.W. The cathodic behavior of CuX, MoO_3 and MnO_2 in lithium cells. J. Electrochem. Soc. 1974, 121, 656-660.

[85] Pistoia, G. Some restatements on the nature and behavior of MnO_2 in Li batteries. J. Electrochem. Soc. 1982, 129, 1861-1865.

[86] Nardi, J.C. Characterization of the Li/MnO_2 multistep discharge. J. Electrochem. Soc. 1985, 132, 1787-1791.

[87] Bach, S., Henry, M., Baffier, N., Livage, J. Sol-gel synthesis of manganese oxides. J. Solid State Chem. 1990, 88, 325-333.

[88] Langlais, B., Reckhow, D.A., Brink, D.R. Ozone in water treatment application and engineering, Lewis Publishing, Chelsea, MI, 1991, pp. 139.

[89] Kissinger, H.E., McMurdie, H.F., Simpson, B.S. Thermal decomposition of manganous and ferrous carbonates. J. Am. Ceram. Soc. 1956, 39, 168-172.

[90] Klingsberg, C., Roy, R. Solid-solid and solid-vapor reactions and a new phase in the system Mn-O. J. Am. Ceram. Soc. 1960, 43, 620-626.

[91] Lvov, Y., Munge, B., Giraldo, O., Ichinose, I., Suib, S.L., Rusling, J.F. Films of manganese oxide nanoparticles with polycations or myoglobin from alternate-layer adsorption. Langmuir 2000, 16, 8850-8857.

[92] Decher, G. Fuzzy nanoassemblies: Toward layered polymeric multicomposites. Science 1997, 227, 1232-1237.

[93] Lvov, Y, Decher, G., Mohwald, H. Assembly, structural characterization, and thermal behavior of layer-by-layer deposited ultrathin films of poly(vinyl sulfate) and poly(allylamine). Langmuir 1993, 9, 481-486.

[94] Espinal, L., Suib, S.L., Rusling, J.F. Electrochemical catalysis of styrene epoxidation with films of MnO_2 nanoparticles and H_2O_2. J. Am. Chem. Soc. 2004, 126, 7676-7682.

[95] Lin, Y.S., Chang, C.H., Gopalan, R. Improvement of thermal stability of porous nanostructured ceramic membranes. Ind. Eng. Res., 1994, 33, 860-870.

[96] Bredesen, R., Jordal, K., Bolland, O. High-temperature membranes in power generation with CO_2 capture. Chem. Eng. Proc., 2004, 43, 1129-1158.

[97] Barsoum, M.W. Fundamentals of Ceramics, Cantor, B., Goringe, M.J. (Eds.) Institute of Physics Publishing, Bristol, UK, 2003.

[98] Kingery, W.D., Bowen, H.K., Uhlmann, D.R. Introduction to Ceramics, Second Edition. John Wiley & Sons, New York, NY, 1976.

[99] Baticle, P., Kiefer, C., Lakhchaf, N., Larbot, A., Leclerc, O., Persin, M., Sarrazin, J. Salt filtration on gamma alumina nanofiltration membranes fired at two different temperatures. J. Membr. Sci., 1997, 135, 1-8.

[100] Leenaars, A.F.M., Burggraaf, A.J. The preparation and characterization of alumina membranes with ultra fine pores. Part 2. The formation of supported membranes. J. Colloid Interface Sci., 1985, 105, 27-40.

[101] Klein, L.C., Gallagher, D. Pore structures of sol-gel silica membranes. J. Membr. Sci., 1988, 39, 213-220.

[102] Shojai, F., Mäntylä, T. Monoclinic zirconia microfiltration membranes: Preparation and characterization. J. Porous Mater., 2001, 8, 129-142.

[103] Khemankhem, S., Larbot, A., Ben Amar, R. New Ceramic microfiltration membranes from Tunisian natural materials: Application for the cuttlefish effluents treatment. Ceram. Int., 2009, 35, 55-61.

[104] Gulicovski, J.J., Čerović, L.S., Milonjić, S.K. Point of zero charge and isoelectric point of alumina. Mater. Manuf. Process., 2008, 23, 615-619.

[105] Bitea, C., Walther, C., Kim, J.I., Geckeis, H., Rabung, T., Scherbaum, F.J., Cacuci, D.G. Time-resolved observation of ZrO_2-colloid agglomeration. Coll. Surf. A., 2003, 215, 55-66.

[106] Tonkin, J.W., Balistrieri, L.S., Murray, J.W. Modeling sorption of divalent metal cations on hydrous manganese oxide using the diffuse double layer model. Appl. Geochem., 2004, 19, 29-53.

[107] McKenzie, R.M. The surface charge on manganese dioxides. Aust. J. Soil Res., 1981, 19, 41-50.

[108] Rao, C.N.R., Müller, A., Cheetham, A.K. The chemistry of nanomaterials: synthesis, properties and applications, Wiley, Chichester, UK, 2004, p. 1.

[109] Gleiter, H. Nanocrystalline materials. Prog. Mater. Sci., 1989, 33, 223-315.

[110] Morgan, J.J., Stumm, W. Analytical chemistry of aqueous manganese. Journ. AWWA. 1965, 107-119.

[111] Cheney, M.A., Bhowmik, P.K., Moriuchi, S., Birkner, N.R., Hodge, V.F., Elkouz, S.E. Synthesis and characterization of two phases of manganese oxide from decomposition of permanganate in concentrated sulfuric acid at ambient temperature. Coll. Surf. A, 2007, 307, 62-70.

[112] Reddy, R.N., Reddy, R.G. Sol-gel MnO_2 as an electrode material for electrochemical capacitors. J. Power Sources, 2003, 124, 330-337.

[113] Jucker, C., Clark, M.M. Adsorption of aquatic humic substances on hydrophobic ultrafiltration membranes. J. Membr. Sci. 1994, 97, 37-52.

[114] Cho, J., Amy, G., Pellegrino, J., Yoon, Y. Characterization of clean and natural organic matter (NOM) fouled NF and UF membranes, and foulants characterization. Desalination, 1998, 118, 101-108.

[115] Yuan, W., Zydney, A.L. Humic acid fouling during ultrafiltration. Environ. Sci. Technol. 2000, 34, 5043-5050.

[116] Violleau, D., Essis-Tome, H., Habarou, H., Croué, J.P., Pontié, M. Fouling studies of a polyamide nanofiltration membrane by selected natural organic matter : an analytical approach. Desalination, 2005, 173, 223-238.

[117] Schäfer, A.I., Fane, A.G., Waite, T.D. Nanofiltration of natural organic matter: Removal, fouling and the influence of multivalent ions. Desalination, 1998, 118, 109-122.

[118] Schäfer, A.I., Fane, A.G., Waite, T.D. Fouling effects on rejection in the membrane filtration of natural waters. Desalination, 2000, 131, 215-224.

[119] Crozes, G.F., Jacangelo, J.G., Anselme, C., Laîné, J.M. Impact of ultrafiltration operating conditions on membrane irreversible fouling. J. Membr. Sci., 1997, 124, 63-76.

[120] Ventresque, C., Gisclon, V., Bablon, G., Chagneau, G. An outstanding feat of modern technology: the Mery-sur-Oise Nanofiltration Treatment Plant (340,000 m(3)/d). Desalination, 2000, 131, 1-16.

[121] Childress, A.E., Deshmukh, S.S. Effect of humic substances and anionic surfactants on the surface charge and performance of reverse osmosis membranes. Desalination, 1998, 118, 167-174.

[122] Jarusutthiriak, C., Amy, G., Croué, J.-P. Fouling characteristics of wastewater effluent organic matter (EfOM) isolates on NF and UF membranes. Desalination, 2002, 145, 247-255.

[123] Her, N., Amy, G., Jarusutthirak, C. Seasonal variations of nanofiltration (NF) foulants: identification and control. Desalination, 2000, 132, 143-160.

[124] Bowen, W.R., Doneva, T.A., Yin, H.-B. Separation of humic acid from a model surface water with PSU/SPEEK blend UF/NF membranes. J. Membr. Sci., 2002, 206, 417-429.

[125] Nilson, J.A., DiGiano, F.A. Influence of NOM composition on nanofiltration. J. AWWA, 1996, 5, 53-66.

[126] Seidel, A., Elimelech, M. Coupling between chemical and physical interactions in natural organic matter (NOM) fouling of nanofiltration membranes: implications for fouling control. J. Membr. Sci., 2002, 203, 245-255.

[127] Hong, S., Elimelech, M. Chemical and physical aspects of natural organic matter (NOM) fouling of nanofiltration membranes. J. Membr. Sci., 1997, 132, 159-181.

[128] Gwon, E.-M., Yu, M.-J., Oh, H.-K., Ylee, Y.-H. Fouling characteristics of NF and RO operated for removal of dissolved matter from groundwater. Wat. Res., 2003, 37, 2989-2997.

[129] Vrouwenvelder, J.S., Kappelhof, J.W.N.M., Heijman, S.G.J., Schippers, J.C., Van Der Kooija, D. Tools for fouling diagnosis of NF and RO membranes and assessment of the fouling potential of feed water. Desalination, 2003, 157, 361-365.

[130] Košutić, K., Kunst, B. RO and NF membrane fouling and cleaning and pore size distribution variations. Desalination, 2002, 150, 113-120.

[131] Combe, A., Molis, E., Lucas, P., Riley, R., Clark, M.M. The effect of CA membrane properties on adsorptive fouling by humic acid. J. Membr. Sci., 1999, 154, 73-87.

[132] Cho, J., Amy, G., Pellegrino, J. Membrane filtration of natural organic matter: initial comparison of rejection and flux decline characteristics with ultrafiltration and nanofiltration membranes. Wat. Res., 1999, 33, 2517-2526.

[133] Manttari, M., Puro, L., Nuortila-Jokinen, J., Nyström, M. Fouling effects of polysaccharides and humic acid in nanofiltration. J. Membr. Sci., 2000, 165, 1-17.

[134] Champlin, T.L. Using circulation tests to model natural organic matter adsorption and particle deposition by spiral-wound nanofiltration membrane elements. Desalination, 2000, 131, 105-115.

[135] Fan, L., Harris, J.L., Roddick, F.A., Booker, N.A. Influence of the characteristics of natural organic matter on the fouling of microfiltration membranes. Wat. Res., 2001, 35, 4455-4463.

[136] Meier-Haack, J., Booker, N.A., Carroll, T. A permeability-controlled microfiltration membrane for reduced fouling in drinking water treatment. Wat. Res., 2003, 37, 585-588.

[137] Carroll, T., Booker, N.A., Meier, Haack, J. Polyelectrolyte-grafted microfiltration membranes to control fouling by natural organic matter in drinking water. J. Membr. Sci., 2002, 203, 3-13.

[138] Roudman, A.R., DiGiano, F.A. Surface energy of experimental and commercial nanofiltraiton membranes: effects of wetting and natural organic matter fouling. J. Membr. Sci., 2000, 175, 61-73.

[139] Von Gunten, U. Ozonation of drinking water. Part I. Oxidation kinetics and product formation. Water Res. 2003, 37, 1443-1467.

[140] Westerhoff, P., Aiken, G., Amy, G., Debroux, J. Relationships between the structure of natural organic matter and its reactivity toward molecular ozone and hydroxyl radicals. Wat. Res., 1999, 33, 2265-2276.

[141] Zhu, H.T., Wen, X.H., Huang, X. Pre-ozonation for dead-end microfiltration of the secondary effluent: suspended particles and membrane fouling. Desalination, 2008, 231, 166-174.

[142] Lee, S., Jang, N., Watanabe, Y. Effect of residual ozone on membrane fouling reduction in ozone resisting microfiltration (MF) membrane system. Water Sci. Technol., 2004, 50, 287-292.

[143] Lu, H., Hu, J., Chen, C., Sun, H., Hu, X., Yang, D. Characterization of Al_2O_3–Al nano-composite powder prepared by a wet chemical method. Ceram. Int. 2005, 31, 481-485.

[144] Cortalezzi, M., Rose, J., Wells, G., Bottero, J., Barron, A., Weisner, M. Ceramic membranes derived from ferroxane nanoparticles: a new route for the fabrication of iron oxide ultrafiltration membranes. J. Membr. Sci. 2003, 227, 207-217.

[145] Cortalezzi, M., Rose, J., Barron, A., Weisner, M. Characteristics of ultrafiltration ceramic membranes derived from alumoxane nanoparticles. J. Membr. Sci. 2002, 205, 33-43.

[146] Chou, K., Kao, K., Huang, C., Chen, C. Coating and Characterization of Titania Membrane on Porous Ceramic Supports. J. Porous Mater. 1999, 6, 217-225.

[147] Bae, D., Cheong, D., Han, K., Choi, S. Fabrication and Microstructure of Al_2O_3-TiO_2 Composite Membranes with Ultrafine Pores. Ceram. Int. 1998, 24, 25-30.

[148] Pedersen, H., Tranto, J., Høj, J. Characterization of multilayer ceramic membranes with the atomic force microscope. Key Eng. Mater. 1997, 132-136, 1707-1710.

[149] Seijger, G.B.F., Van den Berg, A., Riva, R., Krishna, K., Calis, H.P.A., Van Bekkum, H., Van den Bleek, C.M. In situ preparation of ferrierite coatings on cordierite honeycomb supports. Appl. Catal. A, 2002, 236, 187-203.

[150] Oldani, M., Schock, G. Characterization of ultrafiltration membranes by infrared spectroscopy, ESCA, and contact angle measurements. J. Membr. Sci., 1989, 43, 243-258.

[151] Fievet, P., Szymczyk, A., Aoubiza, B., Pagetti, J. Evaluation of three methods for the characterisation of the membrane-solution interface: streaming potential, membrane potential and electrolyte conductivity inside pores. J. Membr. Sci., 2000, 168, 87-100.

[152] Zhang, Q., Jing, W.H., Fan, Y.Q., Xu, N.P. An improved Parks equation for prediction of surface charge properties of composite ceramic membranes. J. Membr. Sci., 2008, 318, 100-106.

[153] Zhang, Q., Fan, Y.Q., Xu, N.P. Effect of the surface properties on filtration performance of Al_2O_3-TiO_2 composite membrane. Sep. Purif. Technol., 2009, 66, 306-312.

[154] McCafferty, E., Wightman, J.P. Determination of the surface isoelectric point of oxide films on metals by contact angle titration. J. Coll. Interf. Sci., 1997, 194, 344-355.

[155] Szymczyk, A., Fievet, P., Reggiani, J.C., Pagetti, J. Characterisation of surface properties of ceramic ultrafiltration membranes by studying diffusion-driven transport and streaming potential. Desalination, 1998, 119, 303-308.

[156] Wyart, Y., Georges, G., Deumié, C., Amra, C., Moulin, P. Membrane characterization by microscopic methods: Multiscale structure. J. Membrane Sci., 2008, 315, 82-92.

[157] Nandi, B.K., Uppaluri, R., Purkait, M.K. Preparation and characterization of low cost ceramic membranes for micro-filtration applications. Appl. Clay Sci., 2008, 42, 102-110.

[158] Benito, J.M., Conesa, A., Rubio, F., Rodríguez, M.A. Preparation and characterization of tubular ceramic membranes for treatment of oil emulsions. J. Eur. Ceram. Soc., 2005, 25, 1895-1903.

[159] Product Overview Characteristics for Inside CéRAM membranes (2009) Tami Industries website. http://www.tami-industries.com/products/lab_products.asp. Accessed 09 July 2009.

[160] Reilly, R.S., Smyth, C.A., Rakovich, Y.P., McCabe, E.M. The photoluminescent lifetime of polyelectrolytes in thin films formed via layer by layer self-assembly. Nanotechnology, 2009, 20.

[161] Tarabara, V.V., Wiesner, M.R. Effect of collision efficiency on the evolution of the surface of diffusion-limited deposits. J. Colloid Interface Sci. 2001, 237, 150-151.

[162] Cai, H., Shen, H., Yin, Y., Lu, L., Shen, J., Tang, Z. The effects of porous silicon on the crystalline properties of ZnO thin films. J. Phys. Chem. Solids. 2009, 70, 967-971.

[163] Shaoqiang, C., Ziqiang, Z., Jianzhong, Z., Jian, Z., Yanling, S., Ke, Y., Weiming, W., Xiaohua, W., Xiao, F., Laiqiang, L., Li, S. Hydroxyapatite coating on porous silicon substrate obtained by precipitation process. Appl. Surf. Sci. 2004, 230, 418-424.

[164] Ghosh, S., Kim, H., Hong, K., Lee, C. Microstructure of indium tin oxide films deposited on porous silicon by rf-sputtering. Mater. Sci. Eng. 2002, B95, 171-179.

[165] Shiau, F.-S., Fang, T.-T., Leu, T.-H. Effects of milling and particle size distribution on the sintering behavior and the evolution of the microstructure in sintering powder compacts. Mat. Chem. Phys., 1998, 57, 33-40.

[166] Binner, J., Vaidhyanathan, B. Processing of bulk nanostructured ceramics. J. Euro. Ceram. Soc., 2008, 28, 1329-1339.

[167] Shackelford, J.F. Introduction to Materials Science for Engineers, Second Edition, MacMillan, New York, NY, 1988.

[168] Liu, Y., Oh, K., Bai, J.G., Chang, C.-L., Yeo, W., Chung, J.-H., Lee, K.-H., Liu, W.K. Manipulation of nanoparticles and biomolecules by electric field and surface tension. Comput. Methods Appl. Mech. Engrg., 2008, 197, 2156-2172.

[169] Standard methods for Examination of Water and Wastewater, 20th ed.; Clesceri, L.S., Greenberg, A.E., Eaton, A.D., Eds.; American Public Health Association: Washington, DC, 1998.

[170] Chen, C., Zhang, X., He, W., Han, H. Comparison of seven kinds of drinking water treatment processes to enhance organic material removal: A pilot test. Sci. Total Environ. 2007, 382, 93-102.

[171] Kalscheur, K.N., Gerwe, C.E., Kweon, J., Speitel, G.E., Lawler, D.F. Enhanced softening: Effects of source water quality on NOM removal and DBP formation. J. AWWA 2006, 98, 93-106.

[172] Barrett, S.E., Krasner, S.W., Amy, G.L. Natural Organic Matter and Disinfection By-Products. American Chemical Society, Washington, D.C., 2000, p.48.

[173] Byun, S., Department of Civil and Environmental Engineering, Michigan State University, Post Doctoral Researcher. Personal communication, 2009.

[174] Huang, X., Leal, M., Li, Q. Degradation of natural organic matter by TiO_2 photocatalytic oxidation and its effect on fouling of low-pressure membranes. Water Res. 2008, 42, 1142-1150.

[175] Lei, L.C., Hu, X.J., Yue, P.-L. Improved wet oxidation for the treatment of dyeing wastewater concentrate from membrane separation process. Water Res. 1998, 32, 2753-2759.

[176] Li, D., Hwang, S.T. Gas separation by silicon based inorganic membrane at high-temperature. J. Membr. Sci., 1992, 66, 119-127.

[177] Zaman, J., Chakma, A. Inorganic membrane reactors. J. Membr. Sci., 1994, 92, 1-28.

[178] Koukou, M.K., Papayannakos, N., Markatos, N.C., Bracht, M., Van Veen, H.M., Roskam, A. Performance of ceramic membranes at elevated pressure and temperature: effect of non-ideal flow conditions in a pilot scale membrane separator. J. Membr. Sci., 1999, 155, 241-259.

[179] Ahmad, A.L., Othman, M.R., Idrus, N.F. Synthesis and characterization of nano-composite alumina-titania ceramic membrane for gas separation. J. Am. Ceram. Soc., 2006, 89, 3187-3193.

[180] Xomeritakis, G., Tsai, C.Y., Jiang, Y.B., Brinker, C.J. Tubular ceramic-supported sol-gel silica-based membranes for flue gas carbon dioxide capture and sequestration. J. Membr. Sci., 2009, 341, 30-36.

[181] Ahmad, A.L., Othman, M.R., Mukhtar, H. H_2 separation from binary gas mixture using coated alumina-titania membrane by sol-gel technique at high-temperature region. Int. J. Hydrogen Energy, 2004, 29, 817-828.

[182] Bhatia, S., Thien, C.Y., Mohamed, A.R. Oxidative coupling of methane (OCM) in a catalytic membrane reactor and comparison of its performance with other catalytic reactors. Chem. Eng. J., 2009, 148, 525-532.

[183] Zhao, H., Li, A., Gu, J., Xiong, G. A novel preparation method for porous noble metal/ceramic catalytic membranes. J. Mater. Sci., 1999, 34, 2987-2996.

[184] Wang, Y.H., Liu, X.Q., Meng, G.Y. Preparation and properties of supported 100% titania ceramic membranes. Mater. Res. Bull., 2008, 43, 1480-1491.

[185] Kim, J., Lee, J.W., Lee, T.G., Nam, S.W., Han, J. Nanostructured titania membranes with improved thermal stability. J. Mater. Sci., 2005, 1797-1799.

[186] Sekulić, J., Magraso, A., Ten Elshof, J.E., Blank, D.H.A. Influence of ZrO_2 addition on microstructure and liquid permeability of mesoporous TiO_2 membranes. Micropor. Mesopor. Mater., 2004, 72, 49-57.

[187] Bae, D.-S., Han, K.-S., Choi, S.-H. Preparation and thermal stability of doped TiO_2 composite membranes by the sol-gel process. Solid State Ionics, 1998, 109, 239-245.

[188] Malaisamy, R., Mahendran, R., Mohan, D. Cellulose acetate and sulfonated polysulfone blend ultrafiltration membranes. II. Pore statistics, molecular weight cutoff, and morphological studies. J. Appl. Polym. Sci., 2002, 84, 430-444.

[189] Nagendran, A., Mohan, D. Protein separation by cellulose acetate/sulfonated poly(ether imide) blend ultrafiltration membranes. J. Appl. Polym. Sci., 2008, 110, 2047-2057.

[190] Koebrugge, G.W., Winnubst, L., Burggraaf, A.J. Thermal stability of nanostructured titania and titania-ceria ceramic powders prepared by sol-gel process. J. Mater. Chem., 1993, 3, 1095-1100.

[191] Kumar, K.N.P., Keizer, K., Burggraaf, A.J., Okubo, T., Nagamoto, H. Synthesis and textural properties of unsupported and supported rutile (TiO_2) membranes. J. Mater. Chem., 1993, 3, 923-929.

[192] Wegmann, M., Michen, B., Luxbacher, T., Fritsch, J., Graule, T. Modification of ceramic microfilters with colloidal zirconia to promote the adsorption of viruses from water. Water Res., 2008, 42, 1726-1734.

[193] Levin, E.M., Robbins, C.R., McMurdie, H.F. Phase Diagrams for Ceramists, Second Edition. Reser, M.K. (Ed.), The American Ceramic Society, Columbus, OH, 1964, fig. 773.

[194] McHale, A.E., Roth, R.S. Phase Equilibria Diagrams, Vol. XII, The American Ceramic Society, Columbus, OH, 1996, fig. 9805.

[195] McHale, A.E. Phase diagrams and ceramic processes, Chapman & Hall, New York, NY, 1998.

[196] Dias, A., Moreira, R.L., Mohallem, N.D.S., Vilela, J.M.C., Andrade, M.S. Nanometric powders and sintered ceramics studied by atomic force microscopy. J. Mater. Res. 1998, 13, 223-227.

[197] Martynczuk, J., Arnold, M., Feldhoff, A. Influence of grain size on the oxygen permeation performance of perovskite-type $(Ba_{0.5}Sr_{0.5})(Fe_{0.8}Zn_{0.2})O_{3-\delta}$ membranes. J. Membr. Sci., 2008, 322, 375-382.

[198] Shojai, F., Mäntylä, T.A. Effect of sintering temperature and holding time on the properties of 3Y-ZrO_2 microfiltration membranes. J. Mater. Sci., 2001, 36, 3437-3446.

[199] Cruz, H.S., Spino, J., Grathwohl, G. Nanocrystalline ZrO_2 ceramics with idealized macropores. J. Eur. Ceram. Soc., 2008, 28, 1783-1791.

[200] Gleiter, H. Nanocrystalline materials. Prog. Mater. Sci., 1989, 33, 223-315.

[201] Schaep, J., Vandecasteele, C., Peeters, B., Luyten, J., Dotremont, C., Roels, D. Characteristics and retention properties of a mesoporous γ-Al_2O_3 membrane for nanofiltration. J. Membr. Sci. 1999, 163, 229-237.

[202] Ma, N., Quan, X., Zhang, Y., Chen, S., Zhao, H. Integration of separation and photocatalysis using an inorganic membrane modified by Si-doped TiO_2 for water purification. J. Membr. Sci. 2009, 335, 58-67.

[203] Benito, J.M., Conesa, A., Rubio, F., Rodríguez, M.A. Preparation and characterization of tubular ceramic membranes for treatment of oil emulsions. J. Euro. Ceram. Soc. 2005, 25, 19=895-1903.

[204] Lee, S.-H., Chung, K.-C., Shin, M.-C., Dong, J.-I., Lee, H.-S., Auh, K.H. Preparation of ceramic membrane and application to the crossflow microfiltration of soluble waste oil. Mater. Lett. 2002, 52, 266-271.

[205] Majhi, A., Monash, P., Pugazhenthi, G. Fabrication and characterization of γ-Al_2O_3-clay composite ultrafiltration membrane for the separation of electrolytes from its aqueous solution. J. Membr. Sci. 2009, 340, 181-191.

[206] Julbe, A., Rouessac, V., Durang, J., Ayral, A. New approaches in the design of ceramic and hybrid membranes. J. Membr. Sci. 2008, 316, 176-185.